

CIRCULARLY POLARIZED DIELECTRIC
RESONATOR ANTENNA WITH PERIODIC
LOADING FOR GNSS APPLICATIONS

ANTENNE À POLARISATION CIRCULAIRE
COMPOSÉE D'UN RESONATEUR
DIÉLECTRIQUE CHARGÉE PAR UNE
STRUCTURE PÉRIODIQUE POUR
APPLICATIONS GNSS

A Thesis Submitted to the Division of Graduate Studies
of the Royal Military College of Canada
by

Slobodan Jović

In Partial Fulfillment of the Requirements for the Degree of
Master of Applied Science in Electrical and Computer Engineering

August, 2019

© This thesis may be used within the Department of National Defence
but copyright for open publication remains the property of the author.

To my dear children: Jelena, Nikola, Aleksandar, Nemanja and Djordje.

Acknowledgments

First and foremost, I would like to offer many thanks to my thesis advisor, *Dr. Yahia M. M. Antar* for his guidance, help and patience throughout this experience. And, I would like to offer many thanks also to my thesis co-advisor, *Dr. Michel Clénet* who coached me, shared his knowledge and provided valuable ideas, insights and assistance.

I wish to acknowledge the *Department of National Defence* (DND) and *Defence Research Development Canada* (DRDC), Ottawa research center, for encouraging and supporting me to further my education during my employment.

Abstract

Jović, S. M.A.Sc. Royal Military College of Canada, August, 2019. Circularly polarized dielectric resonator antenna with periodic loading for GNSS applications. Supervised by Dr. Yahia M.M. Antar and co-supervised by Dr. Michel Clénet.

A novel dual-sense circularly polarized (CP) dielectric resonator antenna (DRA) concept for the Global Navigation Satellite Systems (GNSS) is presented. The concept introduces a loaded annular dielectric resonator (DR) excited using 4-ports fed in a quadrature. The excitation is based on vertical conformal strips where strips are incorporated into the design and contribute to the overall antenna performance. The most unique feature of this antenna is the resonator load, which modifies the boundary conditions of the resonator core. The load consists of a one-dimensional array of periodic elements that behave like an electromagnetic band-gap structure (EBG). The impact on the antenna performance is multifold, including improved bandwidth, radiation efficiency and reduced mutual coupling between the excitation ports. The antenna also exhibits a radiation stop-band.

The experimental results show that this antenna effectively covers both the lower (1165-1300 MHz) and upper (1560-1610 MHz) GNSS bands. The 0 dBic gain and 3 dB axial ratio (AR) bandwidth significantly exceed the 10 dB return loss bandwidth. The 0 dBic gain and 3 dB AR beamwidth range from 105° to 120° and from 135° to 165° , respectively. The radiation stop-band is at 1355 MHz covering a 10 dB radiation suppression band of about 15 MHz.

The antenna is about 24.5 mm high and uses a 90 mm diameter ground plane. It improves upon the current state of the art by resolving its two main limitations; the height of the antenna (38% reduced) and lack of a real-estate for the antenna front-end electronics. At the same time, the antenna main-

tains radiation performances comparable to the state of the art. The main disadvantages of this antenna are the cost and fabrication complexity.

Keywords: *dielectric resonator antenna, wideband, circular polarization, Global Navigation Satellite Systems, engineered surfaces, electromagnetic periodic structures, electromagnetic band-gap structures*

Résumé

Jović, S. M.A.Sc. Collège militaire royal du Canada, août, 2019. Antenne à polarisation circulaire composée d'un résonateur diélectrique chargée par une structure périodique pour applications GNSS. Thèse dirigée par Professeur Dr. Yahia M.M. Antar plus co-dirigée par Dr. Michel Clénet.

Un nouveau concept d'antenne à résonateur diélectrique à polarisation circulaire (CP) à double sens pour les systèmes mondiaux de navigation par satellite (GNSS) est présenté. Le concept introduit un résonateur diélectrique annulaire (DR) chargé et excité à l'aide de 4 ports alimentés en quadrature. L'excitation est basée de lignes microrubans conformes verticales et est incorporée dans la conception et contribue à la performance globale de l'antenne. La caractéristique la plus unique de cette antenne est la charge du résonateur, qui modifie les conditions aux limites du résonateur. La charge consiste en un réseau unidimensionnel d'éléments périodiques se comportant comme une structure à bande interdite électromagnétique (EBG). L'impact sur les performances de l'antenne est multiple, notamment l'amélioration de la bande passante, de l'efficacité du rayonnement et de la réduction du couplage mutuel entre les ports d'excitation. L'antenne présente également une bande de rejection de rayonnement.

Les résultats expérimentaux montrent que cette antenne couvre efficacement les bandes GNSS inférieure (1165-1300 MHz) et supérieure (1560-1610 MHz). Le gain à 0 dBic et la largeur de bande du taux d'ellipticité (AR) de 3 dB dépassent de manière significative la largeur de bande d'adaptation de 10 dB. Le gain à 0 dBic et la largeur de faisceau à 3 dB AR vont de 105° à 120° et de 135° à 165° , respectivement. La bande de rejection du rayonnement est à 1355 MHz et couvre une bande de suppression de rayonnement de 10 dB d'environ 15 MHz.

L'antenne a une hauteur d'environ 24,5 mm et utilise un plan de masse de 90 mm de diamètre. Cette antenne améliore l'état de l'art en résolvant deux principales limitations: la hauteur de l'antenne (réduction de 38%) et l'absence de surface sous le plan de masse pour l'électronique radio-fréquence de l'antenne. Parallèlement, l'antenne maintient des performances de rayonnement comparables à celles de l'état de l'art. Les principaux inconvénients de cette antenne sont le coût et la complexité de la fabrication.

Keywords: *antenne à résonateur diélectrique, large bande, polarisation circulaire, systèmes mondiaux de navigation par satellite, structures périodiques électromagnétiques, structures à bande interdite électromagnétique*

Contents

Acknowledgments	iii
Abstract	iv
Résumé	vi
List of Acronyms	xviii
1 Introduction	1
1.1 Motivation	1
1.2 Problem definition	2
1.3 Scope	2
1.4 Methodology	2
1.5 Main contributions	3
1.6 Thesis organization	3
2 GNSS antenna properties and requirements	5
2.1 Conventions	5
2.2 GNSS concept	6
2.3 Impedance bandwidth	7
2.4 Radiation pattern and beamwidth	8
2.4.1 Elevation masking angle	8
2.5 Antenna radiation parameters	9
2.5.1 Directivity	9
2.5.2 Gain and radiation efficiency	10
2.5.3 Antenna gain performance parameters	11
2.5.4 Antenna gain performance requirements	12
2.6 Polarisation	13
2.6.1 Polarisation axial ratio	14
2.6.2 Polarisation efficiency and polarisation mismatch loss	15

2.6.3	Axial ratio and interference suppression	17
2.6.4	Axial ratio performance parameters and requirements	18
2.7	Antenna phase center and group delay	19
2.7.1	Phase center	19
2.7.2	Group delay	20
2.7.3	Radiation symmetry, phase center and group delay	21
2.8	Summary	22
3	Literature review	23
3.1	Dielectric resonator antenna	23
3.1.1	History	24
3.1.2	Advantages	24
3.1.3	Concept of operation	25
3.2	Dielectric resonator	25
3.2.1	Analysis techniques	25
3.2.2	Cylindrical DR	27
3.2.3	Cylindrical DR internal EM fields	28
3.2.4	Rectangular DR	31
3.2.5	Rectangular DR internal EM fields	31
3.2.6	DR and application of the image theory	34
3.3	Quality factor and coupling coefficient	35
3.3.1	Quality factor Q	35
3.3.2	BW and Q -factor	36
3.3.3	Coupling coefficient χ	36
3.4	Dielectric resonator excitation	37
3.4.1	Slot aperture	38
3.4.2	Coaxial probe	41
3.4.3	Microstrip line	42
3.4.4	Co-Planar waveguide	43
3.5	Circular polarisation	43
3.5.1	Multi-port excitation	45
3.5.2	Multi-port excitation and mutual coupling	46
3.6	Feeding network	47
3.7	Hybrid DRA	49
3.8	Finite size ground plane	50
3.9	State of the art	50
3.10	Summary	57
4	Cylindrical DRA design	59
4.1	Objectives	59

4.2	Dielectric resonator shape	60
4.3	Design of $HE_{11\delta}$ mode cylindrical dielectric resonator	61
4.3.1	Radiation mode	61
4.3.2	Quality factor Q and BW	62
4.3.3	Dielectric constant ϵ_r	62
4.3.4	Wave number $k_0 r$	64
4.3.5	DR dimensions	65
4.4	Circular polarization feeding network	67
4.5	Dielectric resonator excitation	67
4.5.1	Design of probe based coupling	69
4.5.2	Probe based coupling performance	70
4.6	Finite size ground plane	72
4.7	Simulated DR radiation performances	74
4.7.1	Resonant frequency and impedance BW	76
4.7.2	Radiation mode	78
4.7.3	Summary of findings	79
4.8	Conclusion	80
5	Annular DRA with periodic loading	81
5.1	Review of bandwidth enhancement techniques	81
5.1.1	Dielectric constant	81
5.1.2	Impedance matching	82
5.1.3	DR loading and hybrid DRA	82
5.1.4	Use of multiple resonators	83
5.1.5	DR and engineered surfaces	83
5.2	Annular DR	83
5.2.1	Design of annular DR for $HE_{11\delta}$ mode	84
5.2.2	Loaded annular DR	87
5.3	Periodic structure loaded annular DR	89
5.3.1	Periodic structure design	90
5.3.2	Loading structure and EBG	92
5.3.3	DR radiation modes	93
5.3.4	Loading structure resonance	94
5.3.5	Loading structure response control	94
5.4	Antenna simulated response with the loading structure	95
5.4.1	Realised gain, radiation pattern and AR	97
5.4.2	Feeding ports mutual coupling	99
5.5	Antenna final design	100
5.5.1	Impedance matching	102
5.6	Parametric analysis	103

5.7	Antenna fabrication	107
5.7.1	Dielectric resonator	107
5.7.2	Ground plane PCB	108
5.7.3	Loading structure	108
5.7.4	Antenna assembling	109
6	Experimental results	111
6.1	Antenna installation and alignment	111
6.1.1	Antenna installation	111
6.1.2	Antenna alignment	113
6.2	Antenna feeding circuit measurements	113
6.3	Measurement results	115
6.3.1	Resonant frequency and impedance bandwidth	115
6.3.2	Excitation ports mutual coupling	117
6.3.3	Realised gain	117
6.3.4	Radiation pattern and beamwidth	119
6.3.5	Polarisation and AR	120
6.4	Analysis	121
6.4.1	This work and state-of-the-art	123
6.4.2	This work and thesis objectives	123
7	Conclusions and recommendations	125
7.1	Recommendations and future work	126
	Bibliography	127
	Appendices	134
A	GNSS background	135
A.1	Fundamentals of GNSS	135
A.2	Status of GNSS	136
A.3	GNSS signals, modulation and spectral deconfliction	137
A.3.1	GPS Signals	138
A.3.2	GLONASS Signals	138
A.3.3	Galileo Signals	139
A.3.4	BeiDou Signals	139
A.4	GNSS Receiver	140
A.5	Single vs. dual frequency and single vs. multiple GNSS	141
B	Review of single-port CP excitation for DRA	143
B.1	Single mode	143

B.2	Dual mode	145
C	Cylindrical DRA design optimization	147
C.1	Cylindrical DR optimization	147
C.2	Cylindrical DRA optimization	148
C.2.1	Antenna design	149
C.2.2	Design optimization	149
C.2.3	Simulation results	150
C.3	Conclusion	153

List of Tables

2.1	Realised gain requirements for airborne E1 and L1 band antennas	13
2.2	GNSS antenna directive gain requirements	13
2.3	NovAtel 704X antenna AR at GPS frequencies	19
3.1	Cylindrical DR P values for lower order modes	36
3.2	State of the art multi-port excited CP DRA performance summary	57
3.3	State of the art multi-port excited CP DRA key design parameters	57
4.1	$HE_{11\delta}$ mode minimum Q_{rad} at 1385 MHz for $r = 45$ mm.	65
4.2	$HE_{11\delta}$ mode DR dimensions for $\epsilon_r = 10$ at 1385 MHz.	67
4.3	$HE_{11\delta}$ mode DR dimensions for $\epsilon_r = 12$ at 1385 MHz.	67
4.4	Performance summary of 1 and 4-port $HE_{11\delta}$ mode DR	72
4.5	η_{ant} of 1 and 4-port $HE_{11\delta}$ mode excited DR	72
4.6	$HE_{11\delta}$ mode simulated resonant frequency	77
4.7	$HE_{11\delta}$ mode simulated BW and Q-factor	77
5.1	Annular and cylindrical DR and antenna dimensions	87
5.2	Loading structure parameters, dimensions and descriptions.	92
5.3	Feeding port mutual coupling	101
5.4	Impedance matching network parameters.	104
6.1	Measured and simulated $G_r > 0$ $dBic$ beamwidth and HPBW . . .	120
6.2	Measured and simulated AR beamwidth	121
6.3	Summary of the results and state-of-the-art	123
6.4	Summary of the results and thesis objectives	124
A.1	GPS signals.	138
A.2	GLONASS signals.	139
A.3	Galileo signals.	139
A.4	BeiDou signals.	140

List of Figures

2.1	Field vectors and angle conventions in the spherical coordinates.	6
2.2	Basis of the GNSS navigation concept	7
2.3	GNSS antenna ideal and typical radiation pattern.	9
2.4	Antenna directivity vs. the low elevation masking angle.	10
2.5	Far-field polarisation ellipse.	15
2.6	Antenna polarisation losses vs. AR	16
2.7	Receive antenna multipath signal suppression vs. AR	18
2.8	Equiphase contour and antenna phase center	20
3.1	Basic dielectric resonator shapes	26
3.2	Cylindrical DR geometry.	27
3.3	Cylindrical DR $HE_{11\delta}$ mode internal fields and radiation pattern	28
3.4	Cylindrical DR $TM_{01\delta}$ mode internal fields and radiation pattern	28
3.5	Cylindrical DR $TM_{01\delta}$ mode relative field strength	29
3.6	Cylindrical DR $HE_{11\delta}$ mode relative field strength	30
3.7	Rectangular DR geometry.	31
3.8	Rectangular DR $TE_{\delta 11}$ mode internal fields and radiation pattern	32
3.9	Rectangular DR $TE_{\delta 11}^x$ mode relative field strength	33
3.10	Cylindrical DR and image theory	34
3.11	Cylindrical DR slot excitation.	38
3.12	Rectangular DR $TE_{11\delta}$ mode excitation	39
3.13	Slot aperture and co-planar waveguide shapes	39
3.14	Cylindrical DR 4-port arc-slot aperture coupling.	39
3.15	Rectangular slot in the ground plane.	40
3.16	$TE_{\delta 11}$ mode coaxial probe excited rectangular DR	41
3.17	Cylindrical DR coaxial probe excitation.	41
3.18	Cylindrical DR using conformal strip line coupling.	42
3.19	Cylindrical and rectangular DR microstrip line coupling.	42
3.20	Coplanar waveguide coupling to a cylindrical DR	43
3.21	Effects of amplitude and phase errors on AR	44

3.22	Cylindrical DRA using 4-port conformal strip excitation	46
3.23	4-port aperture coupled CP hybrid DRA with feeding circuit.	46
3.24	AR vs. mutual coupling between excitation ports	48
3.25	4-port slot excited CP DRA feeding circuit layout	49
3.26	hDRA RL and AR vs. frequency	51
3.27	Layout of four arc slot excited miniaturized hDRA	52
3.28	RL and AR vs. frequency of miaturised hDRA.	53
3.29	hDRA with a meandered slot ring PCB layout and geometry	54
3.30	hDRA with a meandered slot ring and back cavity	55
3.31	RL and realised gain of hDRA with a meandered slot ring	56
3.32	Measured AR of hDRA with a meandered slot ring	56
4.1	Unloaded Q-factor vs. fractional bandwidth.	63
4.2	$HE_{11\delta}$ mode Q_{rad} vs. r/h ratio.	63
4.3	$HE_{11\delta}$ mode k_0r vs. r/h ratio for $\epsilon_r = 12$ at 1385 MHz.	64
4.4	DR h vs. r for $HE_{11\delta}$ mode at 1385 MHz.	66
4.5	Available Q_{rad} vs. r/h at 1385 MHz.	66
4.6	Antenna feeding circuit.	68
4.7	Probe and conformal strip excited DR.	70
4.8	S_{11} and η_{ant} of 1 and 4-probe $HE_{11\delta}$ mode DR	71
4.9	AR and G_R bandwidth of 4-probe $HE_{11\delta}$ mode excited DR	72
4.10	G_R and AR beamwidth of 4-probe $HE_{11\delta}$ mode excited DR	73
4.11	Ground plane size impact on RL and η_{ant}	74
4.12	Ground plane size impact on AR and G_R BW	75
4.13	Ground plane size impact on AR and G_R beamdwidth	75
4.14	Simulated S_{11} and η_{ant} for 1-probe excited DR of $\epsilon_r = 12$	76
4.15	$HE_{11\delta}$ and $TM_{01\delta}$ modes far-field radiation patterns.	78
4.16	$HE_{11\delta}$ mode simulated and design Q-factor vs. r/h ratio	79
5.1	Annular dielectric resonator.	84
5.2	$HE_{11\delta}$ and $TM_{01\delta}$ modes resonant frequency $f_{0_{HE11}}/f_{0_{TM01}}$ ratio vs. r/h ratio	85
5.3	Unloaded annular DR S_{11} , realised gain and η_{ant}	86
5.4	Annular DR equatorial plane H -field	86
5.5	Various annular ring DR loadings and surface currents	88
5.6	Antenna response for various annular DR loads	89
5.7	Dual-row interleaved wedge-like periodic structure DR load	91
5.8	Loaded DR equatorial plane H -field patterns	94
5.9	Loading structure surface current density	95
5.10	Antenna response to loading structure h_1 variations	96

5.11	Stop-band frequency vs. loading structure h_1	96
5.12	Loading structure impact on antenna response	97
5.13	Antenna RHCP realised gain beamwidth.	98
5.14	Loaded DR RHCP (co-pol.) and LHCP (cross-pol.) radiation patterns	98
5.15	AR bandwidth for $\theta=0^\circ$, 30° and 60°	99
5.16	AR beamwidth at $f=1.16, 1.24, 1.3$ and 1.58 GHz.	99
5.17	Loading structure impact on feeding port mutual coupling.	100
5.18	Loaded annular DRA assembled and exploded views.	102
5.19	Ground plane PCB layered view.	102
5.20	Impedance matching network.	103
5.21	Impedance matching network impact on antenna response	104
5.22	Antenna cross-section	105
5.23	Effects of DR dielectric constant 5% error on antenna response.	106
5.24	Effects of air-gap t_{ag} on antenna response	106
5.25	Fabricated DR with a low-density foam insert.	107
5.26	Fabricated PCB top and underside views.	108
5.27	Fabricated loading structure unwrapped.	109
5.28	Assembled DRA.	110
6.1	Measurement setup in NSI spherical near-field chamber.	112
6.2	AUT ready for measurements.	112
6.3	NSI ANT-WGP-1.12-1.7 probe alignment.	113
6.4	Antenna feeding circuit measured S -parameters.	114
6.5	Feeding circuit measured amplitude errors.	114
6.6	Feeding circuit measured phase angles.	115
6.7	Feeding circuit phase angle errors	115
6.8	Unloaded annular DR S -parameter response.	116
6.9	Loaded annular DR S -parameter response.	117
6.10	Unloaded annular DR excitation port mutual coupling.	118
6.11	Loaded annular DR excitation port mutual coupling.	118
6.12	Measured and simulated RHCP directivity and realised gain	119
6.13	Simulated and measured vertical radiation pattern at $\phi = 0^\circ$	120
6.14	Measured AR beamwidth at $\phi = 0^\circ$	121
A.1	GNSS receiver functional block diagram.	141
A.2	Military handheld GPS receivers: PLGR+96, PLGR 3 and DAGR	142
B.1	Circularly polarised comb-shaped cylindrical DRA	144
B.2	Omnidirectional CP rectangular DRA.	144

B.3 Aperture fed CP rectangular DR. 146

C.1 *S*-parameter response of a cylindrical DRA optimised for the excitation mechanism and ground plane size 148

C.2 Cylindrical DRA assembled and exploded views. 150

C.3 Reflection coefficients and excitation ports mutual coupling. 151

C.4 RHCP total and realized gain. 152

C.5 Vertical plane CP radiation pattern 152

C.6 AR vs. elevation angle. 153

List of Acronyms

1D	One-Dimension or One-Dimensional
2D	Two-Dimensional
3D	Three-Dimensional
ADC	Analog to Digital Converter
AOI	Angle of Incidence
AR	Axial Ratio
AUT	Antenna Under Test
ARP	Antenna Reference Point
BB	Base Band
BOC	Binary Offset Carrier
BOR	Body of Revolution
BPF	Band-Pass Filter
BPSK	Binary Phase Shift Keying
BW	Bandwidth
C2	Command and Control
C/A	Coarse Acquisition
CAF	Canadian Armed Forces
CDMA	Code Division Multiple Access
CP	Circular Polarization
CPW	Coplanar Waveguide
DAC	Digital to Analog Converter
DF	Direction Finding
DN	Decoupling Network
DR	Dielectric Resonator
DRA	Dielectric Resonator Antenna
DRDC	Defense Research and Development Canada
DSP	Digital Signal Processing
DWM	Dielectric Waveguide Model

EBG	Electromagnetic Band Gap structure
EDC	Effective Dielectric Constant method
EM	Electromagnetic
EMA	Elevation Masking Angle
EMI	Electromagnetic Interference
ESA	European Space Agency
FDMA	Frequency Division Multiple Access
FEM	Finite Elements Method
FOC	Full Operational Capability
fPCB	Flexible Printed Circuit Board
FRPA	Fixed Reception Pattern Antenna
GDOP	Geometric Dilution of Precision
GEO	Geostationary Earth Orbit
GLONASS	Globalnaya Navigatsionnaya Sputnikovaya Sistema
GNSS	Global Navigation Satellite System
GPS	Global Positioning System
hDRA	Hybrid Dielectric Resonator Antenna
HE	Hybrid Electric
HFSS	High Frequency Structural Simulator
HPBW	Half-Power Beamwidth
IF	Intermediate Frequency
IGS	International GNSS Service
IL	Insertion Loss
INS	Inertial Navigation System
IOC	Initial Operational Capability
IS	Interference Suppression
LHCP	Left Hand Circular Polarization
LHS	Left-Hand Side
LNA	Low Noise Amplifier
LO	Local Oscillator
MCX	Micro Coaxial Connector
MEO	Mid-Earth Orbit
MDWM	Modified Dielectric Waveguide Model
MoM	Method of Moments
MOPS	Minimum Operational Performance Standards
MWM	Magnetic Wall Model
N	North
NDS	Nuclear Event Detection System

NF	Noise Figure
NSI	Near-field Systems Inc.
Q-factor	Quality Factor
PCB	Printed Circuit Board
PCO	Phase Center Offset
PEC	Perfect Electric Conductor
PGM	Precision Guided Munitions
PML	Perfectly Matched Layer
PVT	Position, Velocity and Time
RAM	Radar Absorbing Material
RF	Radio Frequency
RHCP	Right Hand Circular Polarization
RHS	Right-Hand Side
RL	Return Loss
RLC	Resistance-Inductance-Capacitance
RSNS	Regional Satellite Navigation System
RTCA	Radio Technical Commission for Aeronautics
SBAS	Satellite Based Augmentation Systems
SIW	Substrate Integrated Waveguide
SMT	Surface Mounted
SNF	Spherical Near-Field scanner
SU	Soviet Union
SWR	Standing Wave Ratio
TE	Transverse Electric
TLM	Transmission Line Model
TM	Transverse Magnetic
UI	User Interface
UNK	Unknown
USAF	United States Air Force
VNA	Vector Network Analyzer
vs.	Versus
VSWR	Voltage Standing Wave Ratio

1 Introduction

During the last decade a requirement for a compact wideband antenna covering all the Global Navigation Satellite Systems (GNSS) occupied bands has developed. The requirement is driven by an increasing number of GNSS signals and omni-present use of the space-based navigation systems in both civilian and military domains alike. In addition to the increased bandwidth dictated by the new signals, the GNSS antennas are also expected to be more compact in size, to provide a broader beamwidth and better overall performance for specific applications.

The work presented in this thesis consists of an investigation and experimental validation of a compact fixed reception pattern antenna (FRPA) for industrial and defense applications. It supports a dual-sense circular polarisation covering the entire GNSS band from about 1164 to 1606 MHz. The antenna concept is based on a periodic structure loaded annular ring dielectric resonator (DR). The concept is novel and demonstrates improvements over the current state-of-the-art.

1.1 Motivation

Access to multiple GNSS signals increases accuracy, integrity, reliability and availability of the GNSS based navigation in general. In particular, it provides a multi-layered and redundant global coverage whereas the signal frequency diversity reduces receiver susceptibility to the electromagnetic interference (EMI).

In case of the military applications access to the Global Positioning System (GPS), as one of the GNSS, is one of the key military capability enablers. From the historical perspective, a milestone in the area of the military satellite based navigation was the operationalization of low-cost compact receivers and Iner-

tial Navigation Systems (INS) in the first decade of this century [1, 2]. Such technologies enabled development of the precision guided munitions (PGM) and autonomous vehicles capable of performing missions in all weather and visibility conditions and with an increased effectiveness. However, as the reliance on GPS increased, development of the disruptive technologies and capabilities followed closely [1, 3].

1.2 Problem definition

The antenna is one of the key elements in the GNSS receiver system. In the past a number of antennas were developed to cover only GPS L1 and L2 bands. A smaller number of antennas capable of receiving all the GNSS signals is also reported. However, the number of compact high performance antennas suitable for industrial and defense applications was found to be small.

In addition to the generic GNSS receiver antenna requirements, a growing number of industrial, defense and security applications are being developed for the GNSS spectrum monitoring and non-traditional use of the GNSS signals. Antennas for such applications need to provide polarisation diversity in addition.

1.3 Scope

The scope of this thesis is an investigation and experimental validation of a dual-sense compact GNSS FRPA for industrial and defense applications. The work covers a 4-port antenna design based on a cylindrical DR. The feed network is a pre-existing 4-port feed network designed for a similar antenna. Enhancing the performances of the cylindrical DR is the primary focus of this work. A hypothesis is that engineered surfaces based on the periodic structures could be used to load DR to extend the radiation bandwidth.

1.4 Methodology

The research methodology is a combination of comparative, quantitative, qualitative analytical and experimental methods. First, a study of the GNSS antenna requirements was undertaken. The study was based on the literature covering the subjects of the GNSS user segment, GNSS receiver antenna and satellite communications. The next step was literature survey to investigate the current state-of-the-art. Findings from these two steps provided insight

into to the GNSS antenna types, design concepts, performance requirements and fabrication technologies. An antenna type and concept were then selected based on the likelihood of meeting the thesis objectives.

Based on the selected type and concept, an antenna was then designed and simulated. The performance results were analyzed and the design was modified accordingly. The concept was modified and refined until the simulated performances met the thesis objectives or the simulation tool limitations were exceeded. Once the design was finished, a parametric analysis was carried out to understand sensitivity of the design to material imperfections, fabrication and assembly tolerances. The design was then further modified to minimize the impact of the same.

The last step was an experimental validation of the new antenna concept. The experimental data were analyzed to assess the validity of the simulation results and compared against the thesis objectives and the state of the art.

1.5 Main contributions

The main contribution of this thesis is a novel antenna concept based on an annular DR incorporating conformal periodic electromagnetic structures (aka. engineered surfaces). The novelty is based on the following specific contributions:

- An antenna concept based on a combination of an annular DR and conformal engineered surfaces.
- Use of the engineered surfaces to affect antenna gain, input impedance and axial ratio responses.
- Use of the engineered surfaces to affect DR resonant frequency and mode.

1.6 Thesis organization

This thesis consists of 7 chapters, including this chapter, and 3 appendices. Chapter 2 presents a review and analysis of the GNSS antenna properties and performance requirements. Additional supporting information for this chapter are provided in Appendix A. Chapter 3 presents the literature review covering the dielectric resonator antenna (DRA) and use of such antennas in the GNSS domain.

Chapter 4 is dedicated to a cylindrical DRA design process. The effects of the thin wire probe excitation, conformal strip excitation and the finite size ground plane on the CP DRA performances are also reported here. In Chapter 5 antenna performance enhancements, optimization process, parametric analysis, fabrication considerations, final design proposal and antenna fabrication are covered. Chapter 6 presents the measurement results of a fabricated antenna, analysis and discussion. Finally, Chapter 7 provides conclusions and proposes possible future work concerning the material presented in this thesis.

2 GNSS antenna properties and requirements

This chapter presents the GNSS antenna properties and performance requirements. The presented material provides background information based on the thesis problem definition and scope. Additional supporting information for the presented material are given in Appendix A.

This Chapter starts with a brief descriptions of the conventions used in the thesis and follows with the GNSS concept description in section 2.2. Section 2.3 defines the GNSS antenna impedance bandwidth requirements whereas section 2.4 covers the radiation pattern and beamwidth. The radiation parameters such as directivity and gain are defined in section 2.5 followed by the polarisation and axial ratio in section 2.6. The phase center and group delay are defined and described in section 2.7. A chapter summary is given in section 2.8.

2.1 Conventions

Conventions used in this thesis are based on *Balanis* [4] and *Rao et al* [5], which use the left-hand spherical coordinate system defined by the radius r and θ and ϕ angles that originate at antenna's phase center, see Figure 2.1. In addition to these terms, which are defined in the above mentioned references, additional spatial terms commonly used in the GNSS antenna domain are introduced here. Those are the elevation and azimuth angles β and ψ , respectively, and antenna Zenith, Horizon and Nadir. In some cases the Zenith is also referred to as the antenna boresight.

The spatial terms are aligned with a right-hand references system (x',y',z') , which for a convenience also originates at the antenna phase center. The two

coordinate systems also share the primary axes where $x=x'$, $y=y'$ and $z=z'$. Obviously, the $x-y$ and $x'-y'$ planes are co-planar.

The elevation angle β is measured relative to the $x'-y'$ plane, or the Horizon, and it has a simple relation to θ where $\beta = \pi/2 - \theta$. The azimuth angle ψ is measured in the $x'-y'$ plane clockwise relative to the geodetic North (N), which is aligned with the x' -axis. The antenna Zenith is at $\beta=90^\circ$ or $\theta=0^\circ$, and Nadir is at $\theta=180^\circ$ or $\beta=-90^\circ$. The Horizon is obviously at $\theta=90^\circ$ or $\beta=0^\circ$ and coincides with the $x-y$ and $x'-y'$ planes.

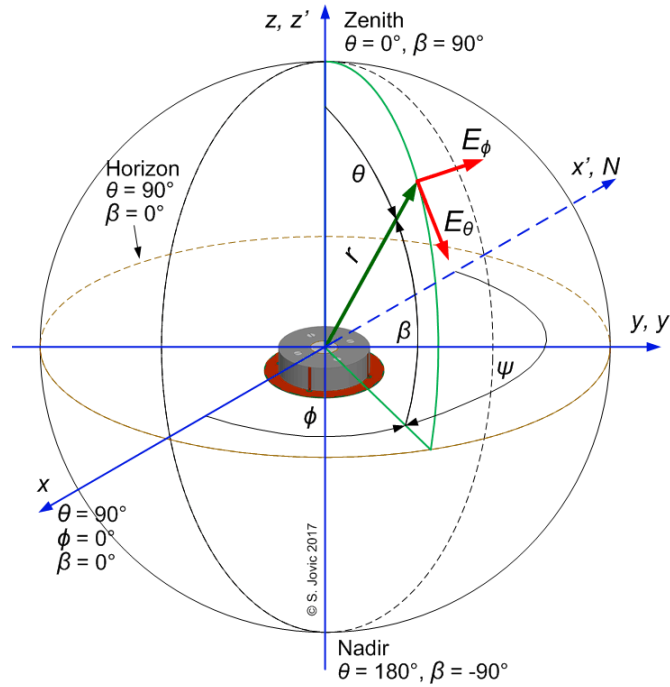


Figure 2.1: Field vectors and angle conventions in the spherical coordinates.

2.2 GNSS concept

The GNSS concept of navigation is based on one-way communication from multiple space-based transmitters, i.e. satellites, to a receiver on or relatively close to the Earth surface (Figure 2.2). An antenna is the first element in the signal acquisition and processing chain and it is required to simultaneously

receive signals from multiple satellites both spatially and spectrally diverse.

The satellites are in constant motion relative to a receiver and during one-half of an orbital period a GNSS satellite traverses an entire hemisphere. In addition, the performance of a navigation solution strongly depends on the instantaneous satellite geometry relative to a receiver. Due to such conditions, a GNSS antenna needs to have a uniform performance over its entire upper hemisphere. At the same time, it is desirable for an antenna to provide maximum rejection of the in-band multi-path and interference signals, which are also referred to as spatial and frequency filtering [5, pp.17-28], see Figure 2.2.

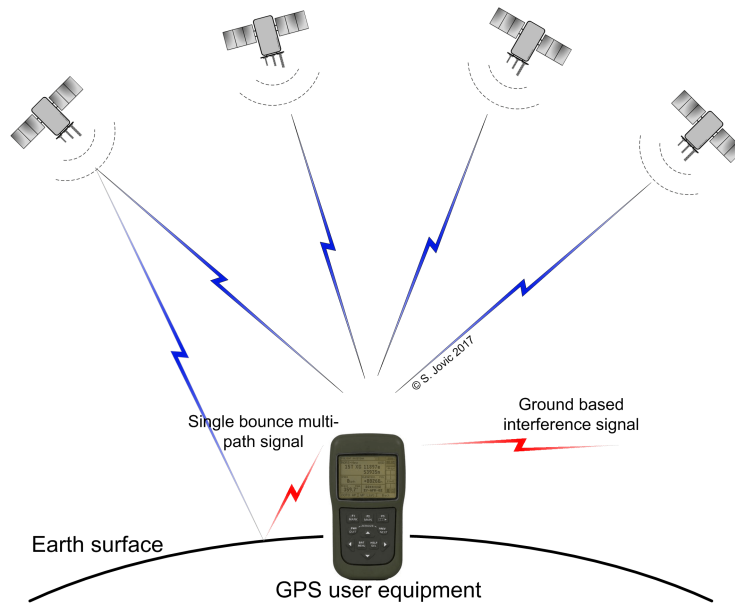


Figure 2.2: Basis of the GNSS navigation concept

2.3 Impedance bandwidth

The impedance bandwidth (BW) is defined as a frequency range over which at least 89% of the antenna received energy is transferred to a receiver and less than 11% of reflected or absorbed [5, pp.76]. The 89% corresponds to antenna RL of 9.5 dB. This slightly differs from the commonly used 10 dB RL impedance BW, however, no explanation was given.

To receive all the GNSS bands, an antenna needs to cover frequencies from 1164 to 1300 MHz and 1559 to 1606 MHz as shown in section A.3. This implies that an antenna can be of a dual-band or wideband design. If an antenna is dual-band, the lower band BW needs to be about 11% while for the upper band requires about 3% BW. In case of a wideband design, the required BW is about 442 MHz (1164 to 1606 MHz) or about 32%.

2.4 Radiation pattern and beamwidth

A receiver is required to have in its view a minimum of 4 satellites to estimate its position [1]. In addition, the statistical uncertainty of a position solution is a function of the geometry between the signal transmitting satellites and a receiver antenna. The geometric dilution of precision (GDOP) is a parameter that expresses the statistical impact of the geometry on these uncertainties.

Based on the GDOP definition, for the least geometry impact on the position estimate in the 2D space, the satellites need to be located at the horizon and with a 90° separation angle in between relative to a receiving antenna [1, pp.661-707]. In case of the 3D space, at least one satellite needs to be located exactly at the zenith. Therefore, from the GDOP aspect, an antenna needs to provide the same performance from the horizon to the zenith, which is not a case in the point-to-point communications and radars. This requirement makes the GNSS antennas unique.

2.4.1 Elevation masking angle

To mitigate the undesired effects of the ground based multipath and interference signals, an antenna is required to minimize its directive gain close to and below the horizon. The cut-off angle is called the low elevation masking angle (EMA). Figure 2.3 shows GNSS antenna ideal and typical radiation patterns for $EMA = 15^\circ$. Obviously EMA has a negative impact on GDOP. However, the GNSS signals from the satellites near the horizon are undesired due to a high attenuation and other distortions owing to the propagation conditions near the Earth's surface [5, pp.17-28].

The literature does not provide a rigorous derivation for EMA, instead, the EMA is provided as an empirical value typically ranging from 5° to 10° . According to [5, pp.20-21 and 45-50], EMA is based on antenna's exploitation conditions, host platform, anticipated signal multipath conditions, receiver processing gain, antenna front-end noise figure (NF) and anticipated ground

based interference. In case of the antennas designed for very high altitude and space applications, EMA may have different requirements.

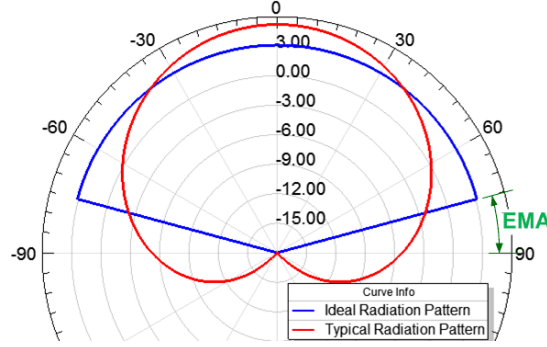


Figure 2.3: GNSS antenna ideal and typical radiation pattern.

Therefore, a GNSS antenna requires the highest permissible beam-width but due to the exploitation conditions the elevation plane beamwidth $\alpha_{\theta EL}$ is determined by the EMA (eq. 2.1). The azimuth plane beamwidth $\alpha_{\phi AZ}$ is obviously 360° , as implied earlier.

$$\alpha_{\theta EL} = \pi - (2 \text{ EMA}) \quad (2.1)$$

2.5 Antenna radiation parameters

In this section directivity, radiation efficiency, gain, radiation pattern and beamwidth for the GNSS antenna will be introduced. *Balanis* in [4, pp.42-69] provides a comprehensive coverage of the subjects whereas [5, pp.17-28] covers the specific aspects applicable to the GNSS antennas. An antenna is required to radiate only in the upper hemisphere providing a broad beamwidth and maximum radiation suppression below EMA. A narrow-beam antenna is undesirable since it impedes acquisition of the low elevation satellites needed for a good GDOP.

2.5.1 Directivity

Antenna directivity D varies inversely with the antenna beamwidth. Eq. 2.2 gives an approximation for D as a ratio of areas of an ideal sphere, which represents an isotropic radiator, and a body enclosed by $\alpha_{\phi AZ}$ and $\alpha_{\theta EL}$ an-

gles, where $\alpha_{\phi_{AZ}}$ and $\alpha_{\theta_{EL}}$ are antenna's azimuth and elevation beamwidths, respectively [5, pp.17-28].

$$D = 10 \log \left[\frac{4\pi}{\alpha_{\phi_{AZ}} \alpha_{\theta_{EL}}} \right] \quad [dBi] \quad (2.2)$$

To investigate the EMA impact on antenna's directivity, an antenna radiating omni-directionally in the horizontal plane ($\alpha_{\phi_{AZ}} = 360^\circ$) and having the elevation plane beamwidth $\alpha_{\theta_{EL}} = 180^\circ - (2 \times EMA)$ is assumed. Figure 2.4 shows the directivity of such an antenna as a function of EMA. This figure shows that for $0^\circ \leq EMA \leq 20^\circ$ the directivity would range $3.0 \leq D \leq 4.1 \text{ dBi}$. However, as stated earlier eq. 2.2 is a approximation that assumes an ideal radiation pattern (Figure 2.3). Obviously, such antennas do not exist.

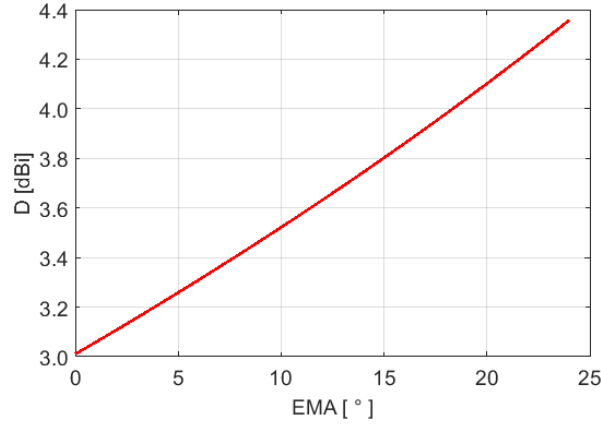


Figure 2.4: Antenna directivity vs. the low elevation masking angle.

2.5.2 Gain and radiation efficiency

The gain and beamwidth are considered two key performance parameters according to [5, pp.17-28]. To differentiate between the antenna absolute gain, which in case of the GNSS antennas frequently includes a low noise amplifier (LNA) as an active component, the term directive gain is used to describe the gain component dominated by the antenna directivity [5].

Rao et al in [5, pp.17-28] introduces antenna directive gain G , which is directivity corrected for the radiation efficiency factor η_{ant} (eq. 2.3). η_{ant} is a product of the impedance mismatch, feed network losses, polarisation losses,

conductor and dielectric losses, eq. 2.4. The feed network losses factor η_f includes losses due to imperfections of the CP generation network and the impedance mismatch between the antenna and the feeding network. The subject of antenna polarisation efficiency is further covered in section 2.6.

$$G = \eta_{ant} D \quad (2.3)$$

$$\eta_{ant} = \eta_i \eta_f \eta_p \eta_r \eta_d \quad (2.4)$$

Where

- η_i – Impedance mismatch factor
- η_f – Feed network mismatch and CP generation losses factor
- η_p – Polarisation losses factor
- η_r – Antenna conductor losses factor
- η_d – Dielectric losses factor

Since eq. 2.3 is an approximation but adequate for the narrow beam antennas, η_{ant} and D are presented as scalar values independent of θ and ϕ . However, for a broad-beam antenna parameters that vary with θ and ϕ need to be considered, which are primarily the polarisation losses η_p and directivity D . Hence, eq. 2.3 can be expressed in terms of θ and ϕ , see eq. 2.5. Eq. 2.5 introduces the realised gain G_r , which is antenna gain but as a function of θ and ϕ [6].

$$G_r(\theta, \phi) = \eta_{ant}(\theta, \phi) D(\theta, \phi) \quad (2.5)$$

For a receiver to maintain a minimum carrier to noise ratio (C/N_0) under all operational conditions, the antenna minimum realised gain needs to be met from EMA to zenith (Figure 2.3) [1, 5, 7], which is also referred to as the antenna minimum gain beamwidth [5, pp.17-18]. For an ideal antenna having $EMA = 5^\circ$, the realised gain is uniform at 3.25 dBic for $0^\circ \leq \theta \leq 85^\circ$ and it abruptly drops below EMA . However, such radiation pattern is obviously unattainable. A typical antenna has the highest realised gain at the zenith that gradually decreases towards the horizon, see Figure 2.3.

2.5.3 Antenna gain performance parameters

Minimum gain beamwidth:

The term half-power beamwidth (HPBW) was intentionally avoided in this section. HPBW is indicative of a GNSS antenna beamwidth only in part since the GNSS antennas have different radiation pattern requirements, as

covered earlier. *Rao et al* in [5, pp.17-28] cover this subject but do not provide a substitution for HPBW. Hence, a new performance measure is needed to quantify the GNSS antenna beamwidth.

According to [5, pp.84-85], a more indicative performance measure of a GNSS antenna beamwidth quality is the minimum gain beamwidth. The minimum gain beamwidth is an angle in the upper hemisphere where an antenna meets the minimum realised gain requirements. However, the minimum gain requirements are not standardized as they depend on a receiver. To simplify this issue for the purpose of this thesis, the minimum gain beamwidth indicates an angle over which $G_r \geq 0$ dBic.

Minimum gain BW:

In addition to the beamwidth, which is usually specified at a specific frequency, a band over which an antenna meets the minimum realised gain needs to be considered as well. The minimum realised gain BW indicates a frequency range over which $G_r \geq 0$ dBic and it will be used in this thesis as a performance indicator. The minimum gain BW in the GNSS antenna context is mentioned in [5, pp.76], however, this parameter is not commonly used in the other literature. Instead, the antenna maximum realised gain at a band center frequency is the most frequently quoted.

2.5.4 Antenna gain performance requirements

The antenna main lobe radiation, radiation suppression from EMA to horizon and the back lobe radiation are covered in the literature usually as antenna performance parameters. However, no rigorous derivations are provided for the minimum performance requirements. Obviously, the back lobe radiation is undesired regardless of the polarisation and as such needs to be minimized.

In the Radio Technical Commission for Aeronautics (RTCA) Minimum Operational Performance Standards (MOPS) for an active antenna operating in the GPS L1 and Galileo E1 bands used for navigation of civilian aircraft [8], minimum and maximum realised gain values are specified for EMA = 5°, Table 2.1. A similar MOPS published by European Commission provides more comprehensive requirements for the antennas used on commercial aircraft operating in the GPS L1 and L5 and Galileo E1 and E5 bands [9], Table 2.2. The document specifies the minimum and maximum directive gain relative to the 0 dBic gain at the antenna zenith. However, the document does not state the minimum and maximum absolute realised gain requirements at the

zenith. The EMA is not specified either. In addition, this MOPS specifies the Axial Ratio (AR) requirements separately and only at the antenna zenith. Thus, the gain values would need to be corrected for the polarisation losses. It is also not clear why the minimum gain is specified below EMA considering that the maximum suppression is always desired in that region. Reference [7, pp.340-341] also provides similar specifications but only applicable to GPS L1 coarse acquisition signal (C/A), 1575.42 MHz \pm 1 MHz. Requirements for the ground and surface GNSS antennas do not appear to be standardized.

Table 2.1: Realised gain requirements for airborne GNSS E1 and L1 band antennas (from [8]).

Elevation Angle [$^{\circ}$]	Max. Gain [dBic]	Min. Gain [dBic]
< -30	-10	-
0	-2	-7.5
5	5	-4.5
10	-	-3
> 15	-	-2

Table 2.2: GNSS antenna relative directive gain requirements (from [9]).

θ [$^{\circ}$]	Max. Gain [dB]	Min. Gain [dB]
90	-7	-10
85	-5	-8.5
80	-3	-7
75	-1	-5.5
60	-0.75	-3.5
≤ 15	0	-2.5

2.6 Polarisation

All GNSS signals are RHCP and to eliminate the polarisation mismatch losses, a receiving antenna has to have the same polarisation. There are three key advantages of CP vs. linear polarisation in this case: 1) Insensitivity to the relative orientation between the satellite and receiver antennas, 2) decreased sensitivity to Earth's ionosphere effects on polarisation and, 3) inherent dis-

crimination between the direct and single-bounce reflected signals.

Relative orientation between the satellite and receiver antennas is dynamic. Obviously, circularly polarized antennas do not depend on antenna alignment to minimize the polarisation losses as long as the sense of polarisation is maintained. Based on [5, pp.5-6], [7, pp.49-52] and [10, pp.589-599], refractory properties of the ionosphere induce a polarisation shift to electromagnetic fields. CP signals are less affected by such a shift.

GNSS signals reflected from conductive surfaces can be received by a receiver. The multi-path signals are an exact replica of the direct signals but with a small time delay due to the propagation path difference and a switched polarisation sense. The reflected signal amplitude is usually reduced as well. GNSS receivers can effectively reject the multi-path signals at the digital signal processing (DSP) stage, however, those signals add to the receiver NF, which reduces signal C/N_0 . If both the receive antenna and the reflected signals have perfect CP but of the opposite sense, the reflected signal is completely rejected by the antenna. Thus, use of CP allows simple but very effective suppression of the single bounce multi-path signals. Reference [10, pp.599-614] covers the multipath issue extensively.

2.6.1 Polarisation axial ratio

For a proper signal reception, a receiver antenna polarisation needs to match the satellite antenna polarisation. However, in practice neither of the antennas have a perfect CP due to imperfections of the antenna CP generating circuitry and fabrication tolerances. The CP antennas are in reality elliptically polarized and CP is considered a special case of the elliptical polarisation.

AR indicates antenna polarisation efficiency and it is a metric of several critical GNSS antenna performance parameters [5]. AR ranges from 0 dB to ∞ where 0 indicates perfect CP whereas ∞ indicates a perfect linear polarisation. The AR can vary significantly with the elevation and azimuth angles depending on the antenna design. In general, the AR degrades with the θ angle for all antennas. The GPS Block II and IIA satellite transmit antennas have $AR \leq 3.2$ dB and it varies with the angle θ [5].

Figure 2.5 shows the far-field magnitude projection of a time-varying electric field $E(t)$ on a plane perpendicular to the direction of propagation at a point z_0 . z_0 is a point on the axis of propagation $n\lambda$ away from the antenna

phase center, where $n = 0, 1, 2, 3 \dots$ and λ is the free-space propagation wavelength. E_{min} and E_{max} are the minimum and maximum magnitudes, respectively, of the electric field $E(t)$. E_{0x} and E_{0y} are the maximum projections of E_{min} and E_{max} on the major axes x and y [4, pp.74]. Thus, AR is a ratio of two orthogonal components E_{min} and E_{max} , eq. 2.6 [5, pp.8].

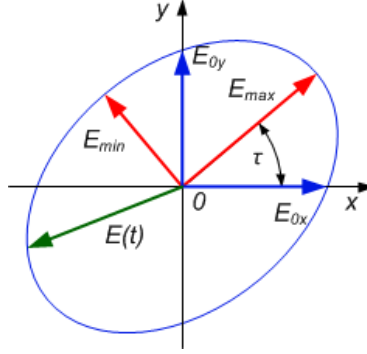


Figure 2.5: Far-field polarisation ellipse.

$$AR(\theta, \phi) = 20 \log \left(\frac{E_{max}}{E_{min}} \right) \quad (2.6)$$

The polarisation ellipse, Figure 2.5, is affixed to the antenna frame of reference. Eq. 2.7 [4, pp.74] is the polarisation tilt angle τ or the angle of ellipse major-axis. The polarisation tilt angle is important when considering the polarisation mismatch between two elliptically polarized antennas. $\Delta\Phi$ is the time-phase difference between E_{0x} and E_{0y} components [4, pp.73].

$$\tau = \frac{\pi}{2} - \frac{1}{2} \tan^{-1} \left[\frac{2E_{0x}E_{0y}}{E_{0x}^2 - E_{0y}^2} \cos(\Delta\Phi) \right] \quad (2.7)$$

2.6.2 Polarisation efficiency and polarisation mismatch loss

If both receive and transmit antennas have perfect CP ($AR = 0$ dB), there would be no losses due to polarisation mismatch ($\eta_p = 1$). In reality both antennas are elliptically polarized ($AR > 0$ dB) and both antennas have a different polarisation tilt angle τ due to different frames of reference. The facts that AR is a function of the signal angle of incidence (AOI) and signal frequency f need to be considered as well.

The polarisation mismatch factor is given by eq. 2.8 [5, pp.12], where AR_T and AR_R are AR of transmit and receive antennas, respectively. $\Delta\tau$ is a relative tilt angle between the major axes of the receive and transmit antennas' polarisation ellipses. The relative tilt angle $\Delta\tau$ varies over its full range due to the relative motion between the antennas. Thus, a practical η_p factor can be estimated only for the worst case scenario where the maximum AR values for both antennas and $\Delta\tau = 90^\circ$ are used (i.e. the major axis of the polarisation ellipses are orthogonal).

$$\eta_p = \frac{1}{2} + \frac{4AR_R AR_T + (AR_T^2 - 1)(AR_R^2 - 1) \cos(2\Delta\tau)}{2(AR_T^2 + 1)(AR_R^2 + 1)} \quad (2.8)$$

For purposes of an antenna design, the transmit antenna can be disregarded, or vice-versa. Eq. 2.9 gives an antenna polarisation loss factor as a function of its own AR. The polarisation mismatch loss L_p is another way to express the polarisation mismatch factor η_p , eq. 2.10 [5, pp.12]. Figure 2.6 shows the worst case polarisation losses ($\Delta\tau = 90^\circ$) at the receive antenna as a function of antenna own AR for various AR_T values. The case of $AR_T = 0$ dB represents also the receive antenna only polarisation losses as a function of its own AR.

$$\eta_p(\theta, \phi) = \frac{1}{2} + \frac{AR(\theta, \phi)}{AR^2(\theta, \phi) + 1} \quad (2.9)$$

$$L_p = -10 \log(\eta_p) \quad (2.10)$$

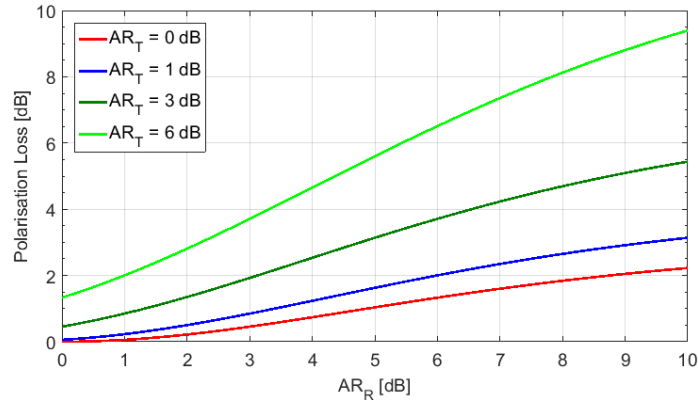


Figure 2.6: Antenna polarisation losses vs. AR.

2.6.3 Axial ratio and interference suppression

In addition to indicating antenna polarisation efficiency, AR also indicates antenna's ability to suppress the single-bounce multipath and other interference signals. Three cases are considered for the interference signal polarisation: left-hand circular polarisation (LHCP), RHCP and linear. The interference suppression (IS) is a strong function of a signal AOI at the receive antenna.

The single-bounce multipath signals are the primary source of the LHCP interference based on the fact that a reflected signal changes its polarisation sense (RHCP to LHCP) at the point of reflection. Hence, suppression is usually high above EMA but not as effective below EMA due to the AR degradation at the low elevation angles. Figure 2.7 shows that a receive antenna has the highest multipath suppression when $\Delta\tau = 90^\circ$ and lowest when $\Delta\tau = 0^\circ$ against $AR_T = 1.8$ dB. When reflected off a perfectly smooth surface, the multipath signals retain AR of the transmit antenna. If a reflective surface is rough the AR gets degraded. In such cases the AR_T and $\Delta\tau$ are unknown and for a practical purpose only the worst case can be assumed.

Equations 2.11, 2.12 and 2.13 give antenna's LHCP, RHCP and linear interference suppression as a function of the receive and transmit antenna AR, AR_R and AR_T , respectively. In all cases it is assumed that the transmit and receive antennas' polarisation axes are aligned ($\Delta\tau = 0^\circ$), which is the worst case scenario or the minimum suppression. Suppression of RHCP signals is obviously very low, especially above EMA. In the case when an interference signal is linearly polarized $AR_T = \infty$. Since the GNSS antennas usually operate on a ground plane where polarisation is near linear, they are very susceptible to the linearly polarized interference.

$$IS_{LHCP} = -10\log \left[\frac{1}{2} + \frac{-4AR_R AR_T + (AR_T^2 - 1)(AR_R^2 - 1)}{2(AR_T^2 + 1)(AR_R^2 + 1)} \right] \quad (2.11)$$

$$IS_{RHCP} = -10\log \left[\frac{1}{2} + \frac{4AR_R AR_T + (AR_T^2 - 1)(AR_R^2 - 1)}{2(AR_T^2 + 1)(AR_R^2 + 1)} \right] \quad (2.12)$$

$$IS_{Lin} = -10\log \left[\frac{1}{2} + \frac{(AR_R^2 - 1)}{2(AR_R^2 + 1)} \right] \quad (2.13)$$

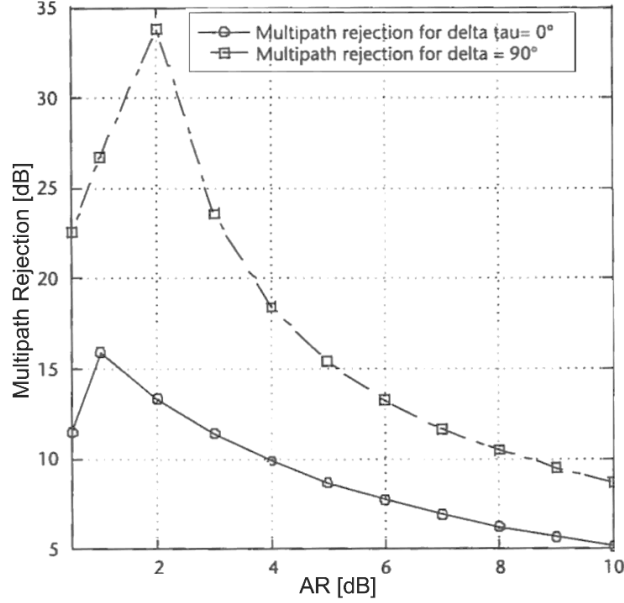


Figure 2.7: Receive antenna multipath signal suppression vs. AR (from [5]).

2.6.4 Axial ratio performance parameters and requirements

In the commercial specifications and frequently in the literature, AR is usually specified only at the antenna zenith and center frequency. However, for the higher performance and multi-band antennas this is inadequate since AR is a strong function of both θ and f . To cover this issue, *Rao et al* [5] introduce terms such as AR beamwidth and AR BW. These two terms specify the beamwidth and BW over which an antenna meets the $AR \leq 3$ dB performance. Ideally AR BW and beamwidth should match the minimum realised gain BW and beamwidth, respectively.

Based on [9], the commercial aircraft GNSS antennas require $AR = 3$ dB or less at the zenith. In [5, pp.11-12] AR performance for *NovAtel 704X* antenna is provided as an example where the same antenna is qualified as “extremely good” (Table 2.3).

Table 2.3: NovAtel 704X antenna AR at GPS frequencies (from [5]).

GPS band	Elevation Angle [°]	AR [dB]
L1	>45	1
L1	15	1.4
L1	5	1.6
L2	>45	2.0
L2	15	3.8
L2	5	5.0

2.7 Antenna phase center and group delay

2.7.1 Phase center

A receiver estimated position is the position of the antenna phase center. However, since a receiver cannot estimate antenna's true phase center an assumption is made about its physical location. Such assumptions are adequate for most of the applications, however, for applications where a high positioning accuracy or signal phase are required such as timing, geodesy and direction finding (DF), the true phase center position needs to be known. Antennas for such applications have an external antenna reference point (ARP) that does not coincide with the true phase center. To remove that error in an estimated position, a receiver needs to know the phase center offset (PCO) relative to ARP. International GNSS Service (IGS) defines ARP that is external to the antenna and coincides with the origin of antenna's frame of reference [5, pp.29].

In the electromagnetic sense, the phase center is the reference point from where an antenna is said to radiate. It is defined as a center of a sphere where the phase $\Phi(\theta, \phi)$ of an electric field $E(\theta, \phi)$ is the same regardless of the θ and ϕ angles. It is also called the equiphase sphere (Figure 2.8). The phase center position p_0 is determined by the electromagnetic properties of the antenna. However, the material imperfections and fabrication tolerances significantly affect its location. The cumulative effect is an irregular non-spherical equiphase contour that makes p_0 dependent on the signal AOI and frequency, see Figure 2.8.

The p_0 can be a fixed point over a narrow range of θ and ϕ angles and a narrow frequency band, which can be adequate for some antennas. However, for a GNSS antenna, the position of p_0 will vary as a function of θ , ϕ and f .

An incorrect position of the phase center introduces the phase pseudorange error Δr_{PR} . If left uncorrected, it adds to the total receiver position uncertainty. The phase center is hard to model and it is usually determined experimentally [4, pp.800]. In the case of the GNSS antennas used for a positioning precision under 10 cm, the phase center can be determined only experimentally [5, pp.31-32].

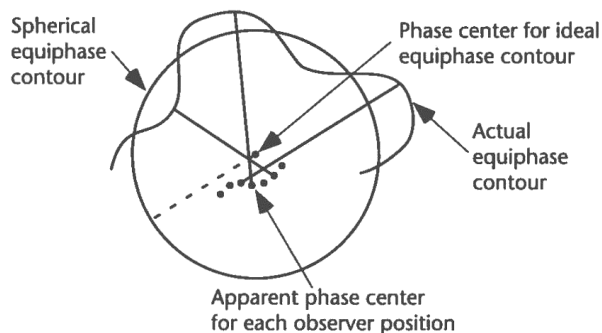


Figure 2.8: Equiphase contour and antenna phase center (from [5]).

2.7.2 Group delay

A wideband or multi-band GNSS antenna induced group delay has two components: The first due to the antenna BW and the second due to the signal AOI. The BW induced group delay τ_{BW} reduces signal C/N_0 through the distortion and spectral quality of the Binary Phase Shift Keying (BPSK) and Binary Offset Carrier (BOC) modulated signal having 20 MHz or more BW [5, pp.36].

The variations of the AOI induced group delay τ_{AOI} , manifest as timing errors between the signals from different AOI, which induces pseudo-range errors. Considering that τ_{BW} and τ_{AOI} have different origins, it is proposed in [5, pp.35-39] that they are analyzed separately.

Bandwidth induced group delay:

The BW induced group delay τ_{BW} is a measure of a relative time within antenna BW and it is defined as a derivative of the transfer phase response versus frequency $\Phi(\omega)$, eq. 2.14. In practical terms, the group delay is the maximum time difference between signal phases $\Phi(f)$ at any two frequencies

within a band of interest, eq. 2.15. To isolate the BW induced group delay from AOI one, *Rao et al* [5] propose that the BW induced group delay is measured at antenna's boresight.

$$\tau_{BW} = \frac{d\Phi(\omega)}{d\omega} \quad (2.14)$$

$$\tau_{BW} = \left| \frac{\Phi(f_i)}{f_i} - \frac{\Phi(f_j)}{f_j} \right| \frac{1}{2\pi} \quad (2.15)$$

In [5, pp.36-37] it is mentioned that for a passive GNSS antenna, $\tau_{BW} \leq 2$ ns is acceptable within a signal BW. The literature does not cover or specify τ_{BW} requirements between different GNSS signals and bands. It is not clear why this subject is not covered considering receivers that track simultaneously signals from multiple bands would be affected. The τ_{BW} for such cases would be significantly larger considering that the total BW for τ_{BW} could be as high as 442 MHz (i.e. 1164 to 1606 MHz).

Angle of incidence induced group delay:

The AOI induced group delay τ_{AOI} is the time difference between the signal phases at two distinctive AOI measured within antenna's main lobe and at the same frequency. Obviously, it is related to the phase center variation covered earlier. In [5, pp.37], τ_{AOI} is also referred to as the differential group delay. Eq. 2.16 gives τ_{AOI} calculated from two phase values $\Phi_1(\theta, \phi)$ and $\Phi_2(\theta, \phi)$ where $0^\circ \leq \theta \leq (90^\circ - EMA)$ and $0^\circ \leq \phi \leq 360^\circ$. The phase difference is absolute, as in case of eq. 2.15.

$$\tau_{AOI} = \left| \frac{\Phi_1(\theta, \phi) - \Phi_2(\theta, \phi)}{2\pi f_c} \right| \quad (2.16)$$

Both the τ_{AOI} and τ_{BW} induce a pseudorange error Δr_{PR} , eq. 2.17, which adds to the total receiver position uncertainty. In eq. 2.17 propagation velocity v_p is used instead of the speed of light c , see section 2.7.1. To minimize the impact of τ_{AOI} , an antenna has to have a uniform group delay response independent of signal AOI. In [5, pp.36-37] it is mentioned that $\tau_{AOI} \leq 3$ ns is acceptable.

$$\Delta r_{PR} = (\tau_{AOI} + \tau_{BW})v_p \quad (2.17)$$

2.7.3 Radiation symmetry, phase center and group delay

According to [11], it is generally not possible to provide ideal phase center and group delay responses independent of signal frequency and AOI for practical

wideband and widebeam GNSS antennas. However, the phase and group-delay responses critically depend on the inherent electromagnetic symmetry of the antenna and its feed.

The evidence indicates that an antenna having a geometrically symmetric radiator made of isotropic materials and electrically symmetric feeding, excitation and CP generating network will result in predictable phase center and group delay responses [11]. An example used is a comparison between a single probe-feed (inherently asymmetric), and a 4-point aperture coupled microstrip antenna (inherently symmetric), shows a group delay variation of 3 and 0.5 ns, respectively [11].

2.8 Summary

In this chapter a review and analysis of the GNSS antenna properties and requirements was presented. A GNSS antenna needs to receive RHCP signals covering frequencies from 1164 MHz to 1300 MHz and from 1560 to 1606 MHz. In terms of the other radiation requirements, it was shown that the GNSS antennas have different requirements comparing to the antennas used in point-to-point communications. Specifically, a GNSS antenna needs to provide uniform gain, AR and radiation efficiency performances independent of the signal AOI for $0^\circ \leq \phi \leq 360^\circ$ and $0^\circ \leq \theta \leq (90^\circ - EMA)$. At the same time, an antenna needs to provide a maximum suppression of the signals arriving below *EMA*. Achieving such a uniform and almost 180° broad beamwidth is difficult and it has not been demonstrated in the literature.

In the next chapter results of the literature review covering the state of the art GNSS antennas will be presented. Specifically, the GNSS antennas based on the dielectric resonator, which were found to provide high performance yet in a compact form.

3 Literature review

This chapter presents a literature review of DRA and its applicability to the field of GNSS. The DRA concept was selected based on the results of a broad GNSS antenna survey. The survey found that the microstrip antenna, specifically the stacked multi-layer type, and DRA provide a good basis for an antenna that could meet the thesis objectives. Both of the antenna types can offer either a multi-band or wideband coverage, broad-beam radiation pattern, dual-sense CP and a compact size. However, the DRA was found to have several advantages over the microstrip antenna. Similar findings were also reported in [12].

This chapter consists of 9 sections. A brief overview of the DRA is given in section 3.1, including the DRA concept of operation. Section 3.2 covers the DR, as the key element of a DRA, including basic DR geometries, resonant modes and radiation patterns. This section also includes an overview of DR analysis techniques and application of the image theory. Antenna Q-factor, its relation to BW and coupling factor are covered in section 3.3. Section 3.4 covers the DR excitation techniques and introduces the coupling factor. In section 3.5 techniques for CP generation are covered. Sections 3.6, 3.7, 3.8 and 3.9 cover feeding networks, hybrid DRA (hDRA), finite size ground plane effects and CP DRA state of the art, respectively.

3.1 Dielectric resonator antenna

The subject of DRA is well covered in the literature, however, DRA is not common among the commercial antennas, especially in the GNSS domain. This could be attributed to the facts that the DRA concept is relatively recent and relatively high cost of DRA comparing to other antenna types, especially the printed antennas.

3.1.1 History

The first published research on DR use in the microwave applications was made in 1939 [13], whereas the first antennas were reported in 1983 [14, 15]. Further theoretical and technological developments followed soon after. In 1984 and 1994 analytical methods for cylindrical and rectangular DR were developed, respectively, see *Kajfez et al* in [16] and *Mongia et al* in [17].

Significant contributions were made between 1990 and 1998 in the area of the broadband and CP DRA. A key point appears to be development and demonstration of the contact-less slot coupling for DRA by *Martin et al* [18, 19] in 1990 and 1991, which was further refined by *Antar et al* [20, 21] and *Kishk et al* [22, 23] between 1993 and 1996. The works by the same group of authors in [24, 25, 26] also made notable contributions. Efforts to develop the DRA technology as an alternative to the traditional antennas and further increase DRA performance in a compact and low profile form continue today.

3.1.2 Advantages

A DRA offers inherently wide BW, high radiation efficiency and a high degree of design flexibility relative to the other antenna types [27, 28]. The design flexibility and radiation efficiency are the two key advantages. The design flexibility is due to the additional design variables such as the resonator shape, dimensions and dielectric constant of the DR material. In addition, it is possible to design a multi-mode DR where each mode can operate at its own resonant frequency.

The high radiation efficiency is due to use of low-loss microwave dielectric materials and it regularly exceeds 90% [27, pp.1-2]. For a comparison, the radiation efficiency of the microstrip patch antennas rarely approaches 80% and typically only over 1-3% BW [5, pp.80-81][29].

An additional advantage of DRAs is the controllable size. The DRA size is proportional to $\lambda_0/\sqrt{\epsilon_r}$, where λ_0 is the resonant frequency wavelength, and ϵ_r is the relative permittivity of the dielectric material. Therefore, DR size is inversely proportional to $\sqrt{\epsilon_r}$ and use of the high permittivity materials allows size reduction.

3.1.3 Concept of operation

A DRA is a resonant antenna that consists of three major parts: a DR, excitation mechanism and feeding circuitry. A DR is made of low-loss homogeneous dielectric material, usually ceramic based but use of polyesters and even distilled water has been reported [27, 28]. It radiates by leaking out electromagnetic fields, which decreases Q-factor, which makes the DR an efficient broadband radiator. The DR resonant frequency is a function of its shape, dimensions and the material permittivity ϵ_r .

The excitation mechanism transfers the energy between a DR and transmission line. It primarily impacts the radiation mode, coupling factor and antenna input impedance. There are several DR excitation techniques and they are usually selected based on the overall antenna design requirements.

The feeding circuitry varies in complexity, ranging from a simple transmission line to a network that includes multiple power splitting, phase shifting and impedance matching circuits. Complexity of the feeding circuitry is mostly affected by the number of excitation ports. In case of the CP DRA, which is of the prime interest in this thesis, the CP generation network is a part of the feeding circuitry.

3.2 Dielectric resonator

The resonator is the central part of a DRA. In theory any dielectric shape can be made to radiate, however, due to design and fabrication considerations, it is usually limited to one of the simpler geometrical shapes such as cube, cylinder and hemisphere (Figure 3.1). The key difference between the shapes is the radiation mode support. The resonant frequency and radiation mode of a DR primarily depend on its shape, dimensions and the relative dielectric permittivity ϵ_r . The most common ϵ_r values typically range between 10 and 60. In this section radiation properties of rectangular and cylindrical DR shapes will be reviewed. The hemispherical shape is not considered due to a limited number of design degrees of freedom.

3.2.1 Analysis techniques

There are several methods for DR analysis including the magnetic wall model (MWM), the transmission line model (TLM) and numerical methods such as Method of Moments (MoM) and Finite Elements Method (FEM). The ana-

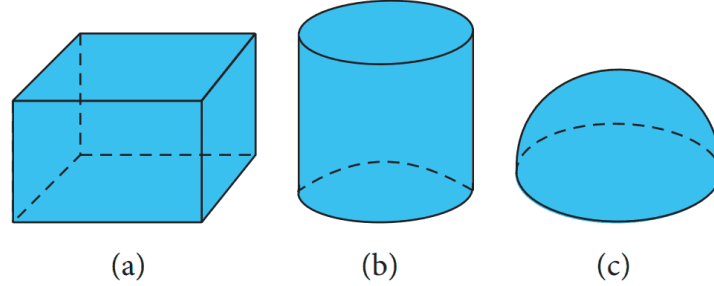


Figure 3.1: Basic dielectric resonator shapes: a) rectangular, b) cylindrical and c) hemispherical.

lytical methods are good for understanding physical insights, however, they are not as accurate as the numerical methods [30].

Kajfez et al in [16] presented a computational procedure and field patterns of the five lowest resonant modes in the cylindrical DR. The procedure is based on a MoM solution of the surface integral equation for bodies of revolution (BOR). An evaluation algorithm for the modal field components is also described.

Mongia et al in [17, 31] presented the dielectric waveguide model (DWM), which was found to be adequate for simple shapes such as rectangular and cylinder. It has a typical resonant frequency error of 5% to 6% and also predicts reasonably accurately the field distribution inside a DR.

Antar et al in [32] introduced a modified dielectric waveguide model (MDWM) to address inaccuracies at for $\epsilon_r \geq 30$. MDWM uses an effective dielectric constant of the material instead of its intrinsic value to reduce the resonant frequency error and improve prediction of the field distribution.

For practical engineering applications, simplified and closed form equations for design of a rectangular, cylindrical and hemispherical DR are given in [28, pp.7-45] and [27, pp.127-172]. Those described design procedures are commonly used in the literature.

3.2.2 Cylindrical DR

A cylindrical DR is described by its dielectric permittivity ϵ_r , radius r and height h (Figure 3.2). A free space suspended cylindrical dielectric resonator can radiate in four modes: transverse electric (TE), transverse magnetic (TM) and two hybrid modes [28, pp.18-22]. The hybrid modes are called HE , where the E_z component of the electric field is dominant and EH , where the H_z component of the magnetic field is dominant.

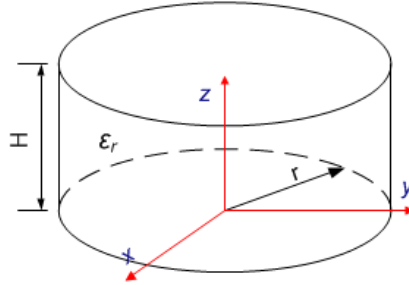


Figure 3.2: Cylindrical DR geometry.

The lower order modes $TE_{01\delta}$, $HE_{11\delta}$ and $TM_{01\delta}$ provide the highest radiation efficiency and they are usually of the primary interest for an antenna design. The subscripts refer to field variations in the azimuth (ϕ), radial (r) and axial (z) directions, respectively, in the cylindrical coordinates. The δ value ranges between zero and one and approaches one for high values of ϵ_r [28, pp.18-19]. The first few resonances have been extensively studied but only $TM_{01\delta}$ and $HE_{11\delta}$ are commonly used for radiation purposes.

The $TE_{01\delta}$ mode has the lowest resonant frequency and a radiation pattern similar to a vertical half-wavelength magnetic dipole [16]. Use of this mode is uncommon for antennas due to its intrinsically high Q-factor and it does not support CP. Hence this mode is of no interest for this work. The $HE_{11\delta}$ mode is the second resonant mode and it provides a broadside radiation pattern that resembles a horizontal half-wavelength dipole. This mode has the lowest Q-factor and for low ϵ_r it is difficult to achieve broadband coupling without additional impedance matching [16]. This is the only mode that supports CP in the cylindrical DR. Figure 3.3.a shows the internal fields of a free space suspended $HE_{11\delta}$ mode resonant DR. The far-field radiation pattern over an infinite ground plane is shown in Figure 3.3.b. The radiation pattern of the $TM_{01\delta}$ mode resembles a vertical half-wavelength dipole radi-

ating omni-directionally in the $x-y$ plane, see Figure 3.4.

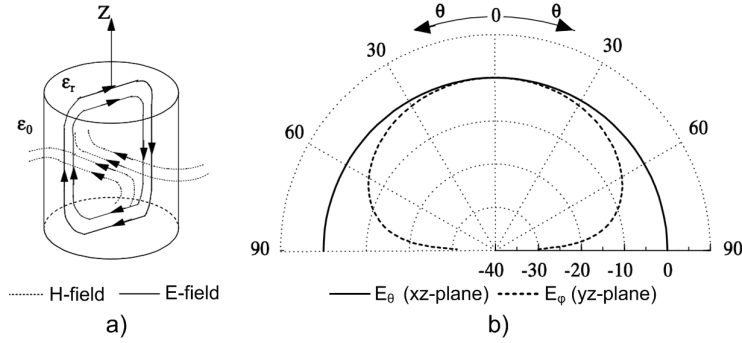


Figure 3.3: Cylindrical DR $HE_{11\delta}$ mode: a) Free space suspended internal fields and b) far-field radiation pattern over an infinite ground plane (from [27]).

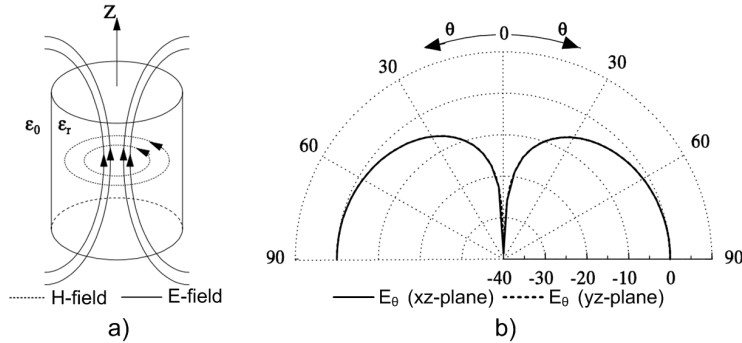


Figure 3.4: Cylindrical DR $TM_{01\delta}$ mode: a) Free space suspended internal fields and b) far-field radiation pattern over an infinite ground plane (from [27]).

3.2.3 Cylindrical DR internal EM fields

There are no exact analytical solutions for the fields within a cylindrical DR. Literature focuses on interpretation of the theoretical models, experimental results and numerical analysis. *Lim* in [30, pp.20-35] summarized derivation process for the $HE_{11\delta}$ mode fields based on MWM.

A proper understanding of the internal fields is necessary for positioning of an exciter within the DR volume. *Petosa* in [28, pp.51-53] provides field equations for the $TM_{01\delta}$ and $HE_{11\delta}$ modes. Eq. 3.1 - 3.6 describe the $TM_{01\delta}$ mode E and H fields as a function of DR radius r and height h in the cylindrical coordinates. The $J_0(\beta r)$ and $J_1(\beta r)$ are the Bessel functions of the first kind and β is a solution to $J_0(\beta r) = 0$ conditions. Figure 3.5 shows a relative field strength based on the eq. 3.1 - 3.6.

$$E_z = 0 \quad (3.1)$$

$$E_r = 0 \quad (3.2)$$

$$E_\phi \propto J_1(\beta r) \cos\left(\frac{\pi}{2h}z\right) \quad (3.3)$$

$$H_z \propto J_0(\beta r) \cos\left(\frac{\pi}{2h}z\right) \quad (3.4)$$

$$H_r \propto J_1(\beta r) \sin\left(\frac{\pi}{2h}z\right) \quad (3.5)$$

$$H_\phi = 0 \quad (3.6)$$

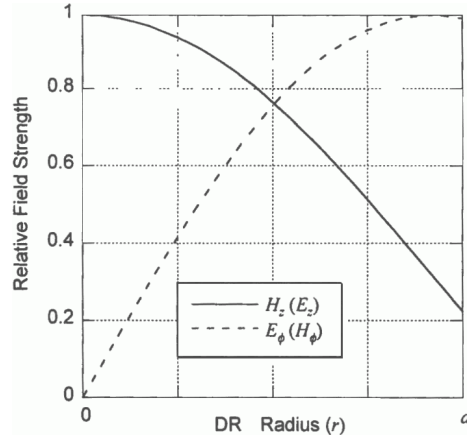


Figure 3.5: Cylindrical DR $TM_{01\delta}$ mode relative field strength (from [28]).

In the same fashion eq. 3.7 - 3.12 describe the $HE_{11\delta}$ mode E and H fields where α is a solution to $J_0(\alpha r) = 0$ conditions. A choice of $\cos(\phi)$ or $\sin(\phi)$

depends on the location of the excitation point in the $x-y$ plane. Figure 3.6 shows a relative field strength based on the eq. 3.7 - 3.12.

$$E_z \propto J_1(\alpha r) \cos\left(\frac{\pi}{2h} z\right) \begin{cases} \cos(\phi) \\ \sin(\phi) \end{cases} \quad (3.7)$$

$$E_r = \frac{\partial J_1(\alpha r)}{\partial(\alpha r)} \sin\left(\frac{\pi}{2h} z\right) \begin{cases} \cos(\phi) \\ \sin(\phi) \end{cases} \quad (3.8)$$

$$E_\phi \propto J_1(\alpha r) \sin\left(\frac{\pi}{2h} z\right) \begin{cases} \sin(\phi) \\ \cos(\phi) \end{cases} \quad (3.9)$$

$$H_z = 0 \quad (3.10)$$

$$H_r \propto J_1(\alpha r) \cos\left(\frac{\pi}{2h} z\right) \begin{cases} \sin(\phi) \\ \cos(\phi) \end{cases} \quad (3.11)$$

$$E_r = \frac{\partial J_1(\alpha r)}{\partial(\alpha r)} \cos\left(\frac{\pi}{2h} z\right) \begin{cases} \cos(\phi) \\ \sin(\phi) \end{cases} \quad (3.12)$$

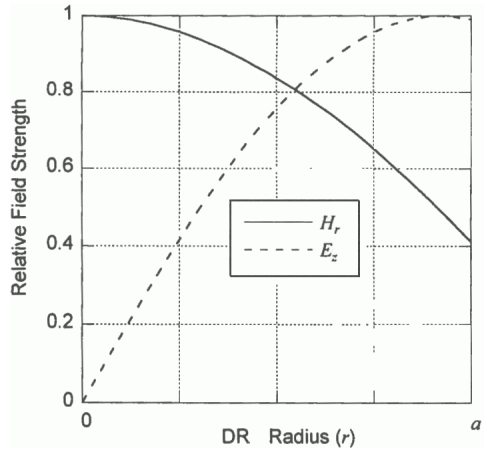


Figure 3.6: Cylindrical DR $HE_{11\delta}$ mode relative field strength (from [28]).

3.2.4 Rectangular DR

A rectangular DR is described by ϵ_r , width W , length L and height H , as shown in Figure 3.7. Thus, it has one more degree of freedom than the cylindrical DR, which makes it the most versatile basic DR shape. As in case of the cylindrical DR, the aspect ratios L/H and W/H are bounded such that $0.2 \leq L/H \leq 3.0$ and $0.5 \leq W/H \leq 4$ [28, pp.29-45].

According to [33, pp.16-26], a rectangular DR can support TE and TM modes, however, existence of the lower-order TM modes has not been experimentally confirmed. Due to the geometry, a rectangular DR offers reduced mode degeneracy, compared to the cylindrical DR, which is desirable in the linear polarization designs. However, the mode degeneracy is necessary for CP and it is achieved through a proper DR excitation.

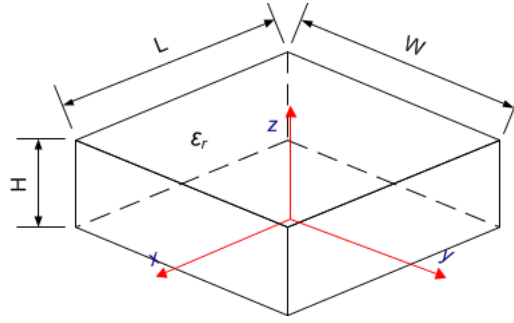


Figure 3.7: Rectangular DR geometry.

The TE mode radiates like a short magnetic dipole (Figure 3.8.b). For a DR where $W > L > H$, the lowest order mode is $TE_{\delta 11}^x$. The superscript indicates the dominant mode direction. Also, the resonant frequencies in the x , y and z directions will be $f_x < f_y < f_z$.

3.2.5 Rectangular DR internal EM fields

Petosa in [28, pp.51-53] provides a procedure for analysis and derivation of the fields within a rectangular DR for the $TE_{\delta 11}^x$ mode. The analysis is based on the DWM [17, 31]. Proper understanding of the DR internal fields is necessary for the excitation mechanism design as in the case of cylindrical DR. For a DR where $W > L > H$, the $TE_{\delta 11}^x$ mode E and H fields are given by eq. 3.13 - 3.18.

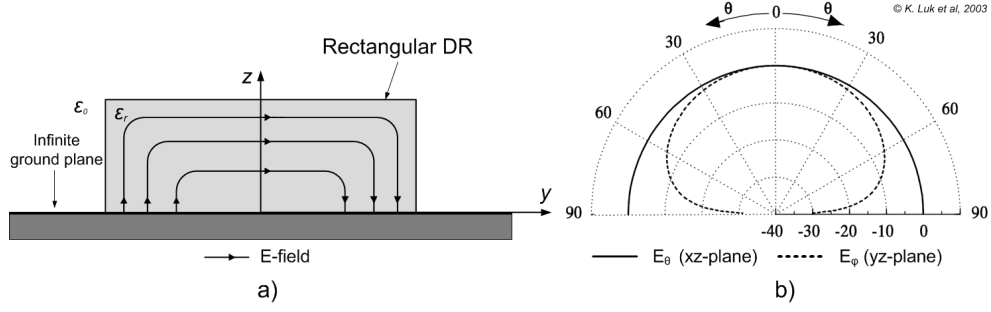


Figure 3.8: Rectangular DR $TE_{\delta 11}$ mode: a) Internal E -field and b) far-field radiation pattern.

$$E_x = 0 \quad (3.13)$$

$$E_y = k_z \cos(k_x x) \cos(k_y y) \sin(k_z z) \quad (3.14)$$

$$E_z = -k_y \cos(k_x x) \cos(k_y y) \cos(k_z z) \quad (3.15)$$

$$H_x = \frac{(k_y^2 + k_z^2)}{j\omega\mu_0} \cos(k_x x) \cos(k_y y) \cos(k_z z) \quad (3.16)$$

$$H_y = \frac{(k_x k_y)}{j\omega\mu_0} \sin(k_x x) \sin(k_y y) \cos(k_z z) \quad (3.17)$$

$$H_z = \frac{(k_x k_x)}{j\omega\mu_0} \sin(k_x x) \cos(k_y y) \sin(k_z z) \quad (3.18)$$

A solution of the eq. 3.13 - 3.18 depends on the wavenumber k in x , y and z axis directions, respectively. The k_y and k_z are simple ratios of the DR width (W) (eq. 3.19) and height (H) (eq. 3.20). To find k_x , a transcendental eq. 3.21 and eq. 3.22 need to be solved for a given resonant frequency f_r and the free space wavenumber k_0 (eq. 3.23).

$$k_y = \frac{\pi}{W} \quad (3.19)$$

$$k_z = \frac{\pi}{H} \quad (3.20)$$

$$k_x \tan(k_x \frac{L}{2}) = \sqrt{(\varepsilon_r - 1)k_0^2 - k_x^2} \quad (3.21)$$

$$k_x^2 + k_y^2 + k_z^2 = \varepsilon_r k_0^2 \quad (3.22)$$

$$k_0 = \frac{2\pi f_r}{c} \quad (3.23)$$

The outlined procedure and eq. 3.13 - 3.23, describe magnitudes of E and H fields as a function of a position within the rectangular DR volume. Figure 3.9 shows the relative field strength as a function of DR width for $TE_{\delta 11}^x$ mode. *Petosa* [28, pp.29-45] provides additional information for an iterative solution of the transcendental eq. 3.21. For the fields within a rectangular DR, *Antar and Fan* [20, 21], *Mongia* [31] and *Fang* [34] provide further insights.

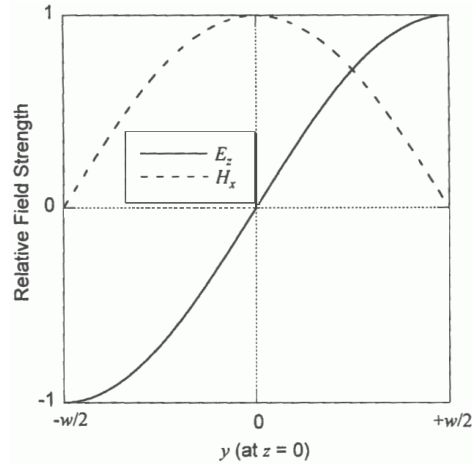


Figure 3.9: Rectangular DR $TE_{\delta 11}^x$ mode relative field strength (from [28]).

Based on [28, pp.33] eq. 3.24 is used to estimate the radiation Q-factor (Q_{rad}), where P_{rad} , stored energy W_e and resonant frequency ω_0 . The same equation is also provided in [27, pp.64] and [31], however, it does not agree with *Pozar* [35, pp.274]. Eq. 3.25 and 3.26 give W_e and P_{rad} , respectively, where A is an arbitrary constant based on the field maximum amplitude, \vec{p}_m is the magnetic dipole moment and $\omega = 2\pi f_0$. Based on [36, pp.23-24], the difference

between measured and calculated resonant frequencies for a rectangular DR ranges between 3% and 12%, while Q-factor errors can approach 100%.

$$Q_{rad} = 2 \frac{\omega_0 W_e}{P_{rad}} \quad (3.24)$$

$$W_e = \frac{\epsilon_0 \epsilon_r L W H A^2}{32} \left(1 + \frac{\sin(k_x L)}{k_x L} \right) (k_y^2 + k_z^2) \quad (3.25)$$

$$P_{rad} = 10 k_0^4 |\vec{p}_m|^2 \quad (3.26)$$

$$\vec{p}_m = \frac{-j\omega 8\epsilon_0(\epsilon_r - 1)A}{k_x k_y k_z} \sin\left(k_x \frac{L}{2}\right) \quad (3.27)$$

3.2.6 DR and application of the image theory

When there is an E -field symmetry within a free-space suspended DR, the image theory can be applied [27, pp.127-172]. The image theory implies use of a perfect electric conductor (PEC) of an infinite size in the E -field plane of symmetry (Figure 3.10). It can be seen in Figure 3.3.a and 3.4.a that $HE_{11\delta}$ and $TM_{01\delta}$ modes have an E -field symmetry at the cylinder mid point. Hence, the plane of symmetry is perpendicular z -axis and cuts the cylinder in two equal parts. Each of two DR halves retains identical field distributions and the resonant frequency of a free-space suspended DR [27, pp.128 and 146-148].

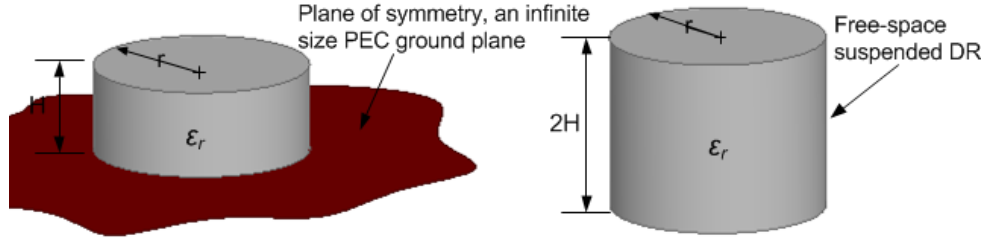


Figure 3.10: Cylindrical DR and image theory.

In case of the GNSS antennas, application of the image theory has a two fold impact: the first is that it allows the DR height reduction by half and second, it places a DR into a typical exploitation environment since GNSS antennas are typically used over a ground plane. However, a practical ground

plane is not of an infinite size. The effects of a finite size ground plane are covered in section 3.8.

3.3 Quality factor and coupling coefficient

3.3.1 Quality factor Q

The Q-factor is directly related to the bandwidth and it is used as a figure of merit to assess DR performances. There are four Q-factors that are defined in the DR context: Unloaded Q-factor (Q_u), external (Q_{ext}), loaded (Q_L) and the radiation (Q_{rad}). The unloaded Q-factor Q_u represents a free space suspended DR that is freely oscillating without an external source. It is defined by eq. 3.28 [35, pp.274] where ω_0 is the resonant frequency, W_e is the stored energy and P is the total dissipated power. In an equivalent RLC circuit the L and R are the resonator internal inductance and resistance.

$$Q_u = \frac{\omega_0 W_e}{P} = \frac{\omega_0 L}{R} \quad (3.28)$$

The total dissipated power P is given by eq. 3.29, where P_{rad} , P_d and P_c are radiated power, dielectric and conductor power loss, respectively. However, DRA have significantly smaller P_d and P_c compared to P_{rad} due to inherent high radiation efficiency, hence, $Q_u \approx Q_{rad}$ (eq. 3.30).

$$P = P_{rad} + P_d + P_c \quad (3.29)$$

$$Q_{rad} = \frac{\omega_0 W_e}{P_{rad}} \approx Q_u \quad (3.30)$$

When a DR is connected to an external energy source through an excitation mechanism an appropriate Q-factor is Q_L , which is the Q-factor seen from the transmission line connected to the excitation mechanism. Q_L is given by eq. 3.31 where Q_{ext} is the external Q-factor given by eq. 3.32. If the transmission line impedance $Z_0 = R_L$, i.e. the transmission line is the only loading, and $Z_0 = R$, the resonator internal resistance, then $Q_u = Q_{ext}$. Thus, at the resonant frequency the DR is matched to the transmission line impedance and $Q_L = Q_u/2$.

$$\frac{1}{Q_L} = \frac{1}{Q_{ext}} + \frac{1}{Q_u} \quad (3.31)$$

$$Q_{ext} = \frac{\omega_0 L}{R_L} \quad (3.32)$$

3.3. Quality factor and coupling coefficient

In [37] it is shown that the Q_{rad} is proportional to ε_r (eq. 3.33) for DRs of $\varepsilon_r > 100$. For $\varepsilon_r < 100$ eq. 3.33 is still valid, however, with adjusted P values. In [17] the P values for the lower order modes of the cylindrical DR are given in Table 3.1. The same reference also states that the P values are nearly independent of the cylindrical DR r/h aspect ratio.

$$Q_{rad} \propto \varepsilon_r^P \quad (3.33)$$

Where

- $P = 1.5$ for modes radiating like a magnetic dipole ($TE_{01\delta}$ and $HE_{11\delta}$)
- $P = 2.5$ for modes radiating like an electric dipole ($TM_{01\delta}$)
- $P = 2.5$ for modes radiating like a magnetic quadrupole ($HE_{21\delta}$)

Table 3.1: Cylindrical DR P values for lower order modes (from [17]).

Mode	P
$TE_{01\delta}$	1.27
$HE_{11\delta}$	1.30
$HE_{21\delta}$	2.49
$EH_{11\delta}$	2.71

3.3.2 BW and Q -factor

The DR impedance BW is defined as a frequency range in which the input voltage standing wave ratio ($VSWR$) is less than the specified. The Q_{rad} , or Q_u as shown in section 3.3.1, and BW are related through eq. 3.34 [28, pp.11], where BW_{abs} is the absolute BW and f_0 is DR resonant frequency. It is not clear how is in this case RL related to Q_u considering that RL or $VSWR$ would be measured externally to a DR, hence use of Q_L would be intuitive.

$$BW = \frac{BW_{abs}}{f_0} = \frac{VSWR - 1}{\sqrt{VSWR} Q_{rad}} \quad (3.34)$$

3.3.3 Coupling coefficient χ

For an efficient coupling between a DR and transmission line, an exciter aperture has to create an equivalent current to the DR field at the point of excitation. The excitation current can be electrical or magnetic, depending on the source. Obviously, a magnetic source would couple to the H field whereas an electric source would couple to the E field. For the most effective coupling,

an exciter needs to be located at a point of the maximum field strength [28]. Therefore, a physical insight into the DR fields is essential for understanding DR excitation, which is covered in sections 3.2.3 and 3.2.5.

The coupling coefficient χ is a normalized value determined by using Lorentz Reciprocity Theorem, eq. 3.35 [28, pp.49-51]. It is also further covered in [33, pp.19-20] and [36, pp.26-27]. Eq. 3.35 states that χ is proportional to a dot product between a source of electric current \vec{J}_S or magnetic current \vec{M}_S and the electric fields \vec{E}_{DR} or magnetic fields \vec{H}_{DR} , respectively, inside a DR. The equation implies integration over the entire DR volume V .

$$\chi \propto \int_V \left(\vec{E}_{DR} \cdot \vec{J}_S \right) dV \propto \int_V \left(\vec{H}_{DR} \cdot \vec{M}_S \right) dV \quad (3.35)$$

For a maximum power transfer between a coupling port and DR, which is always desired in the antenna case, the coupling factor needs to be unity or $\chi = 1$. This is also called critical coupling. However, in practical applications an exciter aperture cannot conform entirely to the DR fields, hence, $\chi < 1$, which is obviously always undesired. Over-coupling ($\chi > 1$) is also possible and it reduces antenna radiation efficiency [28, pp.49-51].

Eq. 3.36 [28] introduces Q_{ext} as Q_u corrected for the coupling coefficient χ . Based on eq. 3.36 low coupling coefficient increases antenna Q_{ext} , which decreases the impedance BW. A coupling mechanism has a loading effect on a DR as shown in eq. 3.37 [28, pp.50-51]. In essence eq. 3.37 tells that a perfect coupling mechanism producing $\chi = 1$ will half antenna Q_L . This also implies, although not explained in such terms, that a DRA input Q_L , which is based on RL, does not represent the antenna actual Q_{rad} or Q_u .

$$Q_{ext} = \frac{Q_u}{\chi} \quad (3.36)$$

$$Q_L = \frac{Q_u}{1 + \chi} \quad (3.37)$$

3.4 Dielectric resonator excitation

This section provides an overview of the common DR excitation techniques. The DR excitation or coupling is a process of energy transfer between a DR and transmission line. Literature mentions several excitation mechanisms: slot aperture, coaxial probe, microstrip line, coplanar waveguide, conformal

strip line and substrate-integrated waveguide (SIW). The coupling method and location of the excitation point will significantly affect DR radiation performances including the resonant frequency, impedance BW, radiation efficiency, gain and polarization.

3.4.1 Slot aperture

The aperture coupling involves a slot in the ground plane beneath the DR that is usually fed by a microstrip line, Figure 3.11 and 3.12.a. It is considered contact-less as there is no electrical contact between a transmission line and DR. A slot is equivalent to a horizontal magnetic dipole and it should be placed at a location of the maximum magnetic field intensity of a desired mode.

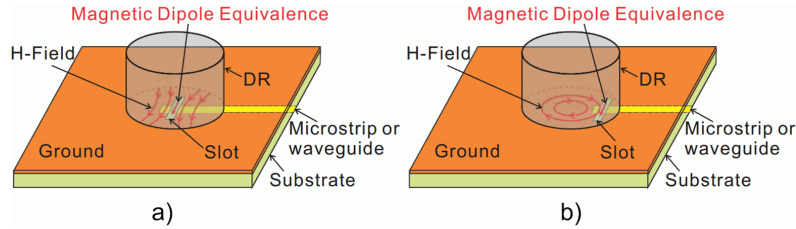


Figure 3.11: Cylindrical DR slot excitation: a) $HE_{11\delta}$ mode and b) $TM_{01\delta}$ mode (from [33]).

To excite the $HE_{11\delta}$ mode in a cylindrical DR, a slot needs to be located at the center of a cylinder, whereas for the $TM_{01\delta}$ mode, a slot needs to be near the periphery (Figure 3.11). To excite the TE mode in a rectangular DR (Figure 3.12.a), a slot also needs to be located at the center of a rectangle. In both cases slot's orientation relative to the DR will determine the radiating mode orientation.

The shape and number of the slots can be optimized to improve the DRA performance and BW. Figure 3.13 shows some of the common slot shapes. Figure 3.14 shows 4-port arc shaped slots used for a cylindrical DR. The apertures are fed by a microstrip lines where the open-end line length is used for impedance matching.

A guideline for a rectangular aperture sizing is given in [28, pp.55-66]. Eq. 3.38 and 3.39 give aperture length l_A and width w_A , respectively, see Figure 3.15. A portion of a microstrip line extending past the aperture can be used for impedance matching as in Figure 3.14. Eq. 3.40 gives the length s of

a microstrip line extending past the aperture. In [28, pp.55-66] it is suggested that eq. 3.40 is only a good starting value and that the s needs to be optimized.

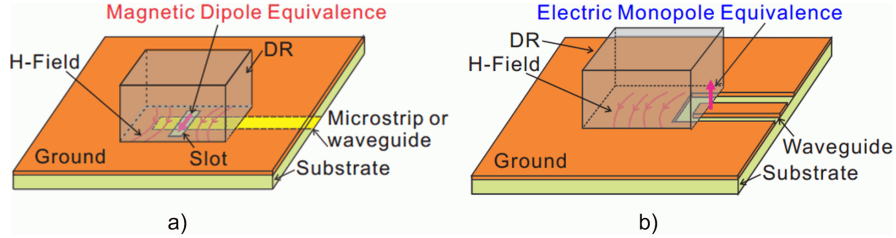


Figure 3.12: Rectangular DR $TE_{11\delta}$ mode excitation: a) Slot aperture and b) Coplanar waveguide (from [33]).

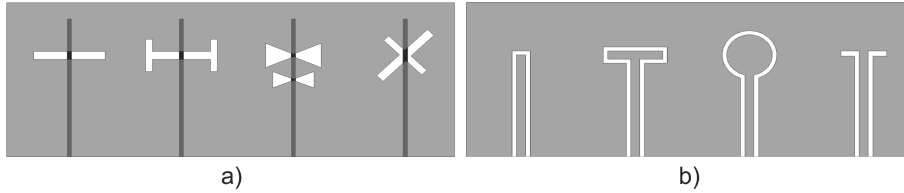


Figure 3.13: Various shapes of a) slot aperture and b) co-planar waveguide.

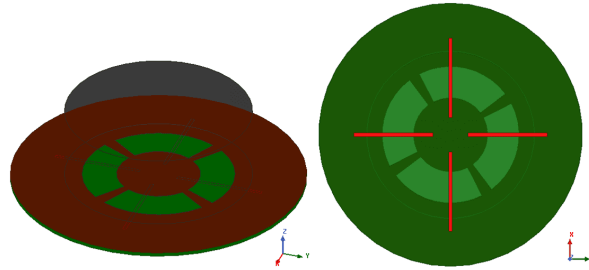


Figure 3.14: Cylindrical DR 4-port arc-slot aperture coupling.

$$l_A = \frac{0.4\lambda_0}{\sqrt{\epsilon_{eq}}} \quad (3.38)$$

$$w_A = 0.2l_A \quad (3.39)$$

$$s = \lambda_g/4 \quad (3.40)$$

In eq. 3.38 λ_0 is the free-space wavelength, ε_{eq} is equivalent dielectric permittivity based on the relative dielectric permittivity of DR $\varepsilon_{r_{DR}}$ and the substrate ε_{r_S} , respectively, see eq. 3.41. In eq. 3.40 λ_g is a guided wavelength of the microstrip line, see [35, pp.147-149]. In [23] a more accurate approach is given based on experimentally verified results for a cylindrical DR $HE_{11\delta}$ mode excitation.

$$\varepsilon_{eq} = \frac{\varepsilon_{r_{DR}} + \varepsilon_{r_S}}{2} \quad (3.41)$$

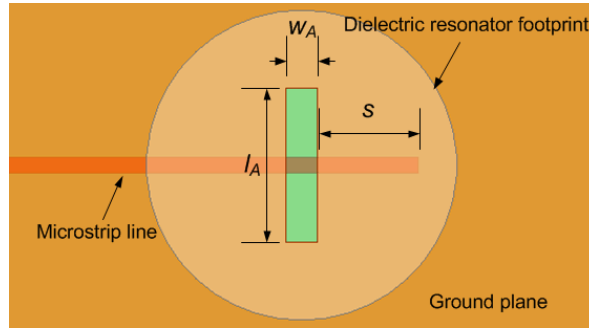


Figure 3.15: Rectangular slot in the ground plane.

The aperture coupling has an advantage of having the excitation mechanism beneath the ground plane, which isolates the DR from its feed network. In addition, the size, shape and position of the aperture can be used as additional parameters to further optimize coupling. In [33, pp.22-23] several such concepts are described. Three most interesting examples include use of an H-shaped slot to reduce the back-lobe radiation around a DR resonance, use of two parallel bow-tie slots to increase DRA impedance BW and use of an asymmetric cross-slot to achieve CP using one feed (Figure 3.13).

Based on eq. 3.38, the aperture size is proportional to the free-space wavelength λ_0 and inversely proportional to $\sqrt{\varepsilon_{eq}}$. This indicates that a DR designed for lower frequencies and made of a low ε_r material could require a size of an aperture that is larger than a DR footprint on the ground plane. In addition, a large aperture could also resonate within the DR resonant band, which would result in an undesired back-lobe radiation.

3.4.2 Coaxial probe

A coaxial probe is the simplest technique to excite the $TE_{\delta 11}$ mode in a rectangular DR or the $HE_{11\delta}$ mode in a cylindrical DR. A probe acts like a short electric monopole and to achieve an optimum coupling it needs to be placed at a location of the maximum electric field intensity, as shown in figures 3.16 and 3.17a. The points of the maximum electric field intensity for $TE_{\delta 11}$ and $HE_{11\delta}$ modes are located at the periphery of a cylindrical and rectangular DR, respectively. Hence, a probe can be used without any modifications to a DR.

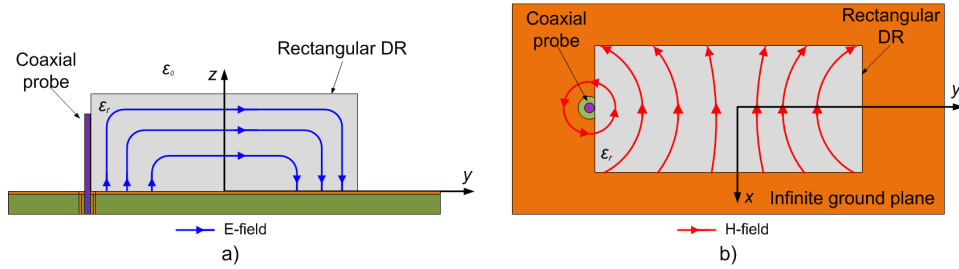


Figure 3.16: $TE_{\delta 11}$ mode coaxial probe excited rectangular DR: a) E -field distribution and b) H -field distribution.

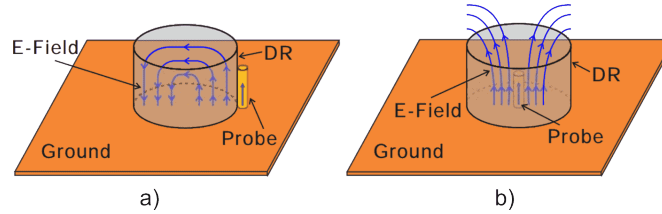


Figure 3.17: Cylindrical DR coaxial probe excitation: a) $HE_{11\delta}$ mode excitation and b) $TM_{01\delta}$ mode excitation (from [33]).

In case of the TM mode excitation in a cylindrical DR, the probe needs to be located inside the resonator, as shown in Figure 3.17.b. However, that changes the effective dielectric constant of the material, hence, affecting the resonant frequency and the Q -factor. In addition, DR drilling increases manufacturing costs of the antenna.

To improve the antenna impedance matching, the probe height can be optimized. To avoid parasitic radiation from the probe, its length is usually less

than the DR height [28]. Use of the probe radius as an impedance matching parameter is not mentioned. A variation of the probe concept is a flat or conformal metallic strip on the DR side wall. That provides an additional variable for impedance matching, which is the strip width. Figure 3.18 shows conformal strips used on a cylindrical DR.

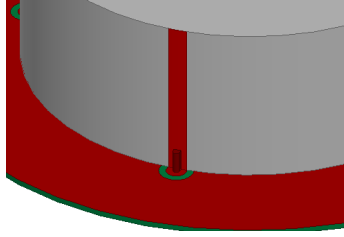


Figure 3.18: Cylindrical DR using conformal strip line coupling.

3.4.3 Microstrip line

The microstrip line coupling is usually used for planar feed networks or where the space required for the feed network is limited. It is a simple excitation technique as a microstrip line does not have to be inside or under a DR. The microstrip line is usually used to excite the $HE_{11\delta}$ and $TE_{11\delta}$ modes in a cylindrical and rectangular DR, respectively. Since an open-ended microstrip line acts in this case as an electric monopole, the feeding point can be beside or underneath but close to a DR edge, as shown in Figure 3.19.

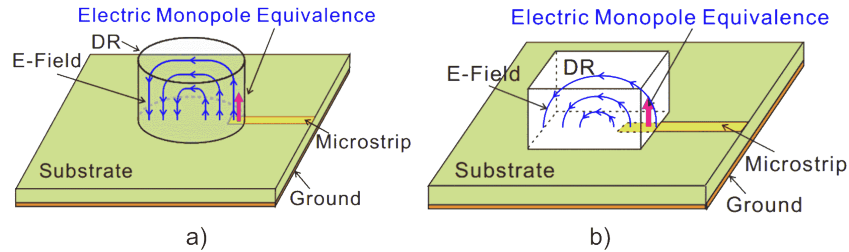


Figure 3.19: Microstrip line coupling: a) Cylindrical DR $HE_{11\delta}$ mode and b) Rectangular DR $TE_{11\delta}$ mode (from [33]).

High efficiency and wideband coupling can be achieved when the shape and length of an open ended stub are optimised [38]. To further improve coupling, different patch like shapes for the open-end have been proposed in the

literature, including a trapezoidal and elliptical [39, 40]. Impedance matching can be improved by adjusting DR's position relative to the microstrip point of radiation, however, it may increase cross-polarization or decrease the radiation pattern symmetry. Disadvantages of a top-side microstrip feed network are unwanted coupling to the exposed microstrip lines and susceptibility to the surface wave coupling.

3.4.4 Co-Planar waveguide

An shorted coplanar waveguide (CPW) provides an electric monopole equivalence, which is similar to a coaxial probe, as shown in Figure 3.20 and 3.12.b. However, compared to the coaxial probe excitation, the CPW has advantages of fabrication simplicity and easy integration on the substrate. As a planar feed network, it has the same advantages as the microstrip line coupling in terms of the space occupied by the feed network.

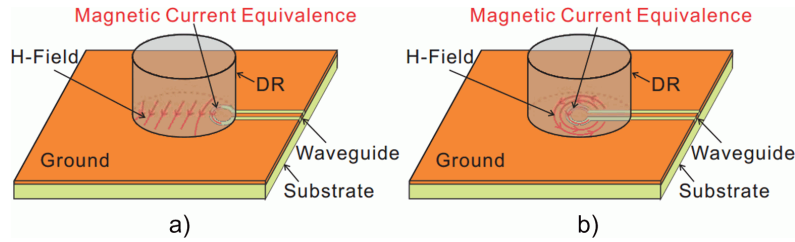


Figure 3.20: Coplanar waveguide coupling to a cylindrical DR: a) $HE_{11\delta}$ mode and b) or $TM_{01\delta}$ mode (from [33]).

An equivalent electric monopole created by a shorted CPW allows it to be placed underneath a DR without drilling a hole, which reduces the DR fabrication costs comparing to the coaxial probe. CPW provides an alternative method to excite the $HE_{11\delta}$ or $TM_{01\delta}$ modes with an advantage of being non-obtrusive. As shown in Figure 3.20, the $HE_{11\delta}$ mode excitation can be achieved by placing a shorted CPW at the edge or in the center to excite $TM_{01\delta}$ mode of a dielectric cylinder. Figure 3.13.b shows some CPW examples including a shorted-circuit, coplanar loops and stub-loaded lines [28, pp.77-78].

3.5 Circular polarisation

In section 2.6 fundamentals of CP and AR were covered whereas the subject of CP DRA is covered in-depth in [28, pp.171-193]. To generate CP radiation,

two sets of fields equal in amplitude ($E_x = E_y$) but 90° out-of phase (i.e. geometrically orthogonal) need to co-exist within a DR. In practice, amplitude equality and phase orthogonality are usually achieved only over a narrow BW. Hence, the far-field polarisation is usually elliptical, as shown in Figure 2.5. AR indicates the polarisation ellipticity and for the GNSS antennas it is expressed as a function of θ and ϕ , see eq. 2.6. The tilt angle of the polarisation ellipse major axis is given by eq. 2.7.

Eq. 3.42 gives AR as a function of the electric field magnitudes in x and y direction, E_x and E_y , respectively, and the phase error angle ψ given in eq. 3.43 [28]. From eq. 3.42 it is obvious that $AR = 0 \text{ dB}$, or perfect CP, can be achieved only when both $E_x = E_y$ and $\psi = 0$. Figure 3.21 shows the effects of the amplitude and phase errors on AR. In addition, in case of the GNSS antennas, the AR varies also with the angle of incidence, as emphasized in section 2.6.

$$AR = 10 \log \left[\frac{E_x^2 + E_y^2 + \sqrt{E_x^4 + E_y^4 + 2E_x^2 E_y^2 \cos(\psi)}}{E_x^2 + E_y^2 - \sqrt{E_x^4 + E_y^4 + 2E_x^2 E_y^2 \cos(\psi)}} \right] \quad (3.42)$$

$$\psi = 2(\phi_x - \phi_y) \quad (3.43)$$

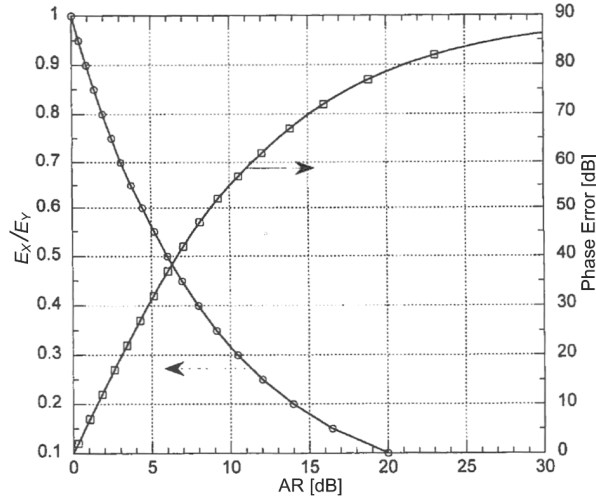


Figure 3.21: Effects of amplitude and phase errors on AR (from [28]).

The far-field CP radiation from a DR can be excited using one or multiple excitation ports. Antennas using single-port excitation typically provide a narrow AR BW and beamwidth and as such are not considered for this work. In addition, the single-port excitation can provide only uni-sense CP. However, single-port CP excitation usually provides a more compact and simpler design. A review is given in Appendix B.

3.5.1 Multi-port excitation

Use of the multiple feeds to excite multiple geometrically orthogonal modes is an intuitive approach to the CP excitation. Typically 2 or 4 excitation ports are used. This requires a DR shape that exhibits symmetry around two axis such as a rectangular DR where $L = W$ or a cylindrical DR. In this case all excited modes will have the same resonant frequency and Q-factor. However, such design requires and relies entirely on a feed network to generate equal amplitude and phase quadrature between the feeding points, which adds to the antenna size and complexity.

In [41] a CP cylindrical DRA excited using dual conformal strips is presented. The antenna provides impedance BW of 13.7% and a 3 dB AR BW of 20%. A similar concept but using four conformal strips is presented in [42]. The strips are placed in a 90° interval around the cylinder circumference and fed in a phase quadrature, see Figure 3.22. The design exhibits 34.5% impedance and 25.9% 3 dB AR BW, respectively. The feeding circuit consists of a pair of 90° hybrid couplers and a T-junction splitter as a power divider. The 180° phase shifting between the couplers is accomplished by adjusting the lengths of the microstrip branches after the T-junction splitter.

Massie et al in [43] reported a 4-port excited CP hybrid DRA showing impedance matching ($S_{11} < -10$ dB) from 1.09 to 1.83 GHz or 50% BW. The $AR < 1$ dB at boresight is achieved from 1.13 to 1.63 GHz, which is antenna's targeted band. The $AR \leq 3$ dB beamwidth ranges between 130° and 190° . The antenna is based on a rectangular resonator excited through 4 slots in the ground plane, see Figure 3.23. Multiple variations of a 4-port excited aperture coupled DRA designs based on a cylindrical DR with similar performance results are also reported in [43, 12, 44, 45, 46]. In case of [46], an $AR \leq 3$ dB beamwidth exceeding 180° had been demonstrated.

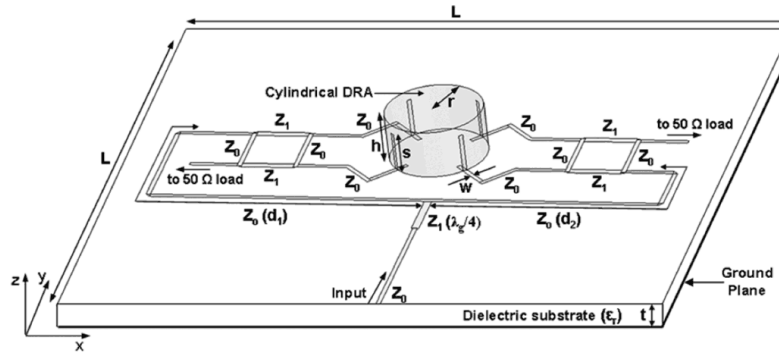


Figure 3.22: CP cylindrical DRA using 4-port conformal strip excitation with a feed network (from [42]).

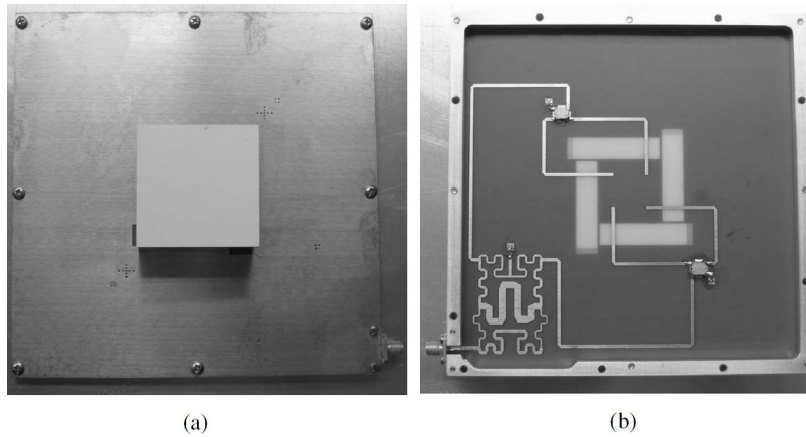


Figure 3.23: 4-port aperture coupled CP hybrid DRA: a) top view and b) underside view feeding circuit. (from [43]).

3.5.2 Multi-port excitation and mutual coupling

Mutual-coupling between the excitation ports can significantly degrade the AR performance [28, pp.174-178]. In a case of -10 dB coupling between two excitation ports, the AR upper limit is 3 dB whereas -20 dB would set it at 0.5 dB. Hence, eq. 3.42 is considered valid only when mutual-coupling is negligible. Eq. 3.44 provides the upper bound of the AR in presence of mutual-coupling [28]. The reflection coefficient Γ_0 is given in eq. 3.45 where s_{ij} are

the s-parameters of a dual-port fed DRA.

$$AR = 10 \log \left(\frac{1 + |\Gamma_0|}{1 - |\Gamma_0|} \right) \quad (3.44)$$

$$\Gamma_0 = \frac{1 - s_{11}^2 + s_{12}^2}{2s_{12}^2} \quad (3.45)$$

The electric field perturbation inside a DR due to the mutual coupling is given in eq. 3.46 [28], where ϕ is the phase difference between E_x and E_y , which is $\phi = \pi/2$ in case of the geometrically orthogonal fields.

$$E_y = E_x e^{-j3\phi} \frac{1 - \Gamma_0 e^{j\phi}}{1 - \Gamma_0 e^{-j\phi}} \quad (3.46)$$

Figure 3.24 shows the AR performance as a function of the mutual coupling between two excitation ports. The impact is also affected by the port impedance matching or the S_{11} -parameter, as shown in eq. 3.45. Obviously, the AR degrades as mutual coupling increases and it is further compounded by the impedance mismatch, especially when $S_{11} > -10 \text{ dB}$. Figure 3.24 also shows that the input impedance match has less impact on the AR performance comparing to the mutual coupling. Hence, a design of a multi-port excited CP DRA needs to be focused on minimizing the mutual coupling to achieve a good AR performance.

3.6 Feeding network

It was shown in section 3.5 that the multi-port excitation provides significantly wider AR beamwidth and BW comparing to the single-port excitation. However, the multi-port excitation requires use of a feed network to generate equal amplitude and a phase quadrature, which adds to the size and complexity.

In case of a two-port excitation, as in [41], the phase difference between the ports needs to be 90° and the input signal needs to be split once. For the four-port excitation, as in the cases of [42, 43, 44], the relative phases shift needs to be 0° , 90° , 180° and 270° for ports 1 to 4, respectively. The input signal in this case needs to be split into four equal parts. The sign of the phase shift depends to the polarisation sense in both cases.

This is typically achieved using a power-divider circuit, such as a hybrid coupler, Wilkinson or a T-splitter [28]. A hybrid coupler also provides a

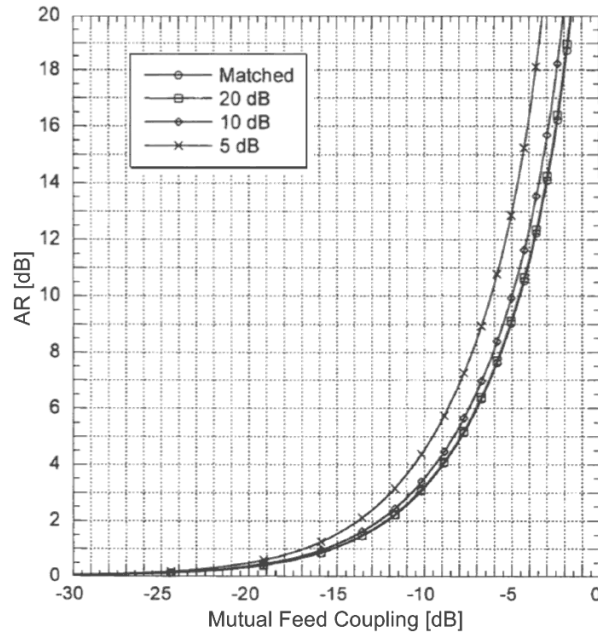


Figure 3.24: AR vs. mutual coupling between excitation ports (from [28]).

90° phase shift whereas in case of the Wilkinson and T-splitter power dividers, the phase delays need to be addressed in addition. The simplest approach is to adjust the lengths of the microstrip branches after the power splitting as in [42], see Figure 3.22. However, use of the physical length of a transmission line can significantly add to the circuit size and increases the feed-line coupling.

In terms of the circuit size, a 4-port excitation network is more than twice the size of a 2-port network. For a 2-port network, only one power divider and phase shifting device is required whereas in case of a 4-port network three such devices are required as shown in the examples of [42, 43]. Figure 3.25 shows a feeding circuit layout of a 4-port CP DRA excited through aperture slots [43]. The first power splitter is a hybrid coupler that provides a 180° phase shift between the two branches. The other two are 90° hybrid couplers designed as the surface mount (SMT) components specifically to minimize the foot-print of the circuit.

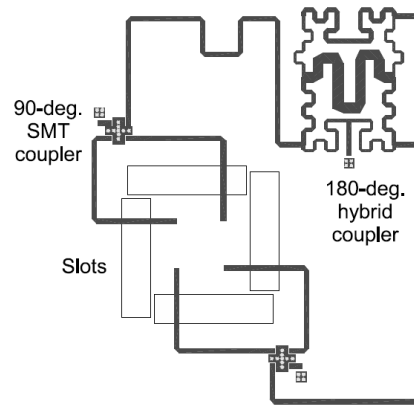


Figure 3.25: 4-port slot excited CP DRA feeding circuit layout (from [43]).

3.7 Hybrid DRA

The term "hybrid DRA" (hDRA) indicates a concept that combines a DR resonance with additional resonances induced either by the antenna excitation mechanism, DR boundary conditions or another coupled resonator. The added resonances contribute to the antenna BW.

Examples of hDRA are antennas reported by *Massie et al.* in [43] and *Caillet et al.* in [45]. These antennas use an additional resonance created by the aperture slots and a meandered slot ring. Another example is the antenna in [42], which uses four conformal strips around the cylinder circumference, see section 3.5.1. The boundary conditions created by the metallic strips induce an additional resonance above the DR primary resonance.

Lapierre et al. in [47] provides probably the best example of a hybrid DRA. The antenna is based on an annular DR and a short electric monopole. It combines resonances of the DR and electric monopole to provide an ultra wideband response exceeding 3:1 of -10 dB impedance BW. Although, this antenna is linearly polarized it could be considered in a multi-element configuration for this work.

Literature in general does not provide analytical tools for hDRA design aside from the empirical results and observations. An exception is *Caillet et al.* [45] where a meandered annular slot ring used to improve a DRA performance is designed based on a microstrip-line-fed circularly polarized printed ring slot

antenna. The slot ring is based on eq. 3.47 and it was demonstrated that the ring increased BW as a result of an added resonance. The ring also improved the far-field AR BW and beamwidth.

$$f_r = \frac{c}{\pi(R_1 + R_2)} \sqrt{\frac{1 + \epsilon_r}{2\epsilon_r}} \quad (3.47)$$

3.8 Finite size ground plane

Application of the image theory, as covered in section 3.2.6, assumes an infinite size perfectly conductive ground plane. However, in practice that is never the case. In [27, 28] it is emphasized that a finite size ground plane has a significant impact on nearly all the DRA radiation parameters. Thus, a ground plane of finite dimensions and its impact on a DRA performance needs to be considered.

It was found that a smaller ground plane will distort the far-field radiation pattern, increase back-lobe radiation, decrease the directional gain, increase impedance BW and shift the resonance frequency [28, pp.164-167]. The direction of the resonance frequency shift is mode dependent. The effects are larger if a ground plane measures less than half of the free-space radiated wavelength. This problem is also covered in [27, 30, 48].

Lim in [30] investigated effects of the circular ground plane size on an $HE_{\delta_{11}}$ mode resonant cylindrical DR. It was found that the ground plane size increase reduces AR beamwidth and increases antenna directive gain. In case of a ground plane diameter exceeding two free-space radiated wavelengths, $AR \leq 3dB$ is available only near the antenna zenith. In addition, it was found that the input impedance traces a sinusoidal pattern as a function of the ground plane size.

3.9 State of the art

The reviewed literature indicates that 4-port excited CP DRAs using a hybrid concept of aperture slot coupling in a combination with a meandered slot ring exceeds in performance all other CP DRA designs. A summary of CP DRA designs provided in [49] shows that only single element CP DRA using 2 and 4-port excitation provide impedance BW exceeding 20%. Similar findings are

also reported in [50].

A 4-port aperture coupled DRA reported by *Massie et al.* in [43, 12] show an overall CP performance of over 33% of antenna's BW. The impedance BW in [43] exceeds the GNSS antenna requirements while the AR at the boresight is under 1 dB over the entire band. The $AR \leq 3\text{ dB}$ beamwidth ranges from 80° to 120° . The realised gain $G_R \geq 0\text{ dBic}$ exceeds the impedance BW, however, the $G_R \geq 0\text{ dBic}$ beamwidth ranges from about 60° to 100° at frequencies near 1.175 GHz and 1.6 GHz, respectively. Figure 3.26 shows the experimental results of RL and AR measured at antenna's boresight.

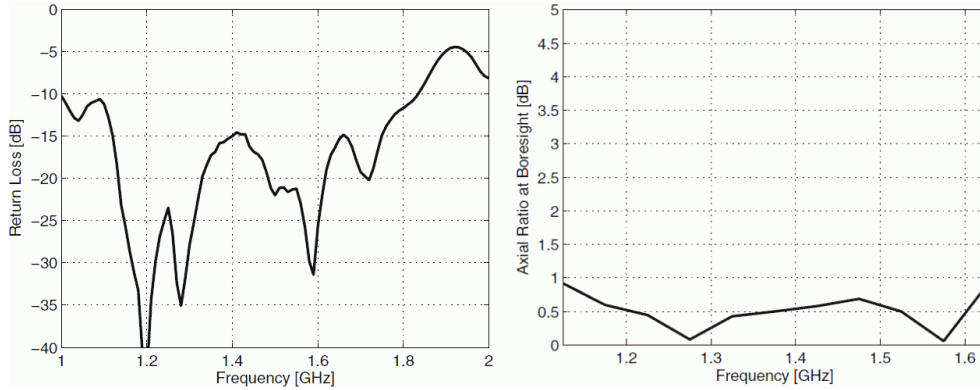


Figure 3.26: RL and AR vs. frequency of an aperture coupled 4-port hDRA with a meandered slot ring (from [43]).

This antenna is relatively large. It uses a rectangular DR $50 \times 50 \times 24\text{ mm}$ ($L \times W \times H$) made of an $\epsilon_r = 10$ material. Due to a low dielectric constant and relatively low frequency, the aperture slots are large, measuring $41 \times 9.4\text{ mm}$ ($l_s \times w_s$). Its large ground plane, measuring $160 \times 160\text{ mm}$ ($L \times W$), is required to accommodate the slots and the feeding network, see Figure 3.25. The experimental performances of this antenna are impressive considering that it was the first wideband DRA designed specifically for the GNSS applications.

Massie et al. in [12] introduce a variation to the earlier design by replacing the rectangular DR with a cylindrical one. The DR had a radius of 31.75 mm and height of 22 mm ($r/h=1.4432$). Similar performances were obtained, however, the slots were reduced to $36 \times 8.8\text{ mm}$ ($l_s \times w_s$), which allowed a smaller ground plane. The DR height was also reduced by 2 mm (8.3%). The back-lobe radiation due to the large aperture slots was also reported.

A further evolution and miniaturisation of the same antenna concept is provided by *Caillet et al.* in [44]. This design uses a higher dielectric constant material of $\epsilon_r = 30$, which reduced DR size to $r=19.05 \text{ mm}$ $h=15.11 \text{ mm}$ ($r/h=1.2607$). To allow uniform loading of the aperture slots, the rectangular slots were replaced with confined arc shaped slots. A back plate housing is added to enclose the feeding circuit and reduce the back-lobe radiation, however, it added 13 mm to the total antenna height, see Figure 3.27.

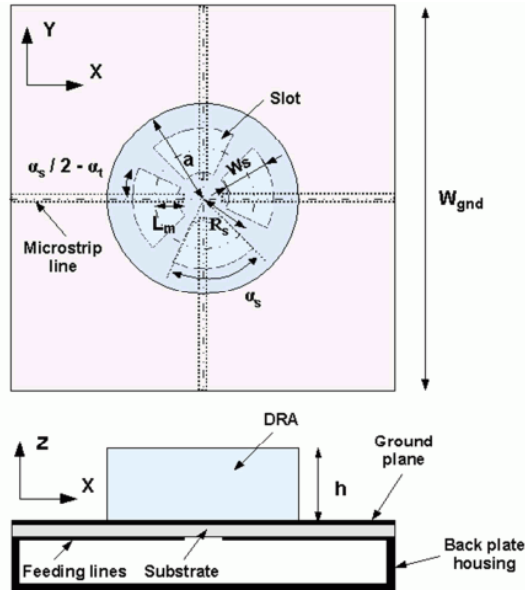


Figure 3.27: Layout of four arc slot excited miniaturized hDRA (from [44]).

The new antenna reduced the DR height by about 7 mm while the ground plane size was reduced to $100 \times 100 \text{ mm}$, or about 61%. However, the total antenna height increased by 5 mm due to the back plate addition. The antenna performances are reduced, mainly due to the use of a higher dielectric constant material. Figure 3.28 shows the experimental results for RL and AR measured at antenna's boresight.

A parametric analysis showed that use of a DR material of $\epsilon_r = 30$ significantly reduced antenna assembly and fabrication tolerances. In particular, it was found that an air-gap on the ground plane made by etching for the excitation slots and DR positioning accuracy over the slots had the most significant impact. The DR ϵ_r 10% error and the DR fabrication tolerances did impact

the performances as well but to a lesser extent. In addition, the analysis had shown that the ground plane size increase reduced the AR beamwidth, which confirmed the findings reported in [30]. Also, it was shown that the antenna absolute gain at the zenith and absolute gain BW were both reduced as a result of the ground plane size increase, which is contrary to [28, pp.164-167].

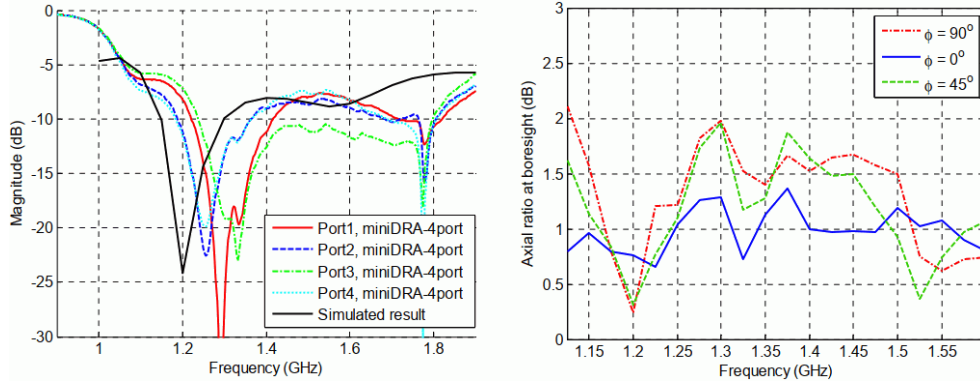


Figure 3.28: RL and AR vs. frequency of miniaturised hDRA (from [44]).

Caillet et al. in [45] further improved the concept by adding a meandered slot ring in the antenna ground plane. The slot ring was added to create an additional resonance to improve the antenna BW. *Podilchak et al.* in [46] optimised the design and added a back cavity to further reduce the back-lobe radiation. To eliminate the air gap between the DR and ground plane a bonding film of the same dielectric constant was used. Figure 3.29 shows the geometry of the PCB layout with the meandered slot ring and the cavity. The lengths and angles are in millimeters and degrees, respectively.

The back cavity increased the antenna total height to 39 mm, which was about 12 mm above the earlier design. In addition, the added meandered slot ring reduced the area underneath the ground plane previously used for the feeding network. That required addition of four coaxial pass-through inserts to bring the signals outside of the back cavity, which further increased complexity of the design. Figure 3.30 shows an exploded view of hDRA with a meandered slot ring and back cavity.

Figure 3.31 shows simulated and measured reflection coefficients and RHCP realized gain. The variations between the individually measured reflection coefficients are believed to be related to fabrication and assembly tolerances [46].

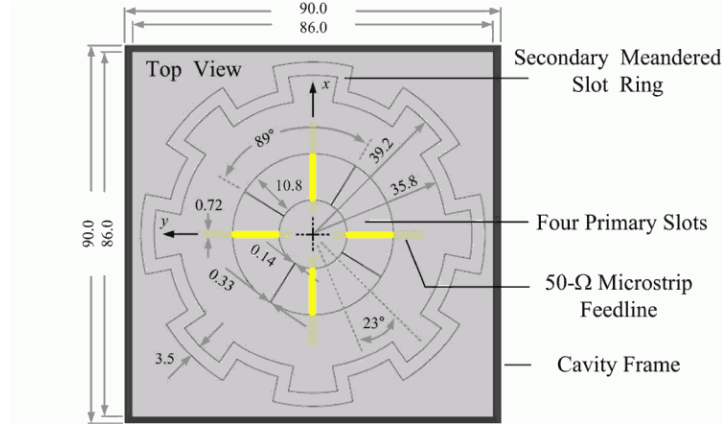


Figure 3.29: hDRA with a meandered slot ring PCB layout and geometry (from [46]).

Figure 3.32 shows the AR as a function of frequency at antenna's broadside and AR versus the beam angle (θ). A fabricated antenna is shown in the inset.

The antennas in [45, 46] improve upon the previous designs and address some of the key problems that resulted from use of the higher dielectric constant materials and large aperture slots for antenna excitation. Comparing to the designs based on $\epsilon_r = 10$ in [43, 12], the new antennas show a narrower impedance BW. However, the realised directional gain $G_R \geq 0 \text{ dBic}$ and $AR \leq 3 \text{ dB}$ BW and beamwidth of the antenna in [46] is a significant improvement.

Table 3.2 provides a performance summary of selected CP DRA that represent or directly contributed to the current state of the art. There are 5 performance parameters that were used to assess the antennas: impedance BW, realised directional gain $G_R \geq 0 \text{ dBic}$ BW and beamwidth (BmW) and, $AR \leq 3 \text{ dB}$ BW and BmW. It is understood that the CP realised gain reflects on the antenna AR performance but it is still used as a more obvious indicator of the CP performance. Antennas in [41, 42] were not designed for GNSS but they are included for comparison because of a different excitation mechanism. Some of the performance and design parameters are unknown (UNK) for these two antennas.

Table 3.3 provides a summary of the key design parameters of the same

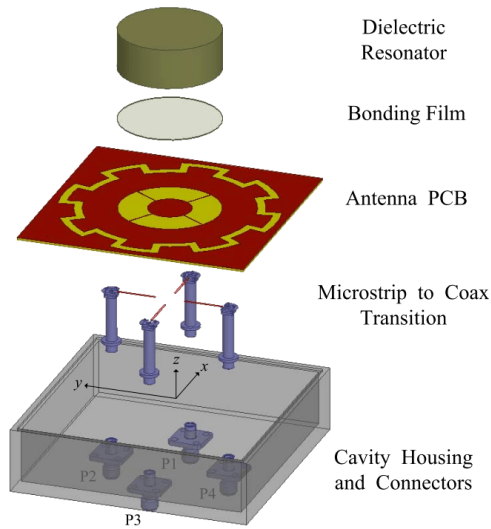


Figure 3.30: hDRA with a meandered slot ring and back cavity exploded view (from [46]).

antennas. The following parameters were considered the most relevant: DR shape (C-cylindrical and R-rectangular), DR dimensions, antenna total dimensions including the ground plane, DR dielectric constant ϵ_r , excitation technique and the number of excitation ports.

The single-port excited CP DRAs were found to be a subject of many publications due to an advantage of a simpler feed network. Typical $AR \leq 3\text{ dB}$ BW for such antennas is below 4% while the AR beamwidth does not exceed 60° . A significant effort has been made to increase the CP performance of the single-port excited DRA. Several concepts were described in [49, 50], however, the reported performances were still inadequate. In addition, the dual-sense CP, which is one of the objectives of this work, cannot be obtained using a single-port excitation approach.

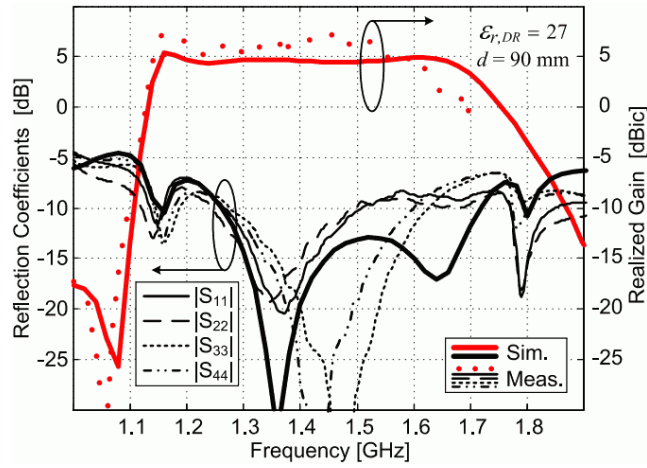


Figure 3.31: RL and realised gain of hDRA with a meandered slot ring (from [46]).

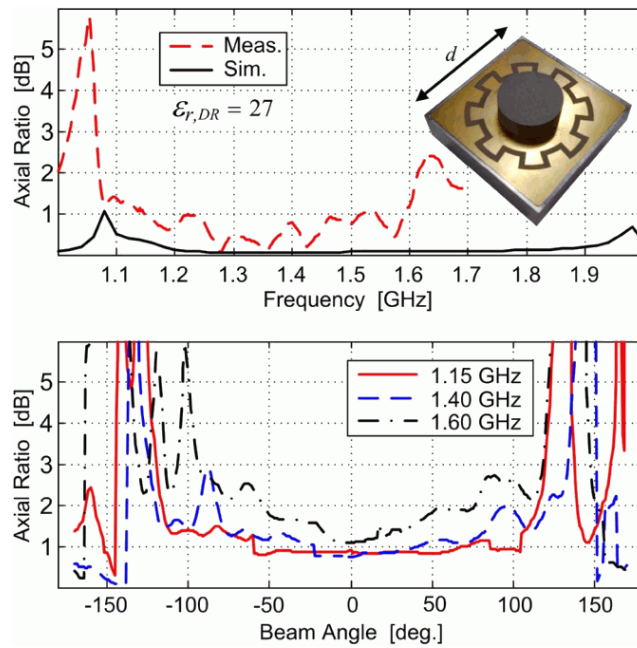


Figure 3.32: Measured AR of hDRA with a meandered slot ring versus frequency and beam angle (θ) (from [46]).

Table 3.2: State of the art multi-port excited CP DRA performance summary.

Ant. ref.	BW (abs.) ($f_L - f_U$) [GHz]	BW [%]	$G_R \geq 0$ dBic		$AR \leq 3$ dB	
			BW [%]	BmW [°]	BW [%]	BmW [°]
[41]	5.0 - 5.75	13.7	UNK	UNK	20	UNK
[42]	1.75 - 2.48 ¹	34.5 ¹	29.8	UNK	25.9	UNK
[43]	1.09 - 1.83 ²	51 ²	>33	60 to 100	>33	130 to 190
[12]	1.09 - 1.82 ³	50 ³	>33	80 to 90	>33	140 to 200
[44]	1.2 - 1.8 ⁴	40 ⁴	>25	90 to 120	37	150 to 190
[46]	1.25 - 1.60	25	42	140	>43	>180

^{1,2,3} Feeding circuit input impedance bandwidth.
⁴ 1.4 - 1.7 GHz $-10 < S_{11} < -7$ dB

Table 3.3: State of the art multi-port excited CP DRA key design parameters.

Ant. ref.	DR shape	DR dimensions ($l \times w \times h$) [mm] or ($r \times h$) [mm]	Antenna dimensions ($l \times w \times h$) [mm]	ϵ_r	Excitation	Number of excit. ports
[41]	C	7×10.8	UNK	9.5	Probe/Strip	2
[42]	C	20×20	$200 \times 200 \times 21$	9.5	Probe/Strip	4
[43]	R	$50 \times 50 \times 24$	$160 \times 160 \times 25$	10	Slot	4
[12]	C	31.75×22	$160 \times 160 \times 23$	10	Slot	4
[44]	C	19.05×15.11	$100 \times 100 \times 29$	30	Slot	4
[46]	C	19.05×15.11	$86 \times 86 \times 39$	30	Slot	4

3.10 Summary

In this chapter results of the literature review and state of the art of the CP DRA and DRA for GNSS applications are presented. Through the review a brief overview of the DRA is given covering their advantages and a concept of operation. An emphasis was put the DR, as the key element of a DRA, by covering the basic DR geometries and their resonant modes, radiation patterns and the DR excitation techniques, which are the key to a DRA performance. In addition, the techniques for CP generation, feeding networks, hDRA and the finite size ground plane effects are covered as well.

The state of the art covers the DRA designed for GNSS applications and other CP DRA concepts that could be adapted for the GNSS applications. In the review, the emphasis was on the pros and cons of the used concepts,

radiation performances and the key design parameters. The GNSS antennas based on a DR were found to provide high performance yet in a compact form. The highest performance antennas use 4-port excitation and a hybrid of the aperture slot coupling with a meandered slot ring. The antennas using a high dielectric constant DR ($\epsilon_r = 30$) show high sensitivity to the assembly and fabrication tolerances.

In the next chapter an attempt will be made to design a compact CP DRA while relying on the existing body of knowledge and experience covered here.

4 Cylindrical DRA design

In this chapter a design process of a DRA for GNSS applications is presented. The design requirements are based on the thesis objectives as outlined in section 4.1. In Chapter 3 it was shown that a DR based concept is a good and flexible basis for a wideband and widebeam GNSS antenna in a compact form factor. Here, different approaches are investigated while building on the existing body of knowledge and experience.

This chapter consists of 8 sections. In section 4.2 a DR shape is selected, which is followed with a cylindrical DR design in section 4.3. Sections 4.4 and 4.5 cover CP generation and DR excitation, respectively. In section 4.6 effects of the finite size ground plane on DRA performances are investigated. Based on the findings from sections 4.4, 4.5 and 4.6, the analytical DR design results from section 4.3 are simulated and analyzed in section 4.7. Section 4.8 provides concluding remarks for this chapter.

In Appendix C additional findings regarding the probe excited cylindrical DR are presented. An antenna concept is proposed based on the findings from this chapter and antenna simulated performances are presented as well. Appendix C is an extension to this chapter and further covers performance of a 4-probe excited CP cylindrical DRA.

4.1 Objectives

The objective of this work is to investigate and validate a new compact all-GNSS FRPA concept based on a DR for defense and industrial applications. The new antenna should improve upon the current state-of-the-art by providing a lower profile antenna while meeting or exceeding current state-of-the-art antenna radiation performances. This is further broken into the following specific performance objectives:

1. A wideband or dual-band antenna providing 10 dB RL impedance from 1164 to 1300 MHz and from 1560 to 1606 MHz.
2. Dual sense circular polarization (CP).
3. 0 dBic realised gain bandwidth meeting or exceeding RL bandwidth.
4. 0 dBic realised gain beamwidth exceeding 140°.
5. 3 dB AR bandwidth meeting or exceeding RL bandwidth.
6. 3 dB AR beamwidth meeting or exceeding 0 dBic realised gain beamwidth.
7. Antenna size not to exceed 90 mm in diameter and 25 mm in height.

4.2 Dielectric resonator shape

In Chapter 3 it was shown that of the three basic DR shapes, the cylindrical and rectangular have a lower DR profile and more design flexibility than the hemispherical shape. However, a trade-off between the cylindrical and rectangular shapes is less obvious.

In section 3.9 two DRA were presented, where one was based on a cylindrical and one on a rectangular DR [12, 43]. The two antennas show very similar performance results, however, the cylindrical DRA had about 10% lower profile. Similar findings are also confirmed in [50]. It was shown that for the same ϵ_r and height, a cylindrical DR will have a lower resonant frequency comparing to a rectangular DR. However, the impedance BW of the cylindrical DR is slightly lower comparing to the rectangular one. This advantage diminishes when $\epsilon_r > 15$, as shown in [50].

The rectangular shape offers one design degree of freedom more comparing to a cylindrical shape, as it was explained in section 3.2.4. However, that degree is negated when the CP radiation is excited using a multi-port excitation since a rectangular DR requires symmetry around two axis as shown in [43], which implies that $W=L$.

Therefore, a cylindrical DR appears to have a small advantage comparing to the rectangular shape, especially for $\epsilon_r < 15$ and when the antenna profile is considered. The BW advantage noted in [50] can be a factor, however, considering the performance of the state of the art antennas in [12, 43], that difference appears to be negligible.

4.3 Design of $HE_{11\delta}$ mode cylindrical dielectric resonator

A cylindrical DR is characterized by its height h , radius r , r/h aspect ratio and ε_r . A cylindrical DR of both low and high r/h ratios can be made to resonate at the same frequency, however, the Q-factor will be different for such two resonators [28, pp.17-18]. The objective here is to select the best trade-off between the size and radiation performances.

In the following subsections a cylindrical DR is designed based a design procedure outlined in [28, pp.25-29]. The described procedure is based on the antenna resonant frequency f_0 , BW and RL requirements. In addition, to the electromagnetic parameters the resonator physical size limitations are considered as well.

4.3.1 Radiation mode

The first step is to identify a resonant mode for DR. In section 3.2.2 it was shown that a free space suspended cylindrical DR can radiate in three different modes: the transverse electric (TE), transverse magnetic (TM) and a hybrid mode (HE). The TE mode was eliminated earlier due to its high Q-factor whereas in case of the TM mode, E -field is constant with the ϕ angle, hence, it cannot support two orthogonal modes within one resonator.

The $HE_{11\delta}$ is the only mode that supports CP since the E -field varies with both the ϕ angle and radius r . Hence, due to cylinder's geometric symmetry an infinite number of offset resonant fields around the circumference can be supported. Therefore, excitation of two orthogonal modes 90° offset around the DR circumference will generate a CP far-field radiation pattern. The $HE_{11\delta}$ mode has two other favorable features as well. It has the lowest Q-factor for a cylindrical DR, hence, the largest impedance BW. And, it radiates like an electric monopole parallel to a ground plane providing a broadside radiation pattern.

A cylindrical DR also supports the higher order HE modes but in the literature they are scarcely mentioned. There is no empirical formula available to calculate the resonant frequency of $HE_{21\delta}$ and $HE_{12\delta}$ modes. In the literature the resonant frequencies of these modes are given as ratios relative to the $HE_{11\delta}$ and $TM_{01\delta}$ resonant frequencies [51].

The higher order HE modes have significantly higher Q-factor values, hence, a narrower BW. *Kajfez et al* in [16] covers $HE_{21\delta}$ and $HE_{12\delta}$ modes and notes that the $HE_{21\delta}$ mode has a very high Q-factor and an undesired radiation pattern. *Guha et al* in [52] reported on a cylindrical DRA radiating in $HE_{12\delta}$ providing a broadside radiation pattern similar to $HE_{11\delta}$ and high radiation efficiency but a narrow BW comparing to the $HE_{11\delta}$ mode.

4.3.2 Quality factor Q and BW

The Q-factor for a DR is based on the BW requirements. The absolute BW (BW_{abs}) is calculated using eq. 4.1, where f_L and f_H are the lower (1164 MHz) and upper (1606 MHz) limits of the GNSS bands, respectively. The resonant frequency f_0 is assumed to match the center of the band and it is calculated using eq. 4.2. Hence, the absolute BW is $BW_{abs} = 442\text{ MHz}$ and $f_0 = 1385\text{ MHz}$. Therefore, the required fractional BW is 0.32 or 32% (eq. 3.34).

$$BW_{abs} = f_H - f_L \quad (4.1)$$

$$f_0 = f_L + \frac{BW_{abs}}{2} \quad (4.2)$$

To obtain the required radiation Q-factor ($Q_u \approx Q_{rad}$, see section 3.3.1), eq. 3.34 is re-arranged into eq. 4.3. For $RL = 10\text{ dB}$, $VSWR$ is around 1.925 (eq. 4.4), which gives the required $Q_{rad}=2.23$. Figure 4.1 shows Q_u as a function of the fractional BW.

$$Q_u = \frac{VSWR - 1}{\sqrt{VSWR} BW} \quad (4.3)$$

$$RL = 20 \log \left(\frac{VSWR - 1}{VSWR + 1} \right) \quad (4.4)$$

4.3.3 Dielectric constant ϵ_r

The dielectric constant ϵ_r requirements are estimated based on Q_u found earlier. Reference [28, pp.26] gives eq. 4.5 for the $HE_{11\delta}$ mode Q_{rad} as a function of ϵ_r and r/h ratio. Figure 4.2 is generated using ϵ_r values for the common commercial dielectric materials and for $0.4 \leq r/h \leq 6$. The acceptable ϵ_r values are those that give a Q_{rad} value at or below the required. Based on Figure 4.2, for $Q_{rad} = 2.23$ the only acceptable ϵ_r is 10 and for $r/h \geq 4.8177$.

4.3. Design of $HE_{11\delta}$ mode cylindrical dielectric resonator

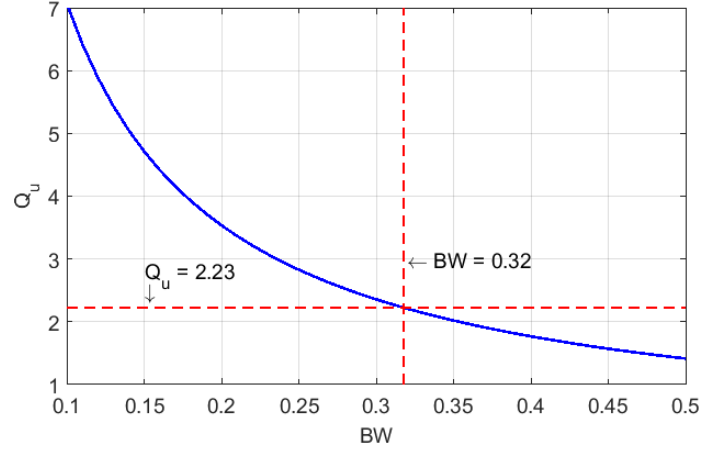


Figure 4.1: Unloaded Q-factor vs. fractional bandwidth.

However, in this case h and r are not bounded by the size restrictions. It will be shown later that the Q_{rad} is further restricted due to the dimensional limitations.

$$Q_{rad} = 0.01007 \epsilon_r^{1.3} \frac{r}{h} \left\{ 1 + 100e^{-2.05\left(\frac{r}{2h} - \frac{1}{80}\left(\frac{r}{h}\right)^2\right)} \right\} \quad (4.5)$$

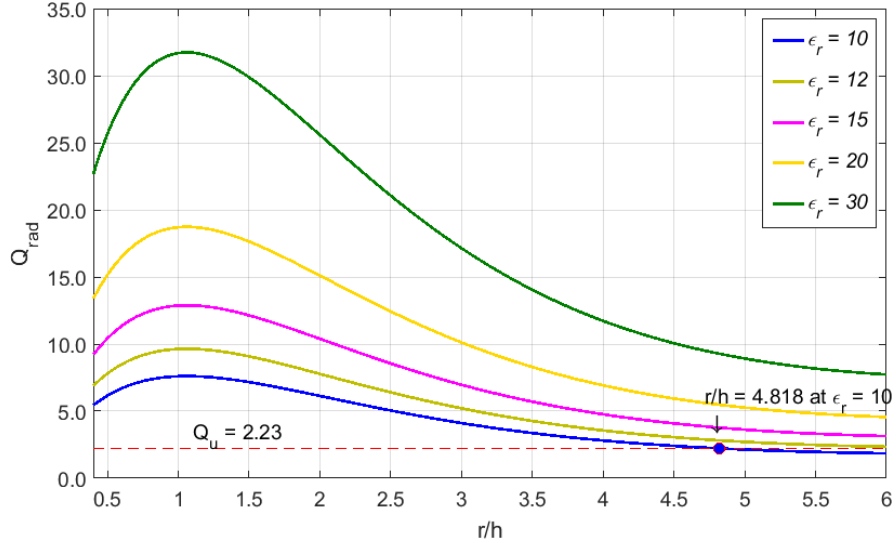


Figure 4.2: $HE_{11\delta}$ mode Q_{rad} vs. r/h ratio.

4.3.4 Wave number $k_0 r$

The DR wave number $k_0 r$ is used to estimate DR dimensions for given values of ϵ_r and r/h . Eq. 4.6 gives $k_0 r$ specific for $HE_{11\delta}$ mode but independent of the resonant frequency whereas eq. 4.7 gives $k_0 r$ as a function of the resonant frequency f_0 , h and r/h ratio but independent of the radiation mode. A point where two $k_0 r$ values calculated using eq. 4.6 and 4.7 intercept, indicates an acceptable r/h value for a given resonant frequency, see Figure 4.3. Note that in eq. 4.7 the DR resonant frequency f_0 and height h are in GHz and cm , respectively.

Figure 4.3 is generated using eq. 4.6 and 4.7 for $\epsilon_r = 12$ and $16 \leq h \leq 30$ mm at $f_0 = 1385$ MHz versus $0.4 \leq r/h \leq 6$. The figure shows an r/h value for each given h , however, independent of the Q-factor.

$$k_0 r = \frac{6.324}{\sqrt{\epsilon_r + 2}} \left\{ 0.27 + 0.36 \frac{r}{2h} + 0.02 \left(\frac{r}{2h} \right)^2 \right\} \quad (4.6)$$

$$k_0 r = \frac{f_0 h \frac{r}{h}}{4.7713} \quad (4.7)$$

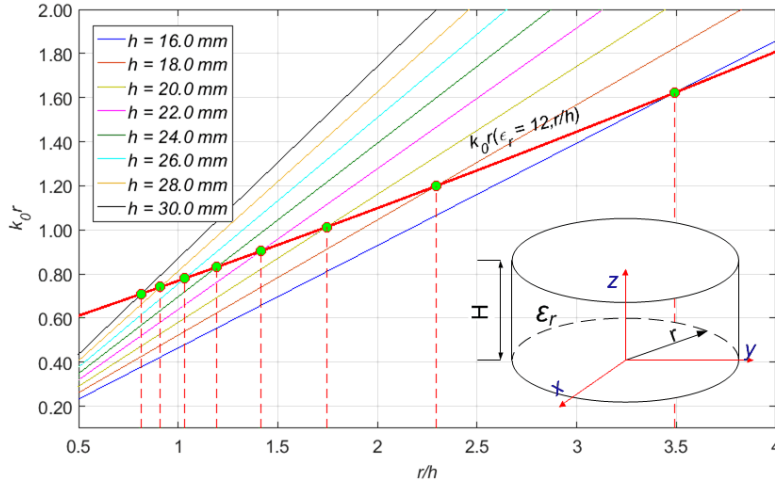


Figure 4.3: $HE_{11\delta}$ mode $k_0 r$ vs. r/h ratio for $\epsilon_r = 12$ at 1385 MHz.

4.3.5 DR dimensions

Using the $k_0 r$ estimated from eq. 4.7, the radius r of a cylinder can be estimated for a given ε_r using eq. 4.6. Figure 4.4 shows h vs. r for an $HE_{11\delta}$ mode resonant cylindrical DR at $f_0 = 1385 \text{ MHz}$. The figure shows that the height of a DR is inversely proportional to its radius, which is anticipated.

Considering the upper limits for h and r of 30 and 45 mm, respectively, the available r/h range is further restricted. Based on eq. 4.5, Figure 4.5 shows available Q_{rad} vs. r/h ratio at $f_0 = 1385 \text{ MHz}$ when h and r are limited to 30 and 45 mm, respectively. Note that in Figure 4.5 Q_{rad} on the left-hand side (LHS) is limited by h while on the right-hand side (RHS) it is limited by r .

Table 4.1 shows the minimum available Q_{rad} values under the same conditions as in Figure 4.5. The minimum Q_{rad} is limited by r , thus, the minimums for all ε_r values are at $r = 45 \text{ mm}$, which is the maximum allowed. The minimum available $Q_{rad} = 5.42$ for $\varepsilon_r = 10$, which obviously does not meet the required $Q_{rad} \approx Q_u = 2.23$.

Table 4.1: $HE_{11\delta}$ mode minimum Q_{rad} at 1385 MHz for $r = 45 \text{ mm}$.

ε_r	h [mm]	r/h	Q_{rad}
10	19.36	2.3232	5.42
12	17.28	2.6020	6.14
15	15.09	2.9768	7.03
20	12.73	3.5341	8.18
30	10.13	4.4378	10.24

Table 4.2 and 4.3 provide dimensions and theoretical Q_{rad} values for a $HE_{11\delta}$ mode resonant cylindrical DR at 1385 MHz for ε_r 10 and 12. The dimensions are obtained from eq. 4.6 and 4.7 for a range of given h values $18 \leq h \leq 30 \text{ mm}$ and $0.4 \leq r/h \leq 6$. The Q_{rad} values are obtained from eq. 4.5 for the r/h values found for Figure 4.3.

All the findings this far indicate that the required Q_{rad} cannot be met based on a simple cylindrical DR. The results also show that the minimum Q_{rad} values exist for highest r/h ratios. However, this work will continue considering that eq. 4.5 and 4.6 are only a good starting point [28, pp.25]. As a part of further investigation, results from Table 4.2 and 4.3 will be simulated. Before the simulations can be conducted, the excitation mechanism needs to

4.3. Design of $HE_{11\delta}$ mode cylindrical dielectric resonator

be designed and impact of the finite size ground plane investigated. These are provided in the subsequent sections.

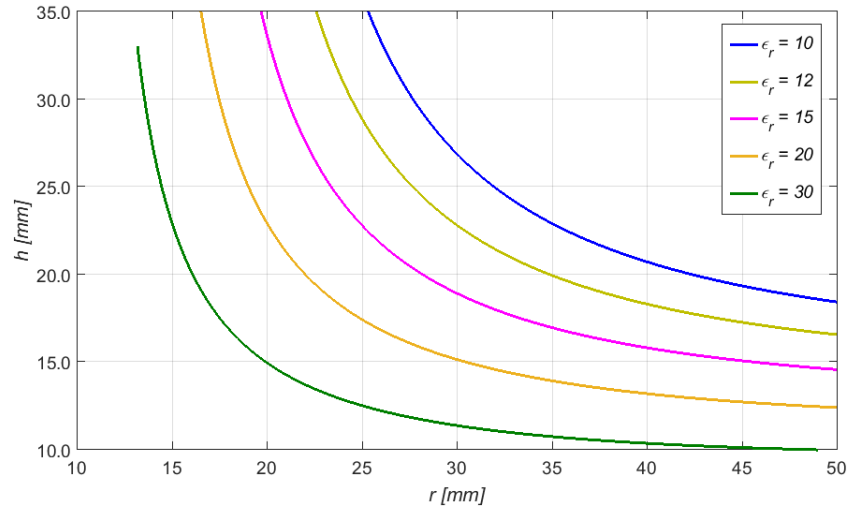


Figure 4.4: DR h vs. r for $HE_{11\delta}$ mode at 1385 MHz.

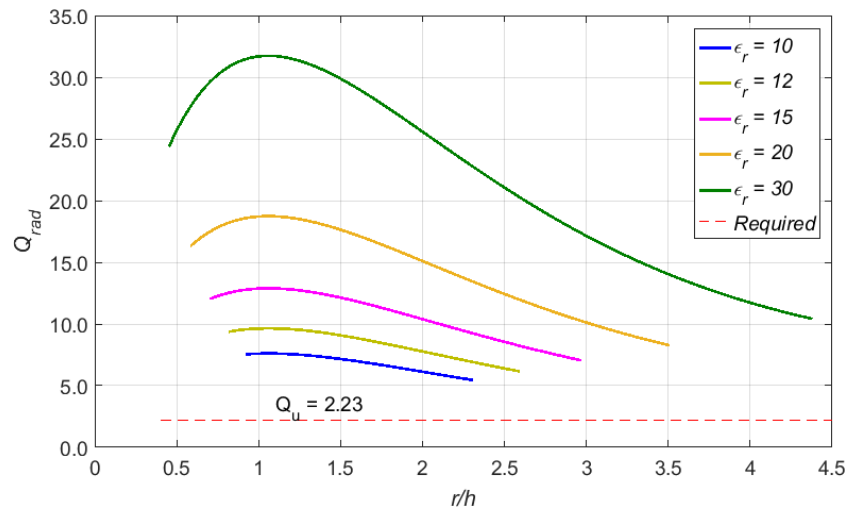


Figure 4.5: Available Q_{rad} vs. r/h at 1385 MHz for $r \leq 45$ mm and $h \leq 30$ mm.

Table 4.2: $HE_{11\delta}$ mode DR dimensions for $\epsilon_r = 10$ at 1385 MHz.

h [mm]	r/h	r [mm]	Q_{rad}
20.0	2.119	42.38	5.87
22.0	1.672	36.79	6.84
24.0	1.387	33.29	7.34
26.0	1.187	30.86	7.56
28.0	1.038	29.07	7.61
30.0	0.923	27.70	7.55

Table 4.3: $HE_{11\delta}$ mode DR dimensions for $\epsilon_r = 12$ at 1385 MHz.

h [mm]	r/h	r [mm]	Q_{rad}
18.0	2.295	41.30	6.95
20.0	1.745	34.89	8.48
22.0	1.415	31.14	9.25
24.0	1.194	28.64	9.58
26.0	1.033	26.86	9.64
28.0	0.911	25.51	9.55
30.0	0.815	24.46	9.36

4.4 Circular polarization feeding network

This work does not include a feeding network design. Instead an antenna feeding circuit previously designed and fabricated for testing of the antennas described in [44, 45, 46] will be used. It is a broadband circuit designed specifically for 4-port GNSS antennas excited in a quadrature [53], see Figure 4.6.

4.5 Dielectric resonator excitation

The literature shows that the slot aperture coupling has significant advantages in terms of the impedance BW over the other studied techniques (Table 3.2 and 3.3). However, at the GNSS frequencies the required slot area is significant relative to the DR footprint. In case of the antennas in [12, 43], the slots were not confined to the DR footprint due to their size, whereas the arc-shaped slots in [44, 46], which were confined, occupied over 77% of the

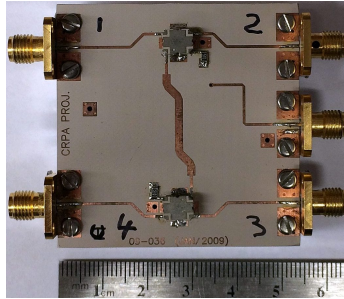


Figure 4.6: Antenna feeding circuit.

DR footprint.

Due to a large slot area, all of the studied slot coupled GNSS antennas experienced significant back-lobe radiation [12, 44, 46]. Use of a back cavity to contain the back-lobe radiation significantly increased antenna complexity and size [46]. In addition, the position of the slots in all of the cases was not optimal for the $HE_{11\delta}$ mode. To accommodate all 4 slots they had to be moved towards the DR edges. An edge position is sub-optimal as shown in sections 3.2.2. Therefore, use of the aperture slots for 4-port DR excitation does not appear to be the best option.

The co-planar and microstrip line excitation techniques are excluded primarily because of their susceptibility to the surface-wave interference and feeding network line coupling. The line coupling could be eliminated by placing the feeding network under the ground plane. However, the surface-wave susceptibility would still remain.

Use of a probe-based excitation at the lower frequencies where aperture coupling is not feasible is suggested in [27, pp.189]. It is also suggested that the impedance matching can be achieved by adjusting the probe height and position. Use of the probe radius as a design parameter is not mentioned in the literature. For $HE_{11\delta}$ mode excitation in both [27] and [28], a probe is usually located at a DR outer edge just touching its surface, however, the impact of the contact area on the coupling efficiency is not addressed in the texts.

When a high permittivity material is used, coupling between a probe and DR becomes sensitive to the probe location and the interface between the two [27, pp.189]. A conformal strip is a variation of the probe but with additional

parameters such as width, height and shape. All three can be used to improve impedance matching as shown in Figure 3.22.

Therefore, the $HE_{11\delta}$ mode excitation using a probe based technique should provide more effective coupling than the slot aperture in case of a 4-port excitation at the GNSS frequencies. In addition, it would eliminate requirements for the back cavity, which was found to be the main disadvantage of the state-of-the-art antennas (section 3.9). In terms of the performances, it was shown in [42, 50] that the conformal strips can provide similar impedance BW and comparable to those reported for the slot aperture coupled antennas in [43, 44, 46].

4.5.1 Design of probe based coupling

The literature does not describe any design techniques for the probe based DR excitation. To investigate performance of a simple round probe and conformal strip excitation both cases were simulated using the High Frequency Solid Structure modeler (HFSS), which is a finite element electromagnetic simulator [6]. The radiation boundary was set as a 2nd order absorbing boundary or the perfectly matched layer (PML), as described in the HFSS documentation.

The simulated antenna was based on a cylindrical DR designed in section 4.3, see Table 4.3. A DR resonant at 1385 MHz of $\epsilon_r = 12$, $r = 28.64 \text{ mm}$ and $h = 24.0 \text{ mm}$ ($r/h = 1.194$) placed on a ground plane of $r_{GP} = 200 \text{ mm}$ was used. The probe was fed through the ground plane using a 50Ω via-through. The 50Ω via-through was designed using the HFSS optimization tool where the via pad radius and pad to ground plane radius (Figure 4.7.d) were optimised for a minimum RL.

To investigate impact of 1 vs. 4-port excitation and a simple round probe vs. conformal strip, all four cases were simulated. To simulate both, the round probe and conformal strip, under the same conditions, the first step was to find ideal dimensions and positions for both. In case of the round probe, the radius, height and probe position with respect to the DR edge were varied, whereas in case of the strip its height, width and the transition from the via-pad were varied (Figure 4.7). Using the HFSS optimization tool, both concepts were optimised for the maximum impedance BW within a band centered at 1385 MHz.

The results show that an ideal height for both probe and strip is the same as the resonator height, which confirms findings reported in [50, 42]. An ideal

round probe appears to be a very thin wire half embedded into the DR body. This finding confirms that a probe requires a finite surface contact area with a DR. To keep it within the realm of fabrication possibilities, the minimum probe diameter was limited to 0.5 mm.

In case of the conformal strip, it was found that the width tends to converge around around 2.16 mm. Tapering the strip over the first 10% of its length appears to provide minor performance improvements. Figure 4.7 shows details of the thin probe and conformal strip line obtained through the described optimization process. The dimensions for the conformal strip line obtained using the optimization tool are shown in Figure 4.7.e.

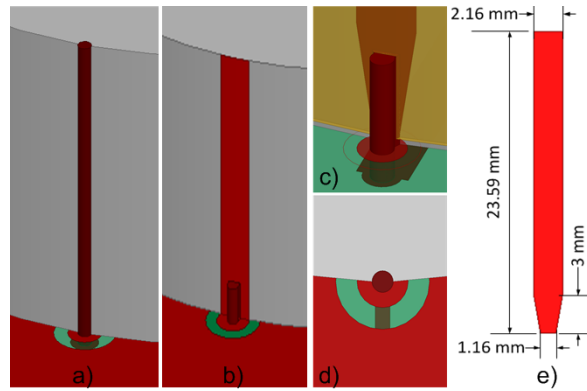


Figure 4.7: Probe and conformal strip excited DR: a) probe, b) conformal strip, c) via-pad to strip tapered transition, d) via-pad and ground plane detail and e) conformal strip optimised dimensions.

4.5.2 Probe based coupling performance

The S_{11} parameter and antenna radiation efficiency factor (η_{ant}) are shown in Figure 4.8, whereas performance summaries are provided in Table 4.4 and 4.5. The strip line appears to provide better impedance BW comparing to the thin wire probe. The difference is especially significant in case of the 4-port excitation where the strip line provides 17.2% vs. 10.0% impedance BW provided using 4 thin wire probes. It is also interesting that the 4-port input impedance resonant frequency shifts up by about 5.8% relative to the 1-port excitation for both the probe and strip line.

At the same time, the 4-port excitation appears to shift the peak η_{ant} by about 11% below the 1-port excited DR for both the thin wire probes and conformal strips (Table 4.5). In addition, the peak η_{ant} does not match the impedance resonant frequency and it is lower by more than 10% in case of the 4-port excitation. For the DR excited using 4 conformal strips, the peak radiation efficiency is at 1315 MHz whereas the impedance resonant frequency is at 1450 MHz. In case of the 4 probes, the results are similar. This likely indicates that the addition of multiple probes modifies the DR boundary conditions, which is more evident in case of the conformal strips because of a larger contact area.

Effects of the 4-probe coupling on AR and realised gain (G_R) beamwidth and BW were investigated as well. Both AR and G_R beamwidth and BW do not appear to be significantly affected and show similar results for both the thin wire probes and conformal strips, see Figure 4.9 and 4.10. It is interesting that both $AR < 3\text{ dB}$ and $G_R > 0\text{ dBic}$ BW at antenna boresight exceed the 10 dB RL impedance BW by a factor of two.

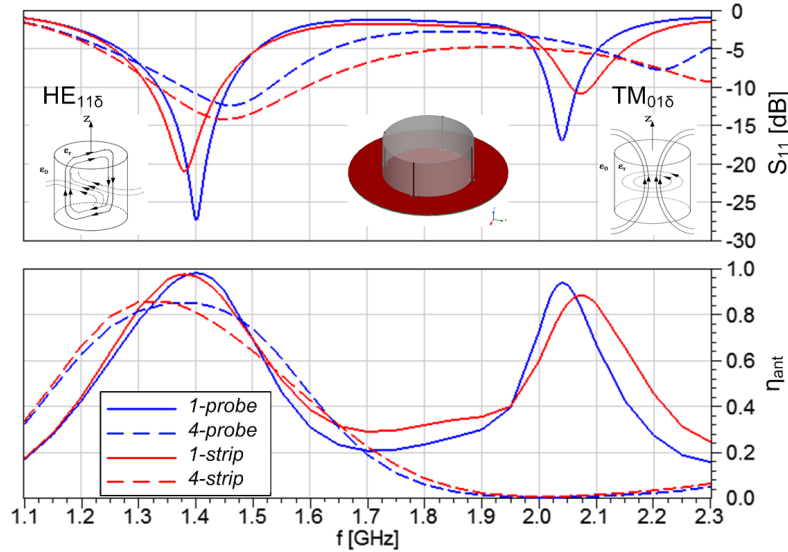


Figure 4.8: S_{11} and η_{ant} of 1 and 4-probe $HE_{11\delta}$ mode excited DR.

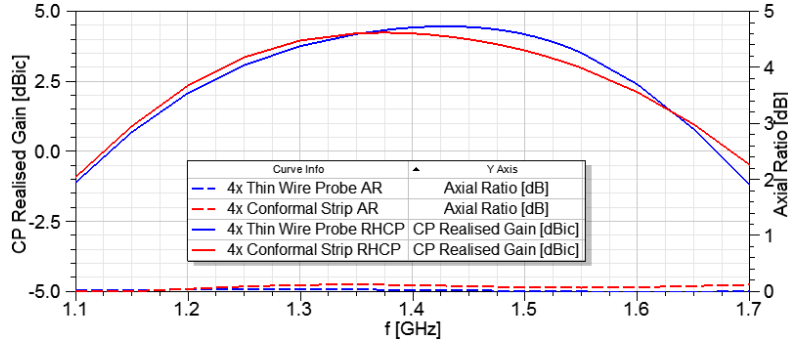
Overall, the conformal strip approach appears to provide better performances, ease of fabrication and more degrees of freedom for impedance matching comparing to a simple thin wire probe. Although there are no noticeable advantages in the cases of the AR and G_R beamwidth and BW performances.

Table 4.4: Resonant frequency, BW and Q_L of 1 and 4-port $HE_{11\delta}$ mode DR.

Excit. type	No. Ports	f_r [MHz]	f_L [MHz]	f_H [MHz]	f_c [MHz]	BW		Q_L
						[MHz]	[%]	
Probe	1	1400	1334	1457	1396	123	8.8	7.56
Strip	1	1380	1318	1443	1381	125	9.1	7.36
Probe	4	1460	1382	1528	1455	146	10.0	6.64
Strip	4	1450	1337	1588	1463	251	17.2	3.88

Table 4.5: η_{ant} of 1 and 4-port $HE_{11\delta}$ mode excited DR.

Excitation type	No. Ports	Max. η_{ant} f [MHz]	η_{ant}
Probe	1	1400	0.990
Strip	1	1380	0.985
Probe	4	1380	0.850
Strip	4	1315	0.875

Figure 4.9: AR and G_R bandwidth of 4-probe $HE_{11\delta}$ mode excited DR.

4.6 Finite size ground plane

In this section results of an investigation of the finite size ground plane effects on the DRA radiation properties are presented. The work is based on the same antenna concept used in section 4.5 but it focuses only on the 4-port excitation using the thin wire probes and conformal strips. The ground plane radius r_{GP} of 50 mm, 100 mm and 200 mm is used, which represent about $\lambda/4$, $\lambda/2$ and λ of the free-space propagation wavelength λ_0 for the lowest simulated frequency (1.1 GHz), respectively.

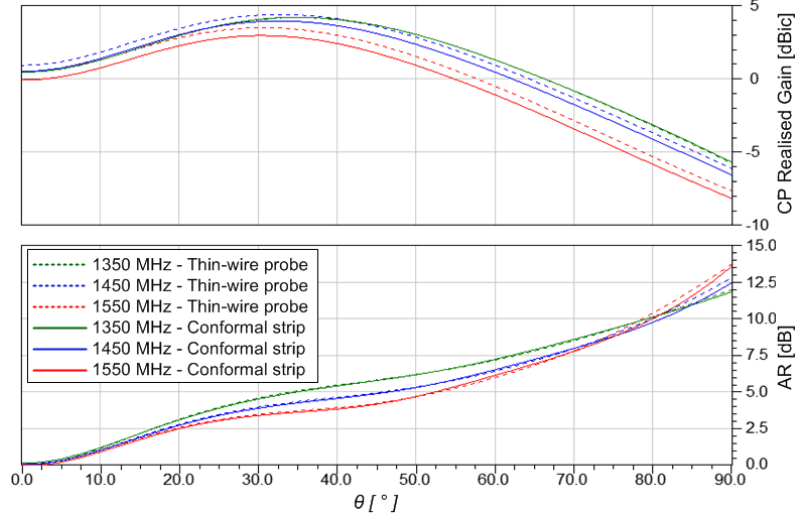


Figure 4.10: G_R and AR beamwidth of 4-probe $HE_{11\delta}$ mode excited DR.

Figure 4.11 shows the RL and η_{ant} responses. For both excitation cases the ground plane size has a minor impact for $r_{GP} \geq \lambda/2$, which confirms observations reported in [30]. The BW difference observed earlier between the thin wire probe and conformal strip is not affected by the ground plane size. However, for the $\lambda/4$ ground plane, the resonant frequency and peak η_{ant} both appear to shift lower. The RL BW does not appear to be affected significantly. In addition to being shifted in frequency, the peak η_{ant} also increased by about 10% for both excitation cases. This is not anticipated and not mentioned in the literature.

The ground plane size appears to have a minor impact on the AR BW at the antenna zenith. For all the sizes and both excitation techniques antenna maintains $AR < 1 dB$ from 1.1 to 1.9 GHz (Figure 4.12). In contrast, the realised gain BW ($G_R > 0 dBic$) is affected by the ground plane size. It is the highest for $\lambda/2$ and shows a coverage from approximately 1.05 to 1.75 GHz and 1.05 to 1.72 GHz in case of the conformal strip and thin wire probe excitation, respectively. The lowest realised gain BW is for λ providing a coverage from approximately 1.14 to 1.68 GHz for both excitation techniques.

The AR and G_R beamwidths are significantly more affected by the ground plane size and the impact in both cases appears to be inversely proportional,

4.7. Simulated DR radiation performances

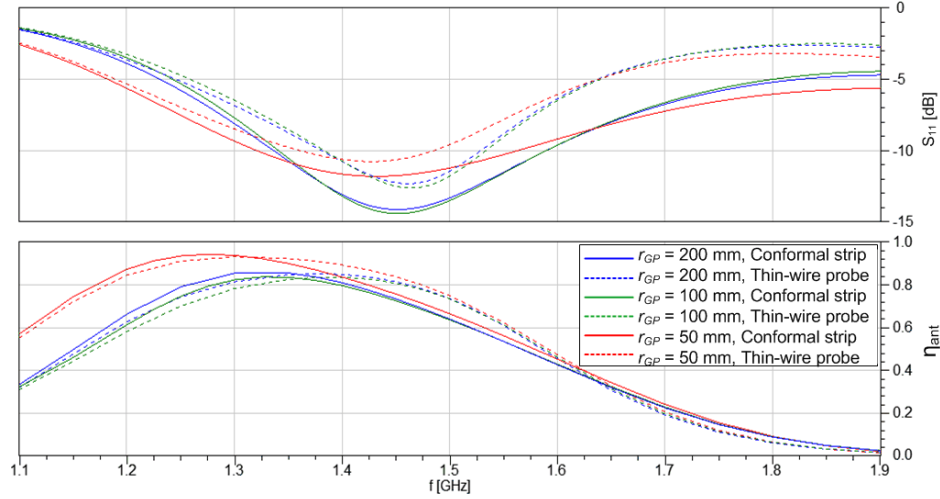


Figure 4.11: Ground plane size impact on RL and η_{ant} of a 4-port excited cylindrical DR.

as expected, see Figure 4.13. The impact is consistent for both test frequencies, 1.35 and 1.55 GHz. For the λ ground plane radius, the radiation pattern does not have a maximum at the zenith. The same effects were also reported in [30] where it was attributed to the field diffraction from the ground plane edges.

The AR and G_R beamwidth simulation was done only for 4-port excitation using the thin wire probes. The thin wire probe appears to have less of an impact on the DR boundary conditions, which allows for easier isolation of the ground plane size effects.

4.7 Simulated DR radiation performances

Now that the key elements of a DRA have been investigated, the results of the DR design presented in section 4.3 can be assessed. The objective is to compare the BW and Q-factor values obtained analytically with the results based on simulations. The Q-factor estimated based on the RL in this case is Q_L .

The set of DRs $\epsilon_r = 12$ from Table 4.3 designed for the $HE_{11\delta}$ mode and ranging in height from 18 to 30 mm were simulated in a frequency range

4.7. Simulated DR radiation performances

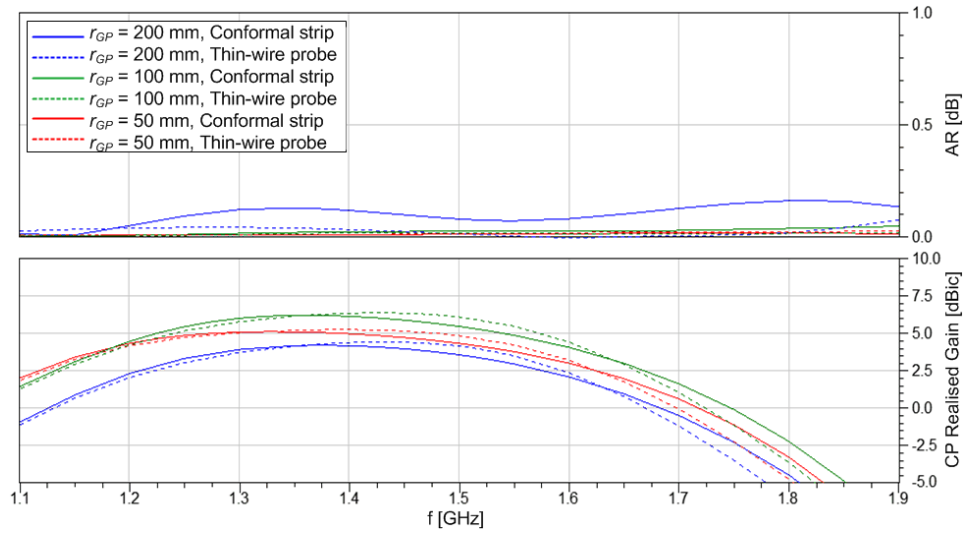


Figure 4.12: Ground plane size impact on AR and G_R BW of a 4-port excited cylindrical DR.

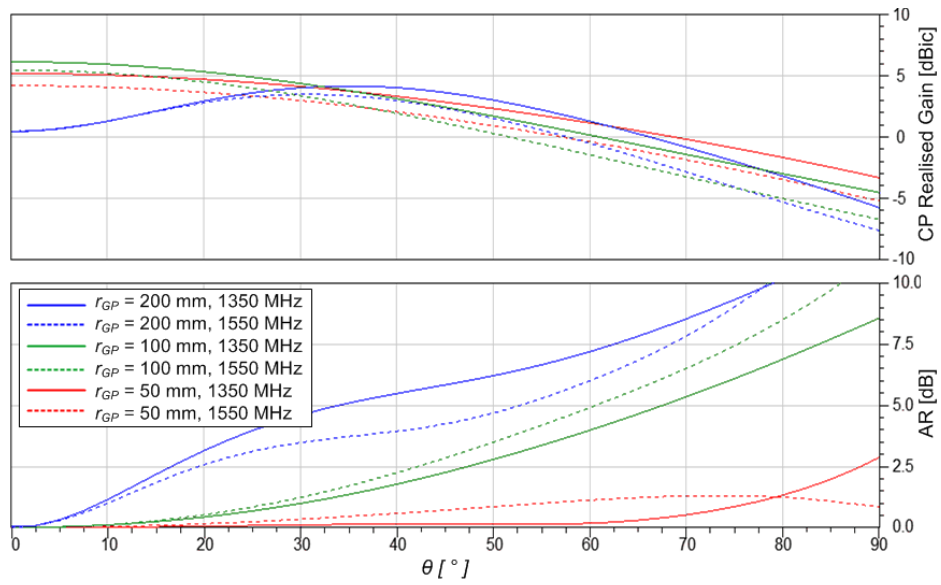


Figure 4.13: Ground plane size impact on AR and G_R beamwidth of a 4-port excited cylindrical DR.

between 1.1 and 2.4 GHz in steps of 20 MHz. To minimize the the impact on the DR boundaries, the DR was excited using one thin wire probe of the same length as the DR height. The probe radius was 0.25 mm and it was fed through the ground plane. The ground plane had a radius of 200 mm or approximately one λ .

4.7.1 Resonant frequency and impedance BW

Figure 4.14 shows the antenna simulated S_{11} and η_{ant} responses. The first resonance appears between 1370 and 1530 MHz, which is the $HE_{11\delta}$ mode, while the second resonance appears between 1680 and 2310 MHz, which is the $TM_{01\delta}$ mode. Note that $TE_{01\delta}$ mode cannot be excited when 4-port excitation in quadrature is used, which is confirmed in Figure 4.14.

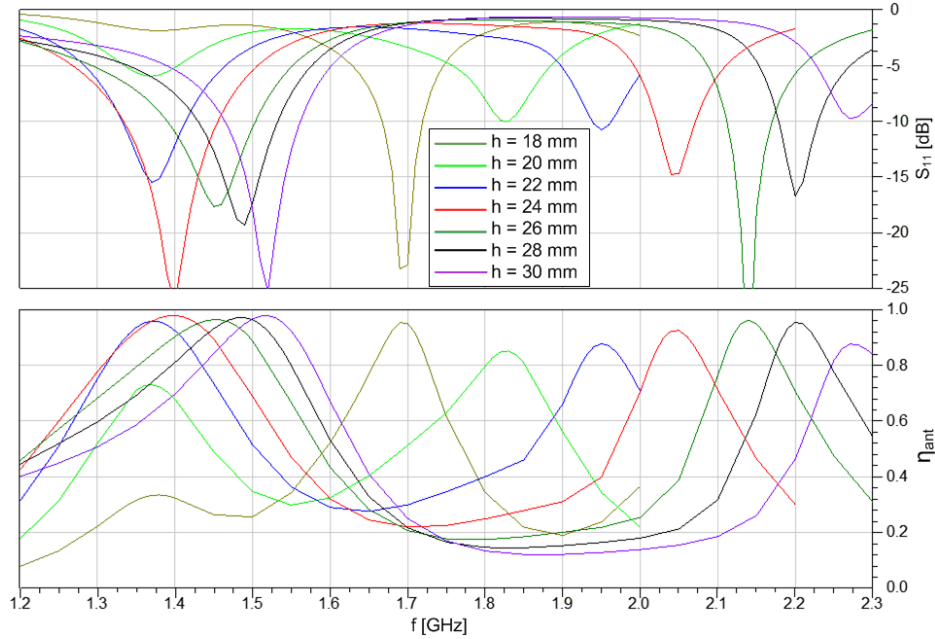


Figure 4.14: Simulated S_{11} and η_{ant} for 1-probe excited DR of $\epsilon_r = 12$.

Table 4.6 and 4.7 summarize the simulated resonant frequency, Q-factor and BW performances. Poor input impedance for DR heights of 18 and 20 mm, corresponding to r/h ratio of 2.295 and 1.745, respectively, is noticeable. The resonant frequency f_0 for $h \geq 24$ mm (low r/h ratio) appears to shift upward as h is increased and r/h ratio is decreased. The same trend is observed for

the $TM_{01\delta}$ mode. The DR resonances based on the S_{11} and the peak η_{ant} responses match for all the design cases.

 Table 4.6: $HE_{11\delta}$ mode simulated resonant frequency.

h [mm]	r/h	f_r [MHz]	f_r <i>err.</i>		f_L [MHz]	f_H [MHz]	f_c [MHz]
			[MHz]	[%]			
18.0	2.295	1370	-15	-1.1	-	-	-
20.0	1.745	1370	-15	-1.1	-	-	-
22.0	1.415	1370	-15	-1.1	1331	1415	1373
24.0	1.194	1400	15	1.1	1334	1457	1395
26.0	1.033	1450	65	4.7	1390	1504	1447
28.0	0.911	1490	105	7.6	1430	1533	1481
30.0	0.815	1520	135	9.7	1464	1562	1513

 Table 4.7: $HE_{11\delta}$ mode simulated BW and Q-factor.

h [mm]	r/h	BW		Q_L (Sim.)	Q_L (Design)	Q_u (Design)
		[MHz]	[%]			
18.0	2.295	-	-	-	3.13	6.25
20.0	1.745	-	-	-	3.95	7.9
22.0	1.415	84	6.1	10.9	4.55	9.1
24.0	1.194	123	8.8	7.6	4.75	9.5
26.0	1.033	114	7.9	8.5	4.8	9.6
28.0	0.911	103	6.9	9.6	4.7	9.4
30.0	0.815	98	6.5	10.3	4.25	8.5

For $h \geq 24\text{ mm}$ the η_{ant} is higher for the $HE_{11\delta}$ mode by 5 to 15% comparing to the $TM_{01\delta}$ mode. This is expected considering that the position of the probe on the DR edge is not optimal for the $TM_{01\delta}$ mode excitation.

The simulated Q_L values in Table 4.7 were calculated from the RL data. For the design Q_L it is assumed that $Q_L \approx Q_u/2$ based on another assumption that the design DRs are connected to matched transmission line. Then the design is $Q_{rad} \approx Q_u \approx Q_{ext}$ (section 3.3.1).

The resonant frequency error for $18 \leq h \leq 24\text{ mm}$ and $2.295 \geq r/h \geq 1.194$ is around 1.1%. However, for $h > 24\text{ mm}$ and $r/h < 1.194$ the error increases, reaching 9.7% at $h = 30\text{ mm}$ ($r/h = 0.815$), which is unexpected considering that the r/h ratio is well within the design limits ($0.4 \leq r/h \leq 6$).

The highest RL BW is achieved for $h=24$ mm ($r/h=1.194$). The achieved BW is 135 MHz or 0.088 (8.8%), which corresponds to $Q_L = 7.6$ or $Q_u = 15.2$. This is about 5.7 points worse than it is predicted by the design. Overall, the simulated Q_u values show discrepancies exceeding 100%, see Table 4.7.

4.7.2 Radiation mode

To confirm the DR radiation mode, the far-field radiation patterns and internal fields were investigated for a DR of $h = 24$ mm ($r/h = 1.194$) and $\varepsilon_r = 12$. In Figure 4.15.a, the far-field radiation at 1375 MHz shows a broadside radiation pattern that resembles a horizontal dipole, which matches the $HE_{11\delta}$ mode. At 2070 MHz the radiation pattern resembles a vertical quarter-wavelength monopole, which matches the $TM_{01\delta}$ mode.

Figure 4.15.b shows H -field in the equatorial plane at 1375 MHz. The field pattern matches the $HE_{11\delta}$ mode pattern described and shown in [16]. It is interesting that the excitation probe position on the edge of DR is not optimal for the $TM_{01\delta}$ mode, however, the radiation efficiency of the $TM_{01\delta}$ mode exceeds 90%, which is unexpected.

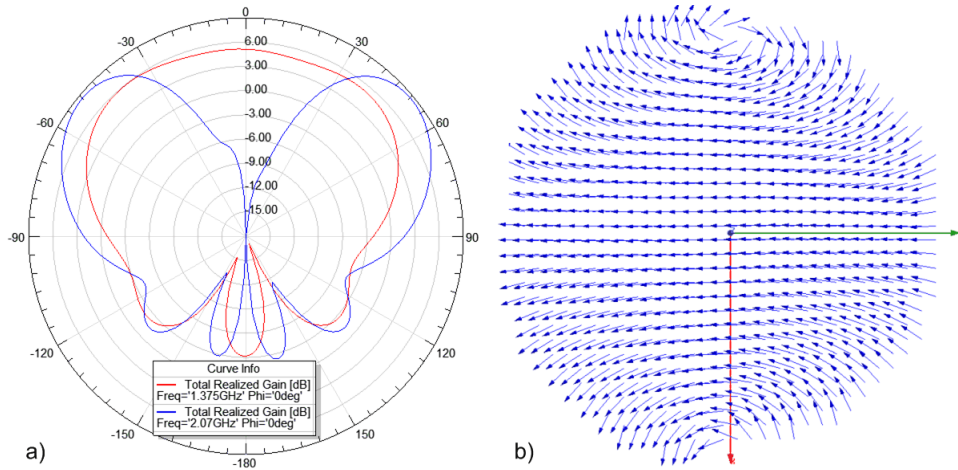


Figure 4.15: a) Far-field radiation patterns at 1375 MHz ($HE_{11\delta}$) and 2070 MHz ($TM_{01\delta}$) modes and b) $HE_{11\delta}$ mode equatorial plane H -field at 1375 MHz.

4.7.3 Summary of findings

The $HE_{11\delta}$ mode simulated results only partially confirm analytical predictions from section 4.3. The most significant finding is related to the Q-factor performance. Results show that the simulations do not confirm Q_L predicted by the analytical design. However, that should not be a surprise since the accuracy of the Q-factor deteriorates as the dielectric constant decreases [27, pp.143]. Figure 4.16 shows several cases of theoretical, simulated and experimentally obtained Q_L data sets vs. the r/h ratio. The theoretical Q_L data are based on Q_{rad} calculated using eq. 4.2 for ϵ_r of 10, 12 and 27. It is assumed that $Q_L \approx Q_u/2$ as explained in section 4.7.1.

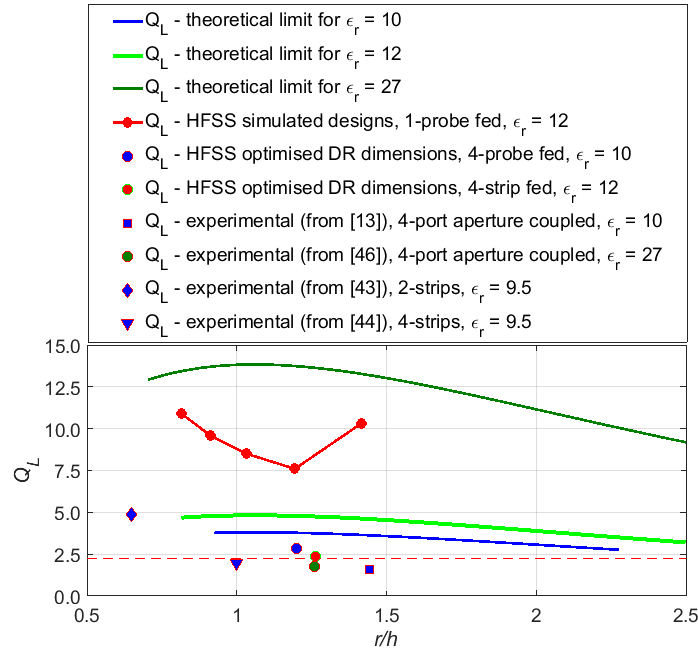


Figure 4.16: $HE_{11\delta}$ mode simulated and design Q-factor vs. r/h ratio.

Based on the five simulated Q_L data points covered in section 4.7 for $\epsilon_r=12$, the Q_L value is the lowest around $r/h = 1.194$ ($h = 24$ mm). However, based on theoretical data for $\epsilon_r=12$, it is anticipated that Q_L would be the highest for $0.9 \leq r/h \leq 1.3$ then gradually decreasing for $r/h \geq 1.2$. In addition to unconfirmed trend between the simulated and theoretical, the simulated Q_L values are significantly higher showing a difference ranging between 50 and 100%.

For the two cases of optimised DR dimensions, the Q_L values are closer to the theoretical predictions. The DR dimensions were optimised for the number of excitation ports, type of excitation (thin-wire probe vs. conformal strip) and ground plane size, see Appendix C. The two data points show that an optimised DR can have significantly lower Q_L .

The four data points based on the experimental results from the literature show a trend similar to the optimised DR cases already covered. The data point from [44], which is based on a 4-port aperture coupled $\varepsilon_r = 27$ DR, shows Q_L well outside the theoretical limits. However, the design is considered hDRA, which implies resonator loading. The data points from [12, 41, 42] are based on RL measurements at the feeding network input. Hence, they do not indicate DR performance but rather the feeding network performance. Nevertheless, these points are included for reference purposes.

4.8 Conclusion

In this chapter a design process for a CP GNSS antenna based on a cylindrical DR was presented. Based on the simulation results, it is shown that a DRA based on a cylindrical $\varepsilon_r = 12$ DR excited using 4 conformal strips fed in a quadrature can not meet the thesis objectives. In addition, it is also shown that the analytical design process commonly used in the literature does not provide sufficient indications of antenna performances at least for the $HE_{11\delta}$ mode. Significant discrepancies are also shown between theoretical and simulated Q_L . The two simulation experiments described in Appendix C confirmed that an optimum DRA design needs to consider all the antenna key elements such as excitation technique, number of excitation ports, ground plane size and impedance matching in addition to the DR dimensions, shape and ε_r .

In the next chapter an attempt is made to further improve the antenna radiation performances and to reduce the mutual coupling between the excitation ports by DR loading using periodic structures.

5 Annular DRA with periodic loading

In this chapter techniques to improve the radiation performances of a cylindrical DRA are reviewed and investigated. In Chapter 4 it was shown that a simple cylindrical DR shape alone can not attain the desirable bandwidth. Such response could be anticipated considering that the required Q-factor exceeds the DR theoretical for any given ϵ_r in a range of $10 \leq \epsilon_r \leq 30$.

In the literature, a DRA bandwidth is usually defined by the input impedance, hence, the bandwidth enhancement techniques described in the literature mostly address the improvements to the impedance response. However, based on *Rao et al* [5], a GNSS antenna minimum gain bandwidth might be a better indication of a true performance than the impedance bandwidth. Similar statements are also made by *Luk et al* in [27, pp. 177-209].

5.1 Review of bandwidth enhancement techniques

Luk et al in [27, pp.177-209] and *Petosa* in [28, pp.119-148] both cover DRA bandwidth enhancement techniques. The discussed techniques are based on the dielectric constant, resonator loading, hybrid DRA, use of multiple resonators and use of the external matching networks.

5.1.1 Dielectric constant

Reducing the dielectric constant is the simplest way to lower the Q-factor and thus increase the antenna bandwidth. However, as the dielectric constant is reduced, the resonator size will increase for a given resonant frequency, which is not desirable in this case where a compact and low-profile antenna is required. In addition, it was shown in Appendix C that use of $\epsilon_r = 10$ did not significantly increase antenna impedance bandwidth comparing to $\epsilon_r = 12$.

In fact, it appears that impedance matching is more difficult to achieve for the lower ϵ_r .

5.1.2 Impedance matching

The impedance matching networks such as quarter-wave transformers and stubs can be used to increase the DR impedance and radiation bandwidth. Such networks are usually placed after the DR coupling mechanism, but sometimes they can be incorporated within the coupling mechanism itself. An example of the latter is a microstrip-fed aperture-coupled DR, where a microstrip stub extends past the slot, see section 3.4.1 and Figures 3.14 and 3.15.

Optimization of DR coupling mechanism to improve the bandwidth is another option. An example is use of the conformal strip width and shape as it was shown in section 4.5. Use of the external matching networks is not desirable since they require additional real-estate and increase the insertion losses, which as a consequence degrade the radiation efficiency of the antenna.

5.1.3 DR loading and hybrid DRA

Based on [27], loading a resonator can provide a modest bandwidth improvement, however, there may be degradations to the radiation pattern, increased cross-polarisation levels and radiation symmetry distortions. An advantage is that the DR size increase is usually minimal. The basic idea behind the DR loading is to introduce such boundary conditions that would add resonances or broaden the existing ones. The described concepts are based on DR shape modifications, such as added notches, microstrip patch loading, ground plane apertures and metallic strips.

The concept of hybrid DRA is found frequently in the literature, however, a theoretical coverage of that subject is absent in the textbooks. Frequently, the term *DR loading* is used interchangeably with the term *hybrid DRA*. Although the impact in both cases is similar, a hybrid concept may involve other antenna additions but DR loading. An example is use of a meandered slot ring in the antenna ground plane in [46]. It is also important to note that the hybrid DRA is the only bandwidth enhancement technique that allows improvements beyond the DR theoretic limits.

In section C.2.2 it was demonstrated that an antenna fed using width optimised conformal strips shows a secondary resonance and significantly wider

bandwidth comparing to an antenna fed using the thin wire probes and unoptimized strips. In that case the strips were acting as a DR load and modifying its boundary conditions.

5.1.4 Use of multiple resonators

Combining multiple resonators in both stacked and coplanar configurations is another of the bandwidth enhancement techniques. However, for this work is not considered due to a potential significant total antenna size increase.

5.1.5 DR and engineered surfaces

Use of the engineered surfaces such as the Electromagnetic Band Gap (EBG) structures to improve various antenna designs is well covered in the literature [54, 55, 56]. However, use of EBG in a combination with DRA is not common based on the reviewed literature. For this work, several concepts to employ EBG were investigated including DR loading, impedance matching and the antenna ground plane shaping. Loading a DR using EBG structures makes a considerable part of this chapter as will be shown in section 5.3.

Use of an EBG based structure to replace the back-cavity of a hDRA antenna in [46] was proposed in [57]. It was hypothesized that a thin EBG based back-plane could be designed to replace the back-cavity. A concept of an artificial back-plane was developed based on a two-dimensional (2D) EBG cell array. An in-depth investigation was conducted, however, the results were unsatisfactory.

5.2 Annular DR

The concept of an annular or ring DR is well covered in [28, pp. 91-96]. A ring is formed by removing a cylindrical section of radius b of the central portion of the resonator, see Figure 5.1. Removing the central portion results in lowering of the effective dielectric constant, which lowers Q_{rad} , hence increasing the bandwidth. For the $TM_{01\delta}$ mode a two to three-fold DR diameter increase is required to achieve 3 to 14 times Q_{rad} reduction due to a resonant frequency increase [28, pp.128-129]. This is due to effective dielectric constant and r/h ratio changes.

The literature only discusses the $TM_{01\delta}$ mode resonant antennas based on an annular DR, which radiate like a short vertical electric monopole. The

best example is in [47], where an ultra wideband response exceeding 3:1 was demonstrated. Existence of the $HE_{11\delta}$ mode in an annular DR is not confirmed in the literature. It is a different structure and there is no evidence that it supports the same resonant modes to those of the cylindrical DR.

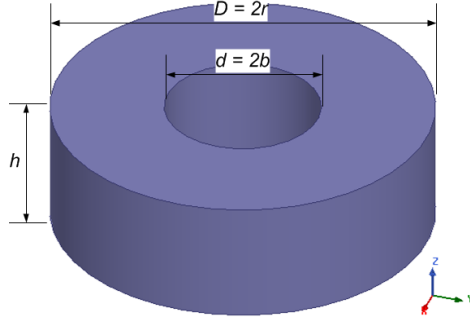


Figure 5.1: Annular dielectric resonator.

A hypothesis is made that the $HE_{11\delta}$ mode is likely to exist for higher r/b ratios (i.e. when less material is removed). This is possible since for a small radius b , the annulus is likely only to reduce ϵ_{eff} and allow perseverance of the $HE_{11\delta}$ mode fields. A probe located in the center of a DR, as shown in Figure 3.17.b, excites the $TM_{01\delta}$ mode, whereas feeding a DR closer to the outer diameter will excite the $HE_{11\delta}$ mode as in case of a solid cylinder. Thus, exciting the $HE_{11\delta}$ mode should be a simple exercise.

5.2.1 Design of annular DR for $HE_{11\delta}$ mode

To confirm the above hypothesis the first step was to develop a basic mathematical tool as a starting point. The only design equations available are for the $TM_{01\delta}$ mode in [28, pp.91-97]. Eq. 5.1 gives a resonant frequency f_0 where c is the speed of light and X_0 is given by eq. 5.2. Eq. 5.2 is a numerical solution of the first order Bessel functions of the first and second kind J_1 and Y_1 , respectively, see eq. 5.3.

$$f_0 = \frac{c}{2\pi\sqrt{\epsilon_r}} \sqrt{\left(\frac{\pi}{2h}\right)^2 + \left(\frac{X_0}{r}\right)^2} \quad (5.1)$$

$$X_0 = 3.56 + 5.13 \left(\frac{b}{r}\right) - 13.07 \left(\frac{b}{r}\right)^2 + 28.2 \left(\frac{b}{r}\right)^3 \quad (5.2)$$

$$\frac{J_1(X_0)}{Y_1(X_0)} = \frac{J_1(\frac{b}{r}X_0)}{Y_1(\frac{b}{r}X_0)} \quad (5.3)$$

In the next step the resonant frequency ratios for $HE_{11\delta}$ and $TM_{01\delta}$ modes as a function of r/h ratio were estimated from the experimentally obtained data in Figure 4.14. Figure 5.2 shows the $HE_{11\delta}$ and $TM_{01\delta}$ modes resonant frequency ratio $f_{0_{HE11}}/f_{0_{TM01}}$ vs. the r/h ratio. Using a polynomial fit on the $f_{0_{HE11}}/f_{0_{TM01}}$ ratio data points from Figure 5.2 gives eq. 5.4. Solving eq. 5.1 and eq. 5.4 for a given r/h allows estimation of the resonant frequency of an $HE_{11\delta}$ mode resonant annular DR.

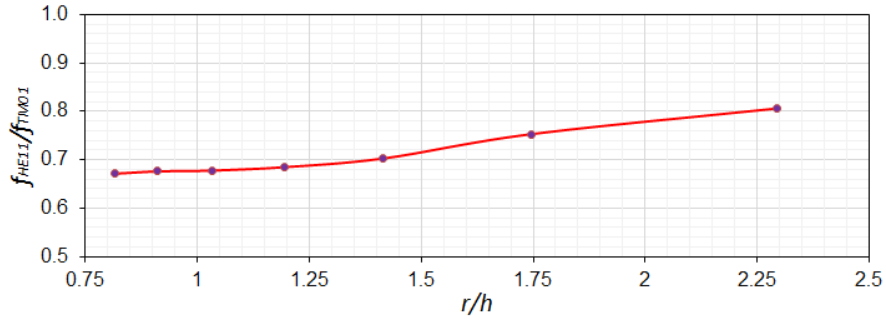


Figure 5.2: $HE_{11\delta}$ and $TM_{01\delta}$ modes resonant frequency $f_{0_{HE11}}/f_{0_{TM01}}$ ratio vs. r/h ratio.

$$f_{0_{HE11}} = f_{0_{TM01}} \left(0.8755 - 0.508 \frac{r}{h} + 0.3823 \left(\frac{r}{h} \right)^2 - 0.0758 \left(\frac{r}{h} \right)^3 \right) \quad (5.4)$$

The presented method makes a broad assumption that the $f_{0_{HE11}}/f_{0_{TM01}}$ ratio follows the same pattern for both the solid cylinder and annular DR. In addition, the method is possibly valid only for r/h in a range between $0.8 \leq r/h \leq 2.3$ (the range of available r/h data). Although, there is no way to easily verify the accuracy of this method, it is the only available in this case.

Based on the procedure described above, dimensions for $\epsilon_r = 12$ DR resonant at 1385 MHz were found as $r = 36$ mm, $h = 27.3$ mm and $b = 12.75$ mm. This design was then optimised using the HFSS optimization tool. The DR dimensions converged at $r = 34.3$ mm, $h = 23.59$ mm and $b = 10.46$ mm for r/h and b/r ratios of 1.454 and 0.305, respectively. An impedance

matching network described in section 5.5.1 was used as well. The responses of the DRA are shown in Figure 5.3 whereas Figure 5.4 shows the equatorial plane H -fields at 1.23, 1.35 and 1.58 GHz. The DR appears to be resonant at 1.35 GHz, which is below the design (1385 MHz).

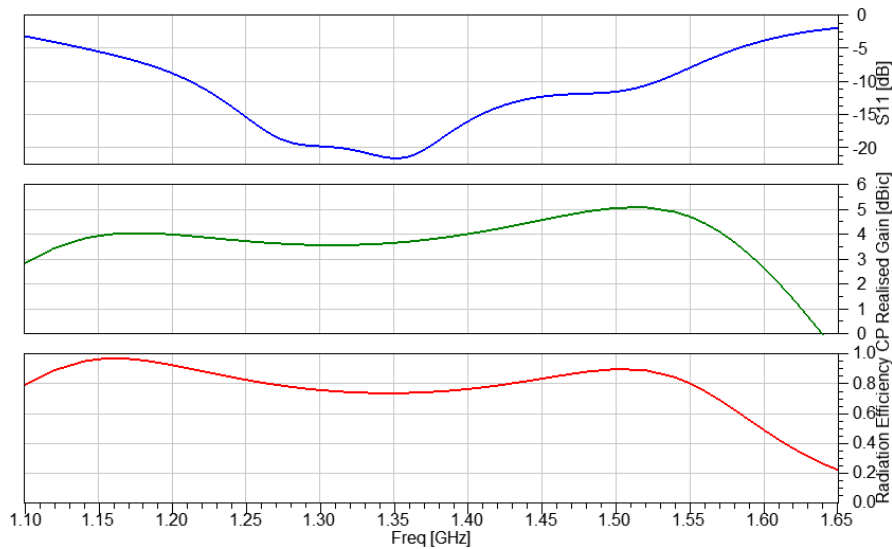


Figure 5.3: Unloaded annular DR S_{11} , realised gain and η_{ant} .

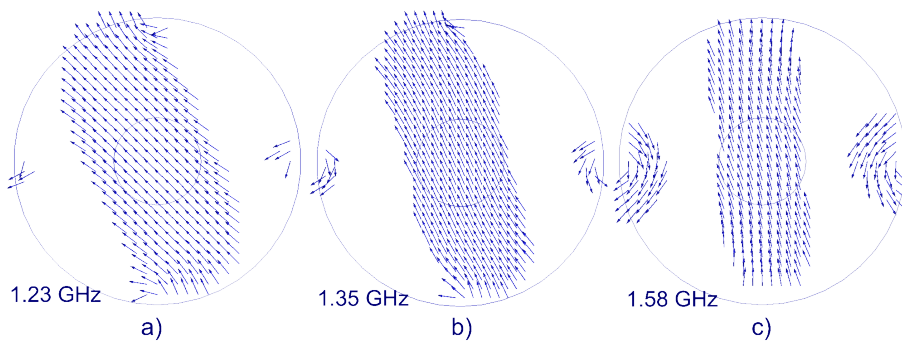


Figure 5.4: Annular DR equatorial plane H -field: a) 1.230 GHz, b) 1.35 GHz - resonant frequency and c) 1.58 GHz.

The results confirm the hypothesis that the $HE_{11\delta}$ mode can be excited in an annular DR. However, the antenna shows no bandwidth improvements comparing to the antennas using a solid cylinder DR of similar dimensions

and ratios, see sections C.1 and C.2.2. Therefore, use of an annular did not provide any significant bandwidth improvements, however, the antenna based on the annular DR is 0.8 mm (3.3%) shorter comparing to the solid cylinder DR (section C.2.2).

The exercise shows that an annular DR can be an alternative to the cylindrical DR while potentially offering minor improvements. In particular, the annular DR has a lower profile. Table 5.1 provides dimensions of the annular and cylindrical DRA parameters used in this investigation. The cylindrical DRA parameters from the antenna in section C.2.2.

Table 5.1: Annular and cylindrical DR and antenna dimensions.

Parameter	Annular DR [mm]	Cylind. DR [mm]	Description
b	10.46	-	DR inner radius
h	23.59	24.40	DR height
r	34.30	30.80	DR radius
r/h	1.454	1.263	DR radius to height ratio
r_{GP}	45.00	45.00	Ground plane radius
w_{es}	2.10	2.10	Excitation strip width
ε_r	12	10	DR dielectric constant

5.2.2 Loaded annular DR

In this section a loaded annular DR is investigated. In [28, pp. 97-98 and 157-159] a $TM_{01\delta}$ mode resonant annular ring DR loaded with a solid grounded post is described. The reference provides similar methodology as in case of the unloaded annular DR covered in section 5.2.1. It is stated that a grounded post modifies the DR internal fields forcing the $TM_{01\delta}$ mode to be lowest mode, hence effectively reducing the size of a DR.

Existence of the $HE_{11\delta}$ mode in an annular DR loaded with a solid grounded post is not mentioned in the literature. The initial reaction to this concept was negative considering that the $HE_{11\delta}$ mode fields have the highest intensity at the DR core [16], hence, presence of a grounded post was counter intuitive. However, after a closer inspection it appeared that presence of a ground plane at the core would allow the $HE_{11\delta}$ mode E -field lines to terminate perpendicularly, therefore allowing the mode to exist. Thus, a hypothesis was made again that an annular DR with a grounded core could effectively reduce the DR size

and lower Q_{rad} , as described in [28, pp. 97-98 and 157-159] for the $TM_{01\delta}$ mode. In addition, it was believed that a termination of the E -field lines at the core would reduce the mutual coupling between the opposing ports, which was found to be an issue with the solid cylinder DR.

Different forms and variations of an annular ring core loading were investigated. The first step was to investigate DR responses to a solid post and its variations. Figure 5.5 shows six grounded electrically conductive loads and their corresponding surface currents J_{sur} at 1585 MHz: a) solid post, b) hollow cylinder, c) hollow cylinder with 4 vertical cuts, d) hollow cylinder with 8 vertical cuts, e) hollow cylinder with 16 vertical cuts and f) dual-row interleaved wedge-like periodic structure. All loads were used on the same DR described earlier in section 5.2.

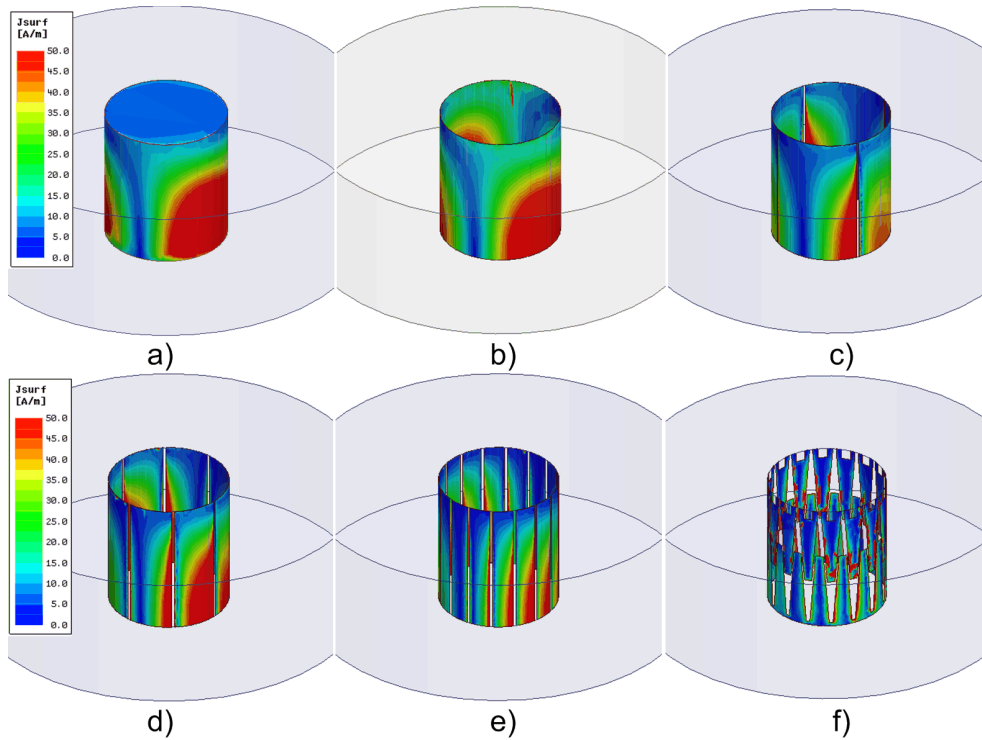


Figure 5.5: Annular ring DR loading and corresponding surface currents at 1585 MHz: a) solid post, b) hollow cylinder, c) hollow cylinder with 4 vertical cuts, d) hollow cylinder with 8 vertical cuts, e) hollow cylinder with 16 vertical cuts and f) dual-row interleaved wedge-like periodic structure.

Figure 5.6 shows that all of the loads show two distinctive pass-bands whereas total combined BW is significantly smaller compared to a cylinder and annular DR (Figure C.3 and 5.3). Radiation efficiency and antenna realised gain at the zenith are lower comparing to an unloaded DR. There is no notable differences between the hollow cylinder and solid post loading (Figure 5.5.a-b), including the surface current density J_{sur} . Adding vertical cuts to the hollow cylinder adds a stop-band within the lower pass-band. The stop-band frequency is affected by the number of cuts.

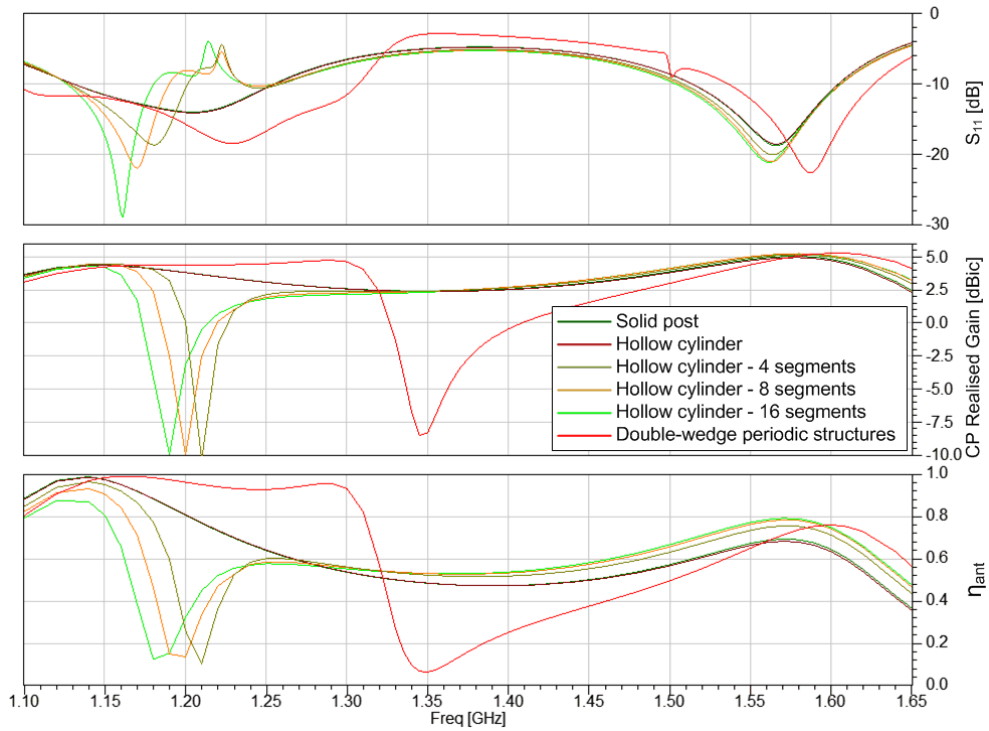


Figure 5.6: Antenna S_{11} , realised gain and η_{ant} for various annular DR core loads.

5.3 Periodic structure loaded annular DR

Use of the periodic structures as an annular DR load is a novel concept. This concept was developed and validated from empirical observations of the surface currents J_{sur} on a grounded cylinder and its variations described in section 5.2.2 (Figure 5.5.a-e). Based on surface currents density it is obvious

that there is a strong interaction between the DR and the load surfaces due to termination of the perpendicular E -field lines. Ability to control the terminations of the E -field lines is the primary objective. Such properties could be achieved using the engineered surfaces such as the EBG structures.

The first step was to add an N number of vertical cuts to the grounded cylinder, where $N = n4$ and $n = 1, 2, 4, \dots$. Based on the S_{11} response (Figure 5.6) the cuts added an additional resonance in the lower pass-band between 1150 and 1250 MHz. The added resonance creates a narrow stop-band at an offset frequency (see η_{ant} and G_r) and increasing the number of cuts appear to shift the resonance towards the lower frequencies. The radiation efficiency η_{ant} shows minor improvements but only in the upper band.

This exercise verified the original hypothesis that the $HE_{11\delta}$ mode can exist. However, the performance is unsatisfactory. Presence of a stop-band is an interesting and desirable antenna feature, however, it is not clear at this stage which parameter controls the stop-band frequency.

5.3.1 Periodic structure design

It was shown above that simple vertical cuts evenly spaced around the DR loading cylinder appear to alter the antenna response. However, simple vertical cuts do not provide sufficient design flexibility to allow exploitation of the observed features. In addition, varying the number of cuts from 4 to 16 does not appear to significantly impact the antenna response.

To make the length of the vertical cuts a variable, the cuts were made with a slant angle α and to eliminate a potential impact on the antenna dual-sense CP performance, a symmetrical cut is added as well. This creates a pattern of two rows of interleaved wedge-like periodic structures, see Figure 5.7. The lower row is grounded while it is capacitively coupled to the upper row through a gap width w_1 . In addition, the height of both the upper and lower wedges, h_1 and h_2 , respectively, can be also varied.

The upper row wedge-to-wedge coupling is controlled through a gap width w_2 . Adding a notch of height h_3 and width w_3 on top of each upper row wedge created a delay to the currents coupled between the upper row wedges. To reduce the impact on the coupling between the upper row wedges due to the other dimensional changes, a narrow rim is added at the top of the structure. Since the rim width w_4 is independent of other dimensions, it allows w_2 to be

independent as well. The same approach was made for the lower wedge row at the ground plane level. To keep the gap width w_5 independent of other changes a rim of width w_6 is added. Figure 5.7 shows the new DR loading structure in more details. The loading structure added design variables and their dimensions are summarized in Table 5.2.

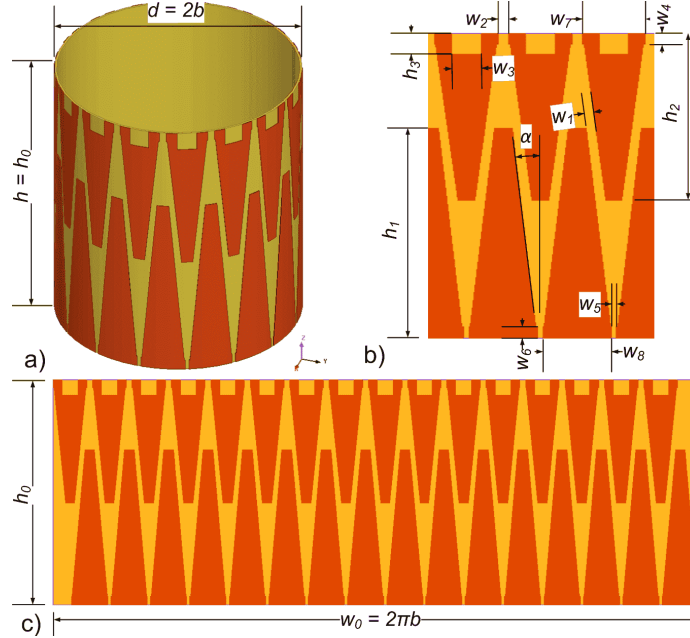


Figure 5.7: Dual-row interleaved wedge-like periodic structure as annular DR load: a) structure wrapped around DR air-core, b) structure detail and c) structure unwrapped.

The number of new design variables is significant and steps were made to eliminate fixed, redundant and low impact variables. Very early in the design process it was found that an optimum structure height h_0 is the same as the DR height h . Also, the unwrapped structure width w_0 is equal to the circumference of the DR core, which is obvious. The angle α is found to be redundant since it is primarily determined by the gaps between the upper and lower rows wedges, w_2 and w_5 , respectively, and wedge heights h_1 and h_2 .

The loading structure consists of two sets of 16 wedge-like elements in the upper and lower rows. The two rows are interleaved. Considering the arrangement between the loading structure surfaces and the resonator, it is

Table 5.2: Loading structure parameters, dimensions and descriptions.

Variable	[mm]	Description
α	-	Cut slant angle
h_0	h	Hight of the DR (Table 5.1)
h_1	16.30	Hight of lower row wedges
h_2	12.86	Hight of upper row wedges
h_3	1.60	Notch hight on the upper row wedges
w_0	65.72	Unwrapped structure width, $w_0 = 2\pi b$
w_1	0.50	Gap width between the upper and lower row wedges
w_2	0.58	Gap width between the upper row wedges
w_3	1.64	Notch width on the upper row wedges
w_4	0.83	Upper row rim width
w_5	0.31	Lower row wedges gap width at the ground plane
w_6	0.90	Lower row rim width
w_7	3.53	Upper row wedge width, $w_7 = (w_0/16) - w_2$
w_8	3.80	Lower row wedge width, $w_8 = (w_0/16) - w_5$

anticipated that terminations of the E -field lines induce the surface currents on the periodic structures. Thus the lower row elements act as an extension of the ground plane. The upper row elements are only capacitively coupled through the edges to the lower row elements, where each is connected to the ground plane. A capacitive coupling between the upper row structures is also maintained over the gap w_2 .

There are two possibilities: The loading structure acts only as an extension of the ground plane and, the loading structure acts like an EBG structure. If the loading structure acts only as an extension of the ground plane then there should be no difference between a solid cylinder and this complex structure. In fact, a solid cylinder would be the most effective extension the ground plane. However, if the loading structure acts like an EBG structure then it should demonstrate a distinctive pass or stop band. This will be investigated next.

5.3.2 Loading structure and EBG

The loading structure obviously needs to be conformal to the inner surfaces of the DR, hence forming a circular network of identical periodic elements. Identical periodic and possibly interacting elements in a circular configuration form an infinite-size circuit and possibly resonant. Based on the definitions

by *Yang et al* in [56, pp. 2-13] such a network can be best described as a one-dimensional (1D) uni-planar engineered surface or the Electromagnetic Band Gap (EBG) structure. References [54, 56] provide a variety of analytical approaches for design of EBG, however, all of them exclusively cover symmetrical structures on planar surfaces.

For a structure to perform as EBG it needs to meet eq. 5.5 condition for both planar and surface wave propagation conditions [56]. In eq. 5.5 l is the electrical length of an element and λ_g is the guided wavelength. In this case at 1380 MHz, which is the DR resonant frequency, $\lambda_g \approx 62.53 \text{ mm}$. Thus the height of the upper row wedges h_2 is about $0.2\lambda_g$ (Table 5.2). The reference does not provide an explanation for eq. 5.5 condition but it does provide evidence that elements meeting the condition perform better. In [56, pp.88] it is shown that $0.2\lambda_g$ would still generate an EBG response however of a narrower BW comparing to $0.1\lambda_g$.

$$l < \frac{\lambda_g}{10} \quad (5.5)$$

Therefore, to validate the hypothesis that the loading structure acts like an EBG, presence of a resonance frequency affecting only the structure needs to be shown. In addition, it needs to be shown that the resonant frequency f_r of the loading structure is dimension dependent.

5.3.3 DR radiation modes

In this section the loaded DR internal fields are examined. Figure 5.8.a-c shows the dominant H -field patterns in the equatorial plane at 5% DR height above the ground plane. The field patterns are shown for 1230, 1350 and 1580 MHz, which represent the resonant frequencies of the lower pass-band, the stop-band and the upper pass-band. Based on the field patterns, the DR appears resonates in the $HE_{11\delta}$ mode in both pass bands, see Figure 5.8.a and b. The $HE_{11\delta}$ mode H -field lines appear more disturbed comparing to the unloaded case in Figure 5.4. The dominant H -field pattern at the stop-band is shown in Figure 5.8.b. This field pattern does not match any of the modes defined in the literature. The radiation efficiency of the added resonance at 1580 MHz is lower relative to the primary resonance despite the fact that RL exceeds 15 dB in that band.

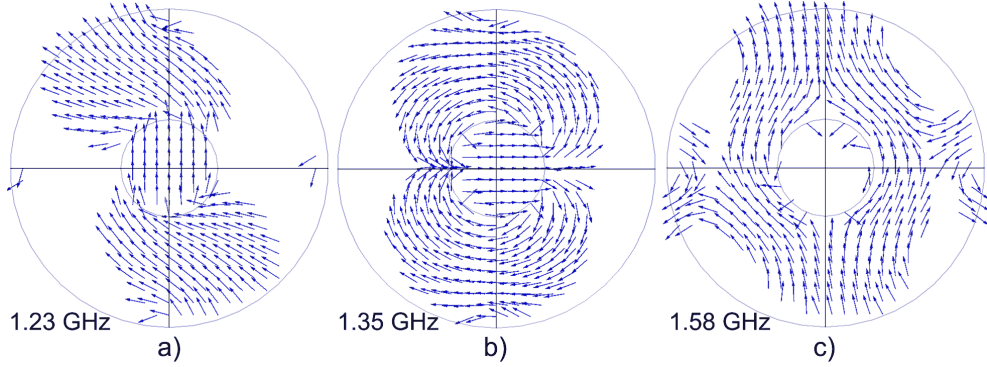


Figure 5.8: Loaded DR equatorial plane H -field patterns: a) 1230 MHz - lower pass-band, b) 1350 MHz - stop band and c) 1580 MHz - upper pass-band.

5.3.4 Loading structure resonance

There are two significant observations around 1350 MHz: First is the radiation mode change (Figure 5.8) and a radiation stop-band (Figure 5.11). Based on the H -field lines at 1350 MHz and using right-hand rule indicates that the E -field lines are terminating at the opposing sides of the core. This is confirmed based on the surface current density J_{sur} , see Figure 5.9. The highest density is observed at 1.355 GHz (Figure 5.9.a), which appears to be the loading structure resonant frequency f_r . The lowest density is observed at 1.23 and 1.585 GHz (Figure 5.9.b), or antenna's lower and upper pass-band resonant frequencies, respectively. Therefore, terminations of the E -field lines is only strong around stop-band. Another interesting observation is that the fields within the loading core appear to be 90° out-of-phase at 1.23 GHz, in-phase at 1.3 GHz and non-existent at 1.58 GHz.

5.3.5 Loading structure response control

Existence of the loading structure resonant frequency confirms that it is likely acting like a resonant circuit with properties similar to an EBG structure. To further confirm this claim structure's response to dimension variations is investigated. Considering that the possible capacitive coupling between the upper and lower structures exists and it can affect structure response, variables affecting the coupling will be varied. Three variables are of a primary interest: Height of the lower wedge h_1 , height of the upper wedge h_2 and the gap width w_1 between the wedges.

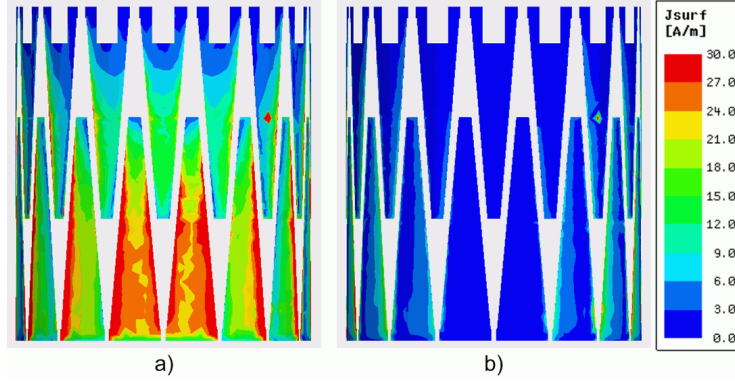


Figure 5.9: Loading structure surface current density: a) 1355 MHz - antenna stop-band, and b) 1240 MHz - antenna lower band resonant frequency.

Figure 5.10 shows the impact of h_1 variation on antenna's response. For the $15.8 \leq h_1 \leq 16.8$ mm range the stop-band shifts between 1330 and 1370 MHz mostly showing a linear response as shown in Figure 5.11. For the entire h_1 range the antenna maintains a similar dual-band response showing a minor impact on the upper and lower resonant frequencies. This might further confirm an existence the loading structure resonant frequency that induces the stop-band. In addition, it demonstrates that the loading structure has a controllable and dimension dependent response.

5.4 Antenna simulated response with the loading structure

The antenna displays distinctively different responses with and without the loading structure, see Figure 5.12. The structure affects the impedance bandwidth, mutual coupling between the feeding ports and provides a narrow band-stop radiation suppression. Without the loading structure the antenna acts as a broadband whereas with the loading structure it acts as a dual band antenna. With the loading structure, the lower band covers from 1.1 to 1.31 GHz and while the upper band covers from 1.54 to 1.62 GHz for a total of 290 MHz bandwidth or about 21%, see Figure 5.12. Both bands exceed the impedance bandwidth requirements of a GNSS antenna. The difference in the total bandwidth comparing to an unloaded annular DR is not significant (i.e. 290 MHz vs. 300 MHz), however, antenna functionality is entirely different.

5.4. Antenna simulated response with the loading structure

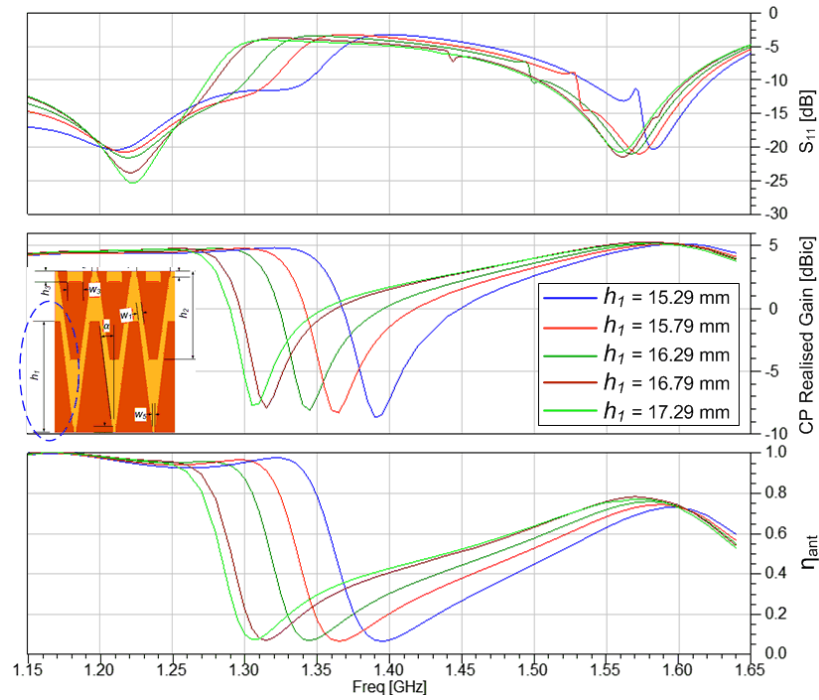


Figure 5.10: Antenna response to loading structure h_1 variations.

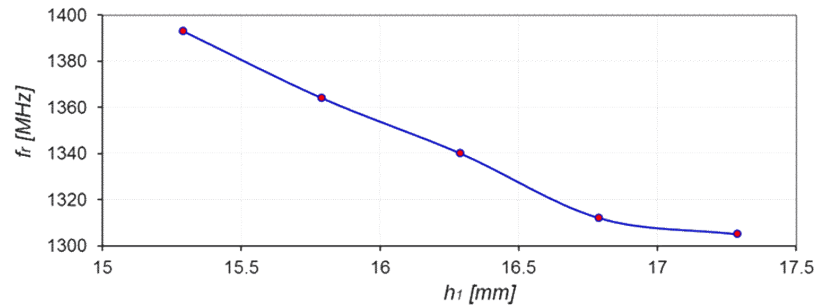


Figure 5.11: Stop-band frequency vs. loading structure h_1 .

The periodic structure load clearly improves antenna impedance bandwidth, minimum gain bandwidth and radiation efficiency over both the upper and lower GNSS bands. The peak radiation efficiency in the upper GNSS band is lower comparing to the lower band and the unloaded annular DR, see Figure 5.12. The loading structure inserts a narrow radiation suppression

5.4. Antenna simulated response with the loading structure

band around 1.355 GHz, similar to a stop-band filter. The 10 dB radiation suppression (i.e. 4.5 to -5.5 dBic) is demonstrated between 1.34 and 1.37 GHz.

As earlier indicated, the loading structure shows controllable and dimension dependent response. Hence, the stop band resonant frequency is controllable through the loading structure. It is most sensitive to the lengths of the lower and upper wedges h_1 and h_2 , respectively, and the gap width w_1 between the upper and lower row wedges, see Figure 5.11.

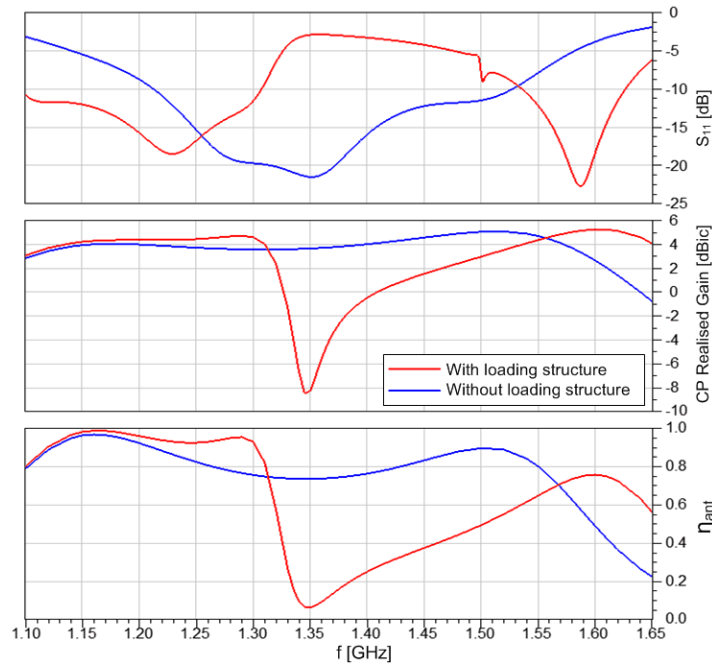


Figure 5.12: Loading structure impact on antenna S_{11} and realised gain responses.

5.4.1 Realised gain, radiation pattern and AR

Figure 5.13 shows antenna's RHCP realised gain G_r beamwidth at $f=1.16, 1.24, 1.3$ and 1.58 GHz. Antenna shows $G_r \geq 0$ dBic beam width between 120° at 1.58 GHz and 144° at 1.3 GHz. These results can not be directly compared with the unloaded DR since 1.16 and 1.58 GHz frequencies are outside of 10 dB RL BW. At 1.3 GHz loaded DR has about 12° broader beamwidth. It is not clear if that is a result of different radiation pattern or higher radiation

5.4. Antenna simulated response with the loading structure

efficiency, hence higher G_r .

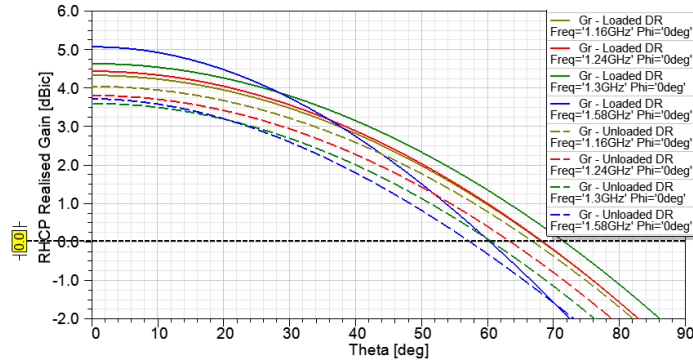


Figure 5.13: Antenna RHCP realised gain beamwidth.

Figure 5.14 shows loaded DR RHCP (co-polarisation) and LHCP (cross-polarisation) vertical plane radiation patterns at $f=1.16, 1.3$ and 1.58 GHz and $\phi=0^\circ$. The LHCP (cross-polarisation) below $\theta=90^\circ$ indicates antenna's susceptibility to the single-bounce multipath signal. At $\theta=180^\circ$ (Nadir) and 1.16 GHz this antenna has LHCP $G_r = -1$ dBic, which could be significant. However, the back lobe LHCP radiation in this case is heavily affected by the ground plane size. There are no elements in this case that could be attributed to the loading structure.

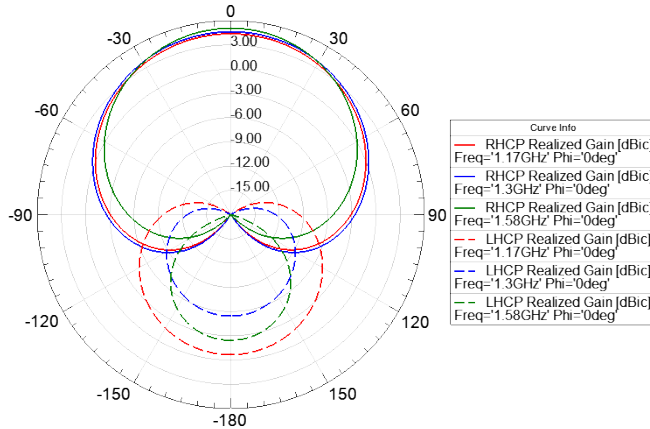


Figure 5.14: Loaded DR RHCP (co-polarisation) and LHCP (cross-polarisation) radiation patterns.

5.4. Antenna simulated response with the loading structure

The AR BW and beamwidth are shown in Figure 5.15 and 5.16. In both loaded and unloaded cases AR responses from 1.15 to 1.3 GHz and from 1.5 to 1.65 GHz are very similar. An exception is between 1.3 to 1.4 GHz where loaded DR shows a distinctive stop-band response, which is this case manifested as AR degradation. Figure 5.15 also shows that the antenna shows $AR < 3$ dB BW of over 36% even at $\theta=60^\circ$. AR beamwidth (Figure 5.16) at 1.16, 1.24, 1.3 and 1.58 GHz does not appear to be affected by the DR loading. The $AR < 3$ dB beamwidth ranges between 130° at 1.16 GHz and over 180° at 1.58 GHz.

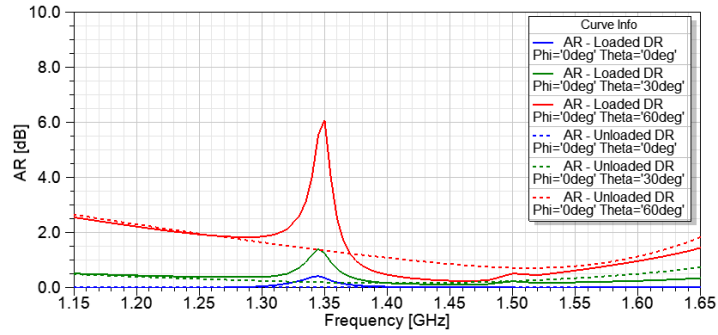


Figure 5.15: AR bandwidth for $\theta=0^\circ$, 30° and 60° .

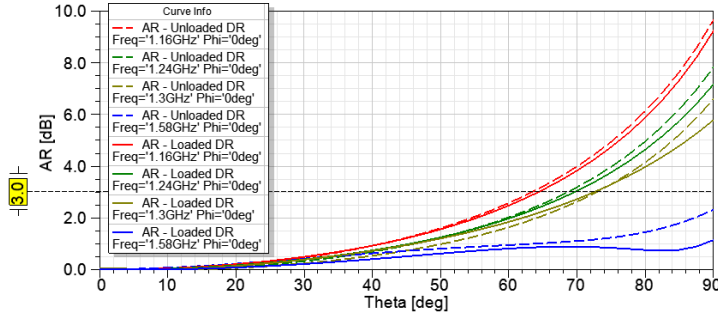


Figure 5.16: AR beamwidth at $f=1.16$, 1.24 , 1.3 and 1.58 GHz.

5.4.2 Feeding ports mutual coupling

With the loading structure, the mutual coupling between the opposite ports is reduced over the entire frequency range comparing to cylindrical and annular unloaded DRs (Figure 5.17). It ranges between -8.5 and -7.5 dB in the

upper band while it is below -15 dB in the lower band. The impact on the adjacent port coupling was, however, adverse especially in the upper band. Between 1.56 and 1.61 GHz, the coupling went from below -15 dB, without a load, to around -8 with a load. In the lower band the adjacent port coupling went from a -12.5 to -7.7 dB range, without the load, to a -7.2 to -6.9 dB range with the load. Table 5.3 summarizes the mutual coupling results for cylindrical, annular and annular loaded DRs. The values are based on Figure 5.17 and C.3.

The loading structure total impact on the mutual coupling is not obvious since the unloaded and cylindrical DRs do not have the same impedance bandwidth as the loaded DR. If the bandwidth differences are ignored, the suppression of the opposing port coupling (S_{31}) can be considered significant. Note that the loading structure was initially called “Decoupling Network” (DN), as a working name, because of the coupling suppression property [58].

The mutual coupling impact on the AR performance does not appear to be as severe as predicted in section 3.5.2. Based on Figure 3.24, the AR upper limit is 5 to 6 dB for an adjacent port mutual coupling of around -7 dB. However, the simulated $AR < 3$ dB beamwidth exceeds 130° over both pass-bands (Figure 5.17). A similar finding is described in section C.2.3.

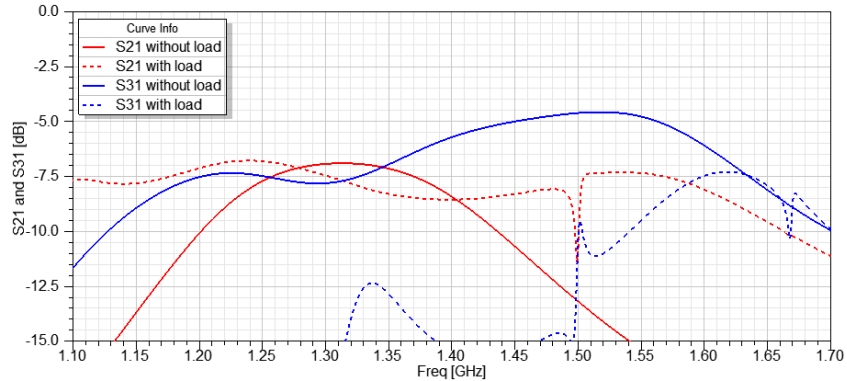


Figure 5.17: Loading structure impact on feeding port mutual coupling.

5.5 Antenna final design

The final antenna proposal is based on the loaded annular DR. The DR is specified in Table 5.1. It has a 34.3 mm radius and 23.59 mm height, which

Table 5.3: Cylindrical, annular and annular loaded DR feeding port mutual coupling.

f [MHz]	Cylinder DR		Annular Unl. DR		Annular Load. DR	
	Oppos. [dB]	Adjac. [dB]	Oppos. [dB]	Adjac. [dB]	Oppos. [dB]	Adjac. [dB]
1175	-9.0	<-15	-8.0	-11.7	<-15	-7.5
1225	-6.0	-10.7	-7.4	-8.5	<-15	-7.0
1300	-5.7	-9.5	-7.8	-6.9	<-15	-7.5
1580	-4.0	-14.0	-5.5	<-15	-8.0	-8.0

is 0.8 mm or about 3.3% less than the antenna based on a solid cylindrical DR in section C.2.2. However, the DR radius has increased by 2.5 mm for r/h ratio of 1.4540 comparing to 1.2629 for the cylindrical DR in section C.2.2. The inner DR core radius b is 10.46 mm. The antenna is based on the same $\epsilon_r = 12$ dielectric material. To improve the radiation symmetry the ground plane is in a circular shape of 45 mm radius, which is based on the thesis objectives. The ground plane substrate is 30 mil mm thick of $\epsilon_r = 10.2$.

The inner surface of the annular DR is loaded with an engineered surface based on the electromagnetic periodic structure, which was covered in section 5.3. The loading structure is wrapped around a low density foam core ($\epsilon_r = 1.08$) and inserted into the DR. The loading structure dimension are given in Table 5.7 and Figure 5.2. The DR is excited using 2.1 mm wide conformal strips. For fabrication simplicity, the strips are not tapered. The antenna uses an impedance matching network that is further covered in section 5.5.1.

To ensure a gap-less interface between DR and the ground plane, which was noted as a problem in the designs presented in [45, 46], the DR is affixed to the substrate and ground plane using four fasteners M3x0.5x30 made of polyester ($\epsilon_r = 3.2$). The fasteners are also used to align the DR with the excitation vias, which should simplify the assembly process.

Figure 5.18 shows an exploded view of the antenna assembly, whereas Figure 5.19 shows a layered view of the ground plane PCB. The PCB also includes mounting pads for the micro coaxial connectors (MCX) that will be required for antenna measurements. Due to the absence of the radiating slots, compared to the state of the art designs in [12, 45, 46], there is no need for a

back cavity. In addition, the entire area below the ground plane is available for the front-end circuitry.

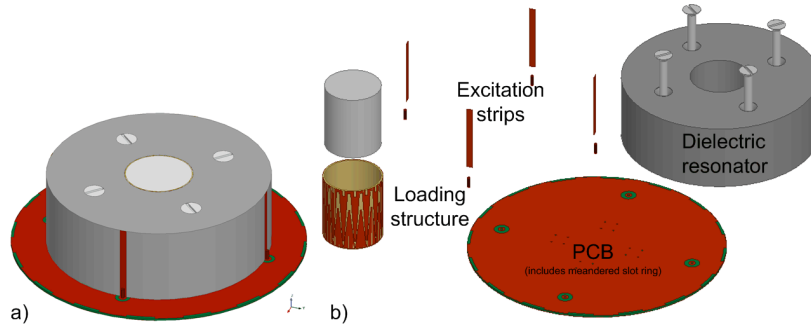


Figure 5.18: Loaded annular DRA: a) assembled view and b) exploded view.

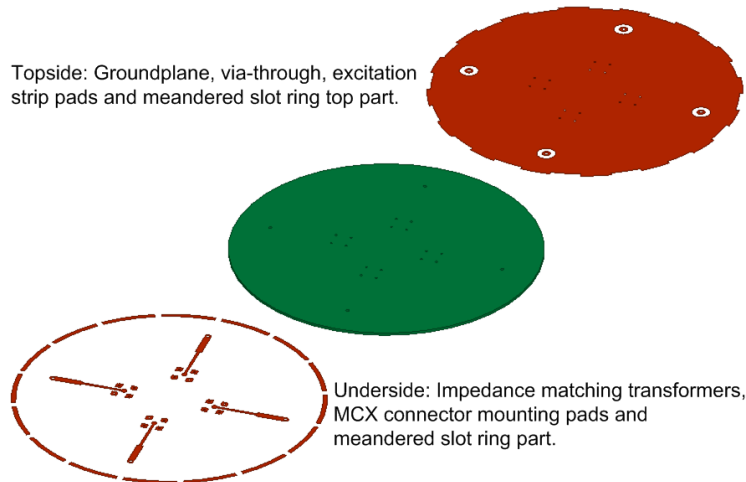


Figure 5.19: Ground plane PCB layered view.

5.5.1 Impedance matching

To improve the impedance matching a three-section short-step microstrip transformer is used. In addition, the diameter of the via-through pad d_{vp} and its ground plane clearance r_v are also used for impedance matching. This network plays a significant part in the antenna performance. It is interesting that a DR made of $\epsilon_r = 12$ material even without the loading structure is

highly dependent on an additional impedance matching for the $HE_{11\delta}$ mode. A similar finding has been mentioned in several references, including [16].

Figure 5.20 shows the underside view of the antenna PCB and the main elements of the impedance matching network: a three-section short-step microstrip transformer, excitation strip pad and coaxial via-through. The width of the conformal excitation strips is used in as well. Table 5.4 provides a list of the nomenclatures, dimensions and description of the impedance matching parameters.

Figure 5.21 shows the effects of the impedance matching network on the antenna S_{11} , radiation efficiency and realised gain responses. It is obvious that the impedance matching contributes significantly to the antenna performance especially in the upper band.

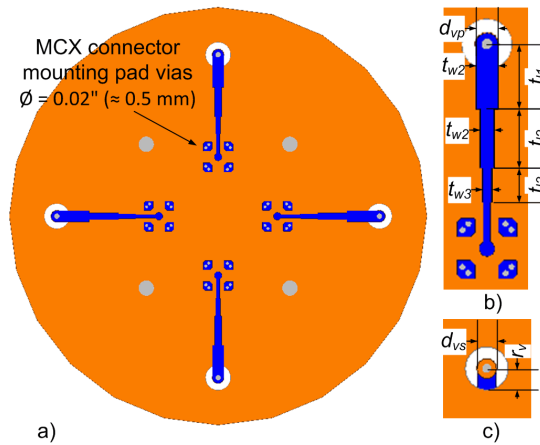


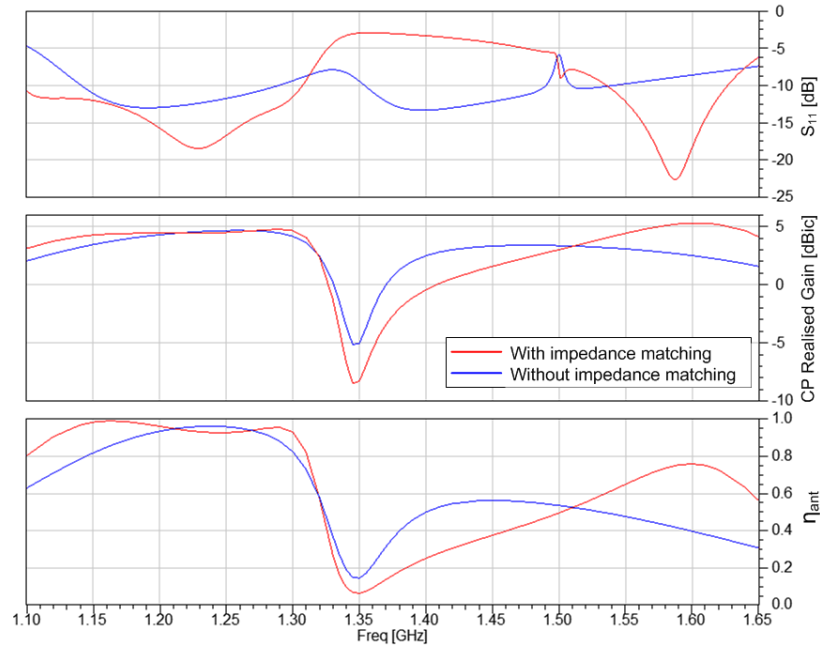
Figure 5.20: Impedance matching network parameters: a) antenna PCB underside view, b) three-section short-step impedance transformer and c) via-through and excitation strip pad.

5.6 Parametric analysis

To assess the antenna design sensitivity to the material variations, fabrication and assembly tolerances a parametric analysis was conducted. All of the dimension and dielectric constant dependent parameters were investigated. Fabrication specifications for DR machining and PCB etching were used. For

Table 5.4: Impedance matching network parameters, dimensions and descriptions.

Variable	[mm]	Description
t_{l1}	6.90	Impedance transformer section 1 length
t_{l2}	6.30	Impedance transformer section 2 length
t_{l3}	3.70	Impedance transformer section 3 length
t_{w1}	2.40	Impedance transformer section 1 width
t_{w2}	1.40	Impedance transformer section 2 width
t_{w3}	0.96	Impedance transformer section 3 width
d_{vp}	t_{w1}	Via-through pad diameter
d_{sp}	2.50	Excitation strip pad diameter
r_v	1.50	Coaxial ground plane clearance radius

Figure 5.21: Impedance matching network impact on antenna S_{11} , radiation efficiency and realised gain.

the dielectric constant dependent parameters material specifications provided by the manufactures were used.

The analysis showed that the impact of the dimension errors due to fabrication tolerances is not significant. In most cases the antenna retains its performance with a minor degradation. However, a cumulative effect from fabrication and assembly errors can not be excluded. Two most critical parameters were found to be the DR dielectric constant error and presence of an air-gap t_{ag} between the loading structure and DR core inner wall, see Figure 5.22. Such an air-gap t_{ag} can be formed as a result of the antenna fabrication or assembly process.

Figure 5.23 shows the effects of the dielectric constant 5% error ($11.4 \leq \epsilon_r \leq 12.6$) as specified by the manufacturer [59]. Based on the S_{11} response the lower resonance varies between $1200 \leq f_r \leq 1255$ MHz while the the upper resonance varies between $1540 \leq f_r \leq 1610$ MHz. The impact on the stop-band is similar, the resonance varies between $1320 \leq f_r \leq 1370$ MHz. Considering that the dielectric constant impact on λ_g is $1/\sqrt{\epsilon_r}$ the actual resonant frequency f_r should be within $\pm 2.5\%$ of the design resonant frequency f_{rd} . Therefore, the impact on the DR design resonant frequency should be $0.9747f_{rd} \leq f_r \leq 1.0247f_{rd}$ or $1350.4 \leq f_r \leq 1419.6$ MHz. The results from Figure 5.23 confirm that.

Impact of the air-gap t_{ag} was found to be the most critical. Figure 5.24 shows that a gap of only 50 μm would significantly degrade antenna performances in both bands. Thus fabrication and assembly of the loading structure and DR need to be considered with a significant attention to details.

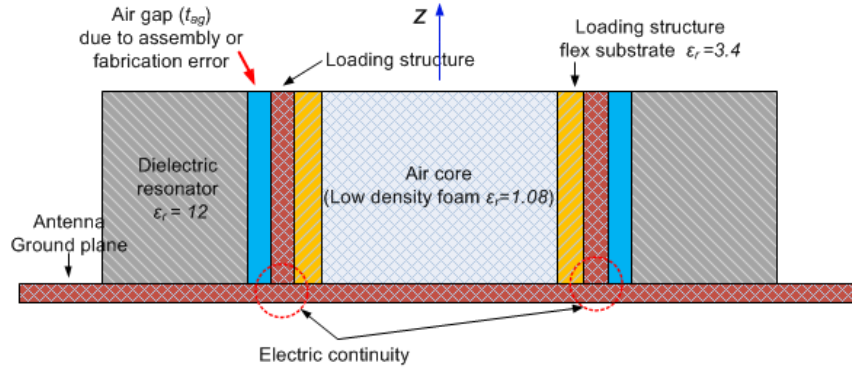


Figure 5.22: Antenna cross-section.

5.6. Parametric analysis

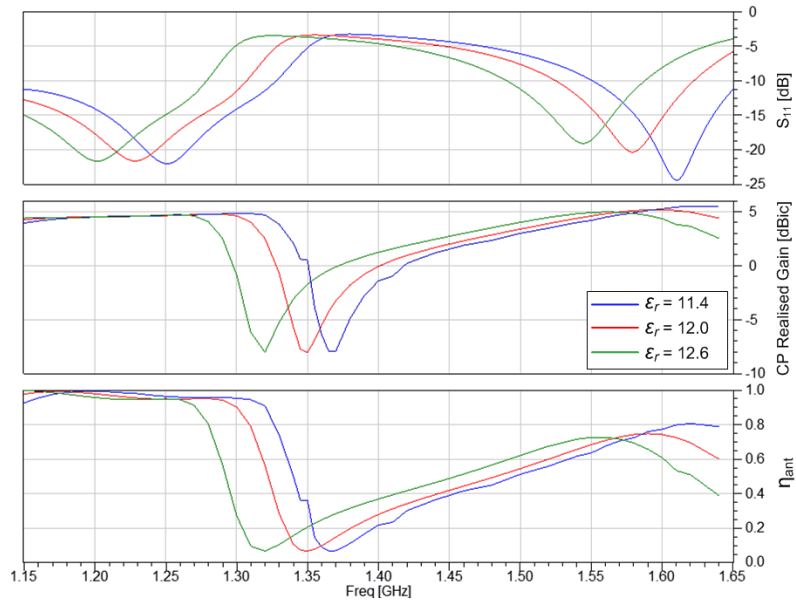


Figure 5.23: Effects of DR dielectric constant 5% error on antenna response.

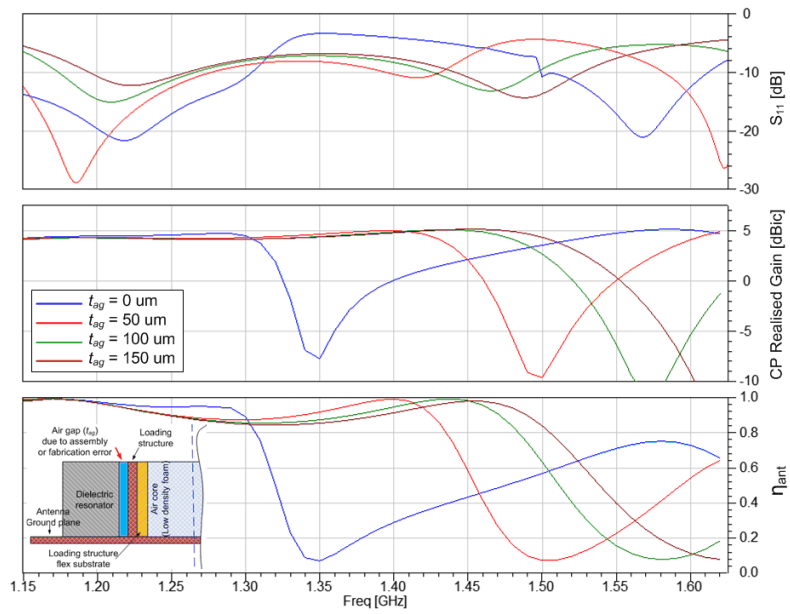


Figure 5.24: Effects of air-gap t_{ag} on antenna response.

5.7 Antenna fabrication

Antenna fabrication process consists of four main steps: DR machining, solid and flex PCB fabrication and assembling process. Each of the steps is described in the subsequent sections.

5.7.1 Dielectric resonator

The DR is fabricated from C-STOCK AK-12 made by Cuming Microwave [59]. It is a ceramic filled cross-linked plastic based material, which is more suitable for machining than the traditional ceramic only dielectric materials. The material has loss tangent below 0.002 and it is homogeneous and isotropic to within 5% for $\epsilon_r \leq 20$ [59]. Machining tolerances for DR are claimed to be +/- 0.15 mm or better.

The DR inner air core is made of low density, low dielectric constant ($\epsilon_r = 1.08$) and low loss structural foam similar to C-STOCK RH made by Cuming Microwave [60]. Pictures of a manufactured DR and its inner foam core are shown in Figure 5.25. The foam core function is to ensure tight and gapless fitting between the loading structures and DR. Considering significantly higher machining tolerances for the foam material, several foam core units were made in various diameters.

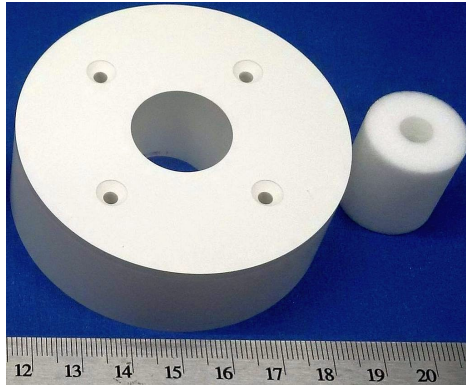


Figure 5.25: Fabricated DR with a low-density foam insert.

5.7.2 Ground plane PCB

The ground plane printed circuit board (PCB) is fabricated using Rogers AD1000™ substrate of dielectric constant $\epsilon_r = 10.2$, a dissipation factor $DF = 0.0023$ and dielectric thickness $h_{sub} = 30 \text{ mil}$ [61]. AD1000 is a substrate specifically designed for harsh environmental and exploitation conditions such as defense and aerospace applications. It is considered a high dielectric constant substrate made of a woven glass reinforced laminate, which allows dimensional stability, low thermal expansion, mechanical robustness and high tolerance to the vibrational stress.

Figure 5.26 shows a fabricated PCB with soldered surface mounted MCX coaxial connectors. It is fabricated using a standard chemical etching process whereas vias were plated using a plasma copper deposition process. Trace width fabrication tolerance is 3 mil or better.

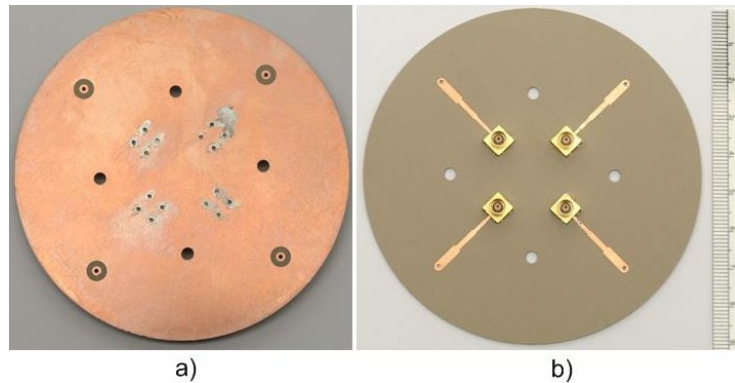


Figure 5.26: Fabricated PCB: a) top view and b) underside view.

5.7.3 Loading structure

The DR loading structure is a single layer one-sided engineered surface that requires a gap-less fit against the DR inner wall (Figure 5.18). It is fabricated as a single layer one-sided flexible printed circuit board (f-PCB). The f-PCB substrate is DuPont™ Pyralux® AP8565R polyimide film of $\epsilon_r = 3.4$, 6 mil thick and 18 μm ($0.5 \text{ oz}/\text{ft}^2$) metalization thickness [62]. It is fabricated using standard chemical etching technique. Figure 5.27 shows a sample of fabricated unwrapped loading structure.

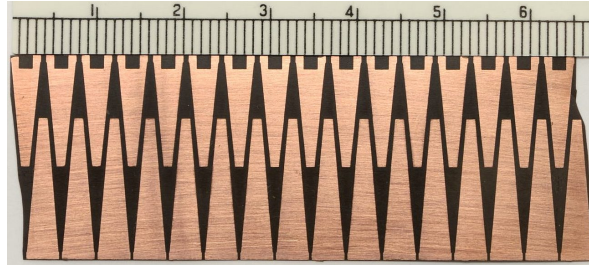


Figure 5.27: Fabricated loading structure unwrapped.

5.7.4 Antenna assembling

Assembling the DR and loading structure to the ground plane was a long manual process based a trial-and-error. An obvious solution was to solder the lower row wedges to the ground plane but that was not feasible for multiple reasons. The assembling order requires the DR to be first aligned with the ground plane and the excitation ports then secured to the PCB using four polyester fasteners. Then the loading structure can be inserted into the DRA. However, when this order is followed there is no access to the contact surfaces between the loading structure and the ground plane, see Figure 5.23.

A high conductivity silver based paste was used to ensure a electric contact between the loading structure and the ground plane instead of solder. The paste is a non-hardening component of the two-part high conductivity epoxy compound. This approach allowed a proper assembly order while at the same time it provided a flexible solution where antenna can be easily disassembled if required and the loading structure re-inserted. An important factor was that pressure can be applied on the loading structure flexible substrate once inserted into the cavity to ensure a gap-less fit. The 6 mil thick flexible substrate was found to be overly rigid and hard to press against the DR wall to ensure fully conformal fit. Significantly thinner substrate having also a thinner metalization layer should be considered for future work.

The excitation strips were fabricated from a copper foil. Copper was selected because of its high conductivity and natural softness, which provide a snug conformal fit. The strips were soldered directly to the via-through pads and held in place using DuPont™ Kapton® polyimide based adhesive tape of $\epsilon_r = 3.6$, again to ensure a gap-less contact. Figure 5.28.a shows the final antenna assembly whereas Figure 5.28.b shows the antenna top view with the

alignment markers as installed for measurements.

This design and assembly technique are influenced by the experience from the state-of-the-art designs described in [12, 44, 46]. All of those designs experienced issues with the air gaps between the ground plane and DR and DR alignment with the excitation ports. Although those designs used a different excitation technique and DR materials of $\epsilon_r = 30$, which both made antenna more susceptible to air-gaps than this design, it was still considered important.

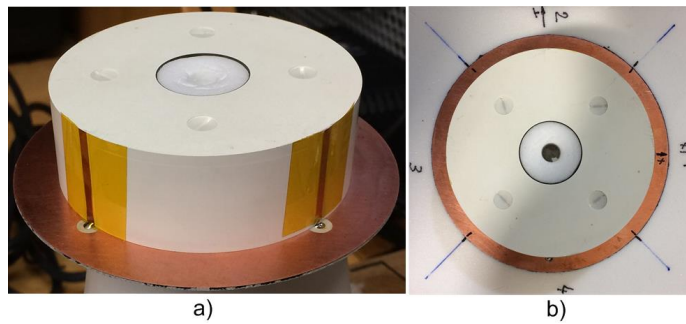


Figure 5.28: Assembled DRA: a) trimetric view and b) top view with antenna axes and port markings.

6 Experimental results

In this chapter antenna measurement results and analysis are presented. The chapter consists of 4 sections. Section 6.1 covers the antenna installation and alignment for radiation pattern measurements. The feeding circuit measurement results are provided in section 6.2 whereas the antenna S -parameter and radiation measurements are presented in section 6.3. An analysis of the results is given in section 6.4.

6.1 Antenna installation and alignment

The antenna was measured using a spherical near-field scanner (SNF) from Nearfield Systems Inc. (NSI) [63]. Spherical near-field measurements allow a complete characterization of an antenna-under-test (AUT). To perform the near-field measurements AUT is rotated in two axes (θ and ϕ) while a fixed probe measures the field data over the spherical surface. The near-field measurement data are then processed using NSI antenna measurement software NSI2000 to estimate the far-field parameters.

The scanner consists of a mechanism for positioning both AUT and probe and it is interfaced to a two-channel microwave vector network analyzer (VNA) [64]. It uses a dual axis ϕ/θ stepper motors to position AUT and it allows full spherical 360° ϕ/θ rotation with a resolution of 0.0125° in both axes [63].

6.1.1 Antenna installation

The antenna and its feeding circuit were first installed on a fixture made specifically for antennas of similar sizes. The fixture allows an antenna to be positioned at the center of the measurement sphere, or more precisely it allows the antenna's presumed phase center to be positioned at the center of the measurement sphere.

6.1. Antenna installation and alignment

After the antenna was installed on the fixture, it was then placed on the antenna positioner and connected to a coaxial cable, which is connected to the VNA through a coaxial rotary joint, see Figure 6.1. To minimize unwanted scattering around the AUT, the fixture was wrapped into two sheets of 12.7 mm thick radar absorbing material (RAM), which leaves only AUT and its ground plane exposed, see Figure 6.2.

The test probe used for these measurements was rectangular open-ended waveguide ANT-WGP-1.12-1.7 (WR-770) covering frequencies 1.12 - 1.7 GHz [65] (Figure 6.1).

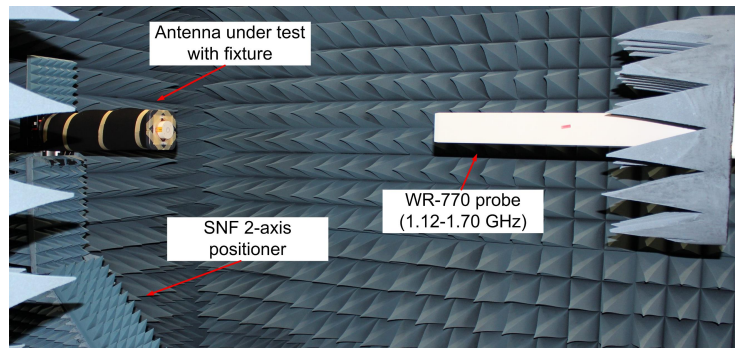


Figure 6.1: Measurement setup in NSI spherical near-field chamber.

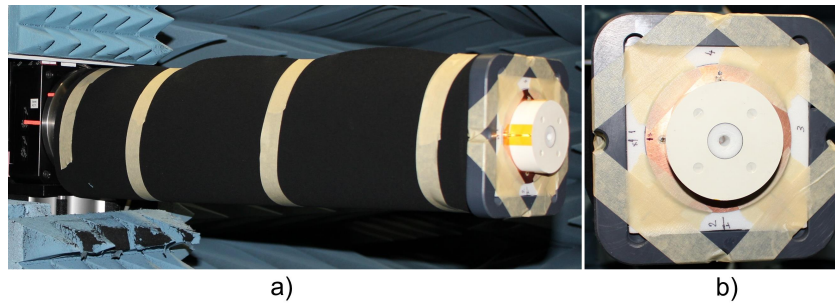


Figure 6.2: AUT ready for measurements: a) antenna on the RAM wrapped adapter and b) antenna front view at $\theta = 0^\circ$ and $\phi = 0^\circ$.

6.1.2 Antenna alignment

After the antenna was installed a scanner alignment was performed. The rectangular open-ended waveguide ANT-WGP-1.12-1.7 probe was aligned to the local horizontal plane to 0.05° accuracy then its positioner was re-indexed, which assumes the new established horizontal angle as the reference and resets the angle index to $\phi = 0^\circ$.

In the next step the antenna x-axis was also aligned to the local horizontal plane to match the probe alignment. The antenna positioner was then re-indexed, which set its newly established position angles to $\theta = 0^\circ$ and $\phi = 0^\circ$.



Figure 6.3: NSI ANT-WGP-1.12-1.7 probe alignment.

6.2 Antenna feeding circuit measurements

Figure 6.4 shows the feeding circuit measured S parameters. The feeding circuit input impedance (labeled as S_{55}) was measured while the 4 antenna ports were terminated using a $50\ \Omega$ matching terminations. The antenna ports were measured one at a time using VNA Port 2 while Port 1 was used to feed the circuit input. The unused antenna ports were terminated using matched terminations.

The feeding circuit input bandwidth (S_{55}) exceeds the required antenna impedance bandwidth, which is necessary. The antenna ports 1 and 3 (S_{11} and S_{33}) also exceed the antenna required input impedance. However, the antenna ports 2 and 4 (S_{22} and S_{44}) do not meet the 10 dB RL requirements in the upper band.

6.2. Antenna feeding circuit measurements

The antenna ports amplitude drop relative to the input port ranges from -6.5 to -7.5 dB, which gives 0.5 to 1.5 dB amplitude errors relative to the input port and up to 1 dB amplitude errors between the antenna ports, see Figure 6.4 and 6.5. The feeding circuit insertion loss (IL) is about 1.5 dB based only on the impedance measurements. Such performance was anticipated.

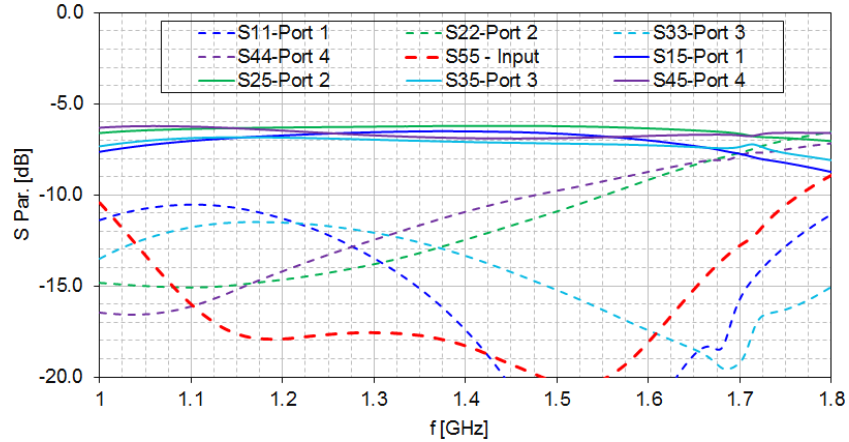


Figure 6.4: Antenna feeding circuit measured S -parameters.

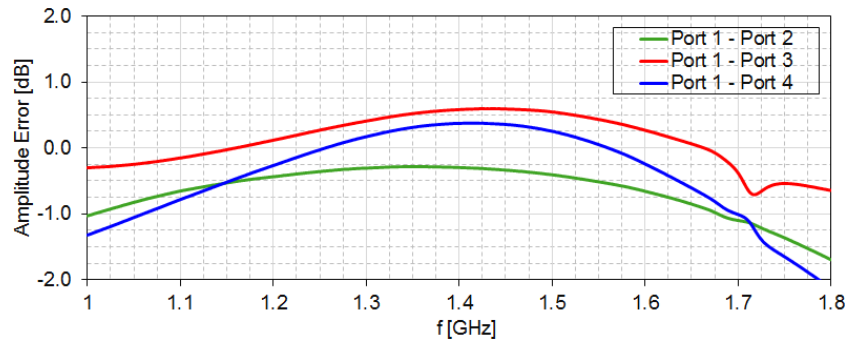


Figure 6.5: Feeding circuit measured amplitude errors.

Antenna feeding circuit measured phase angles relative to the antenna port 1 are shown in Figure 6.6 whereas the phase angle errors are shown in Figure 6.7. The phase angle errors do not exceed 4° in magnitude over the entire range. The exact impact of these errors alone on the antenna CP performance cannot be anticipated at this point.

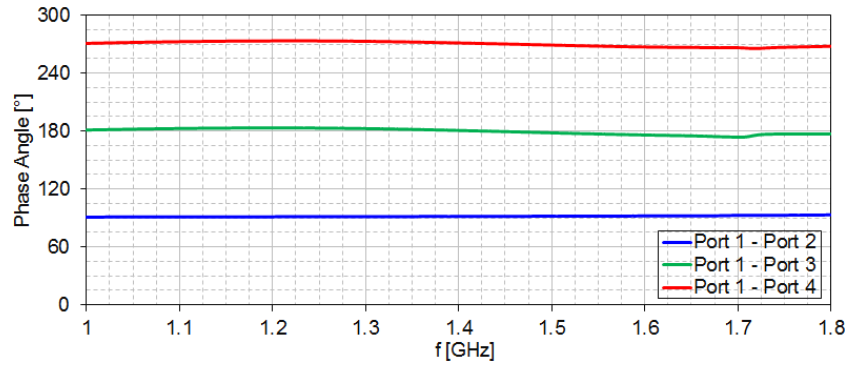


Figure 6.6: Feeding circuit measured phase angles.

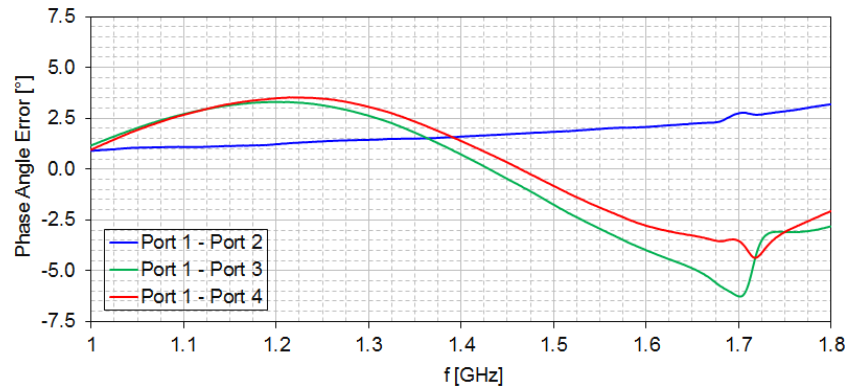


Figure 6.7: Antenna feeding circuit phase angle errors.

6.3 Measurement results

6.3.1 Resonant frequency and impedance bandwidth

In this step the antenna impedance was measured directly without the feeding circuit. Note that the input port impedance includes both the antenna and feeding circuit impedance, hence, to measure the antenna only input impedance the feeding circuit needs to be removed. The resonant frequency and impedance bandwidth were measured first without and then with the loading structure. This step was unnecessary from the antenna performance perspective, however, it gave a better understanding and confirmation of the DR alone performance and design considering the loading structure added complexity.

Without the loading structure, the measured resonant frequency varies from 1290 to 1350 MHz depending on the antenna port whereas the simulated resonant frequency is 1325 MHz, see Figure 6.8. The antenna also shows a second resonance between 1500 and 1550 MHz, which does not show in the simulation data. The impedance bandwidth is better than the simulation for all ports. The 10 dB RL covers between 1220 to 1580 MHz for a total bandwidth of 360 MHz or 25.7%, for most of the ports. The simulation data show 10 dB RL from about 1210 to 1520 MHz for a total bandwidth of 310 MHz or 22.7%.

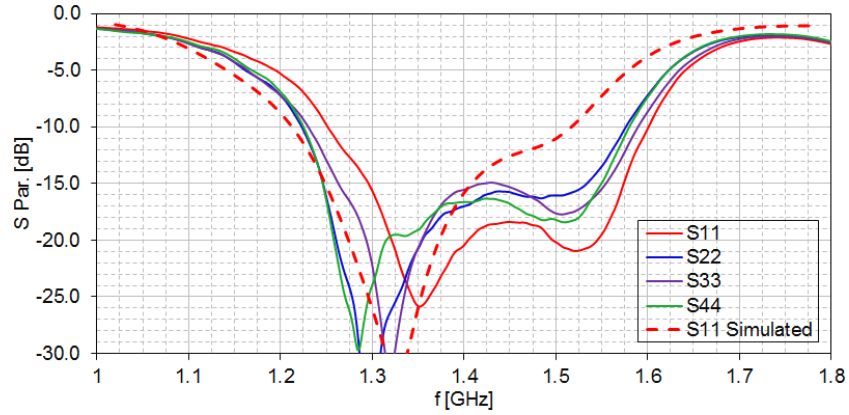


Figure 6.8: Unloaded annular DR S -parameter response.

With the loading structure, the antenna shows distinctively different input impedance response, see Figure 6.9. It clearly displays two distinctive resonances, one around 1230-1250 MHz and one around 1620 MHz consistently for all 4 ports. The simulated resonances were at 1230 MHz and 1580 MHz. The 10 dB RL impedance bandwidth is worse than the simulation. For the lower band the bandwidth varies between 130 and 180 MHz covering the lower band from 1160, 1125, 1205 and 1200 MHz to 1320, 1320, 1330 and 1330 MHz for antenna ports 1-4, respectively. The simulated 10 dB RL impedance bandwidth is 205 MHz covering from 1100 to 1305 MHz.

In the upper band there is a resonance shift of about 40 MHz, which partially shifts the 10 dB RL coverage outside of the GNSS upper band. The bandwidth is about 60 MHz covering from 1575 to 1645 MHz for all 4 ports. The simulated 10 dB RL impedance bandwidth is 100 MHz covering from

1525 to 1625 MHz.

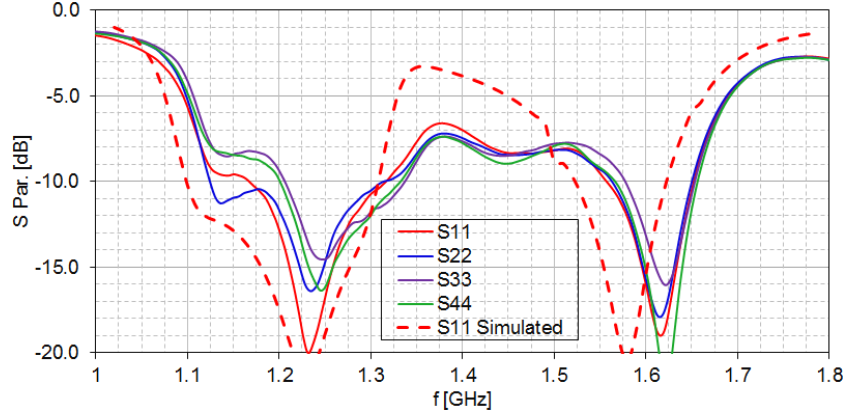


Figure 6.9: Loaded annular DR S -parameter response.

6.3.2 Excitation ports mutual coupling

The excitation ports mutual coupling was measured without the feeding circuit. The mutual coupling was measured with and without the loading structure. In both cases the measured coupling responses are similar to the simulation results over the entire antenna band, see Figure 6.10 and 6.11. In addition, in both cases there is an evident response shift of about 40 MHz comparing to the simulation data.

In the case of an unloaded resonator, the results indicate that within the antenna 10 dB RL bandwidth the adjacent and opposing port coupling range between -12 and -8 dB and -9 and -4 dB, respectively. With a loaded DR, the opposing port coupling is below -15 dB in the lower band and ranges -12 to -10 dB in the upper band. The adjacent port coupling is in a range between -10 to -8 dB in the lower band, while in the upper band it ranges between -9 and -7.5 dB, see Figure 6.11.

6.3.3 Realised gain

Simulated and measured RHCP directivity and realised gain at $\phi = 0^\circ$ and $\theta = 0^\circ$ are shown in Figure 6.12. The antenna demonstrates the stop-band response in both the antenna directivity and realised gain, which is significant

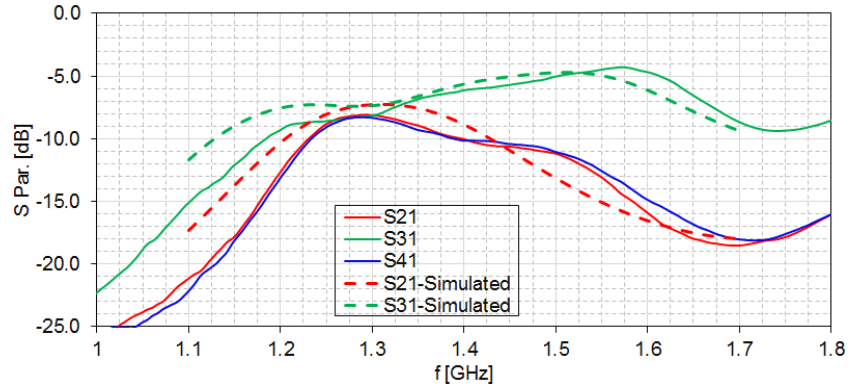


Figure 6.10: Unloaded annular DR excitation port mutual coupling.

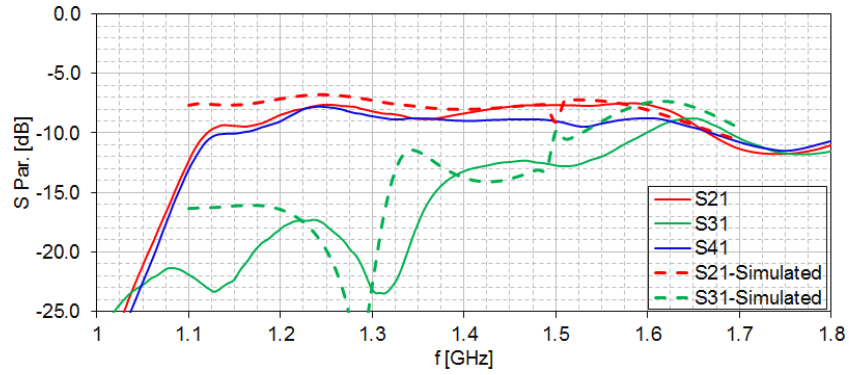


Figure 6.11: Loaded annular DR excitation port mutual coupling.

since it proves the effects of the loading structure on the DR. The stop-band resonance appears to be shifted by about 10 to 20 MHz comparing to the simulated data and the stop-band attenuation is about 3 dB less than the simulation. The bandwidth of the stop-band closely matches the simulated data.

The measured directivity at $\phi = 0^\circ$ and $\theta = 0^\circ$ exceeds the simulation results by about 2 dB over the entire band. In addition, there is a 1 dB step increases just after the stop-band (1375 MHz), which is not present in the simulations.

In the lower band, the realised gain is about 1 dB below, whereas in the upper band the realised gain is about 2 dB below the simulation results. This

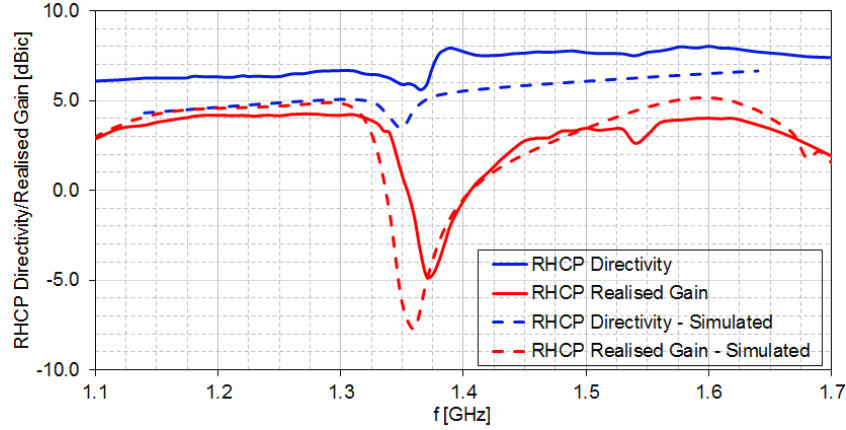


Figure 6.12: Measured and simulated RHCP directivity and realised gain at $\phi = 0^\circ$ and $\theta = 0^\circ$.

could imply that the antenna has a lower radiation efficiency and that there are other unaccounted losses. This is especially true for the upper band. The 0 dBic CP realised gain bandwidth at the antenna zenith, or the minimum realised gain as covered in section 2.5, significantly exceeds antenna's impedance bandwidth.

6.3.4 Radiation pattern and beamwidth

Figure 6.13 shows simulated and measured vertical radiation pattern at $\phi = 0^\circ$. As noted earlier, the realised gain appears to be 1 to 2 dB below the simulated results, which is also clear from the vertical radiation pattern. The most notable difference between the measured and simulated results is that the antenna has significantly higher gain below the horizon, especially at the lower frequencies. The radiation pattern symmetry appears to be degraded especially in the upper band, comparing to the simulations.

Table 6.1 provides a summary of measured and simulated 0 dBic CP realised gain beamwidth and HPBW data. The measured $G_r > 0$ dBic beamwidth for the antenna appears to be 15 to 25° below the simulated results, which is in part due to a lower realised gain. Although the HPBW is not a good indicator of a GNSS antenna radiation pattern performance, as covered in section 2.4, it is included for comparison reasons. The HPBW is around 100° in the lower band and 90° in the upper band, which is the same trend as in case of the 0 dBic beamwidth.

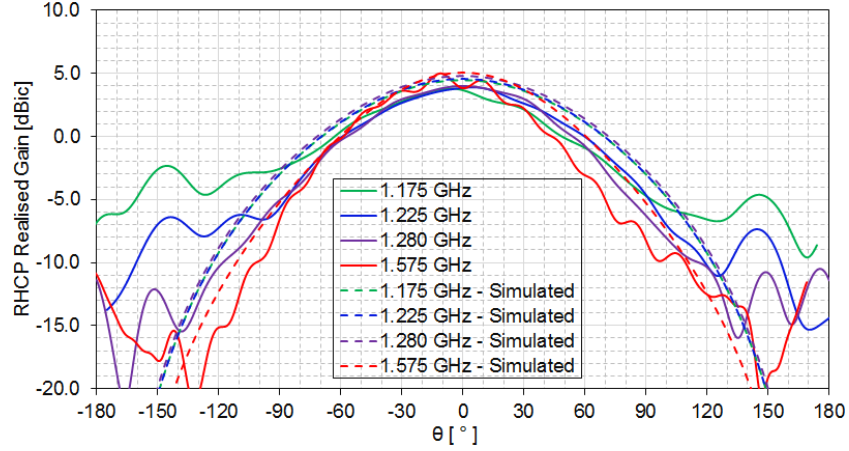


Figure 6.13: Simulated and measured vertical radiation pattern at $\phi = 0^\circ$.

Table 6.1: Summary of measured and simulated $G_r > 0$ dBic beamwidth and HPBW at $\phi = 0^\circ$.

Frequency [MHz]	Measured 0 dBic beamwidth [°]	Simulated 0 dBic beamwidth [°]	Measured HPBW [°]	Simulated HPBW [°]
1175	115	140	100	105
1225	120	140	100	105
1280	115	140	100	110
1575	105	120	90	90

6.3.5 Polarisation and AR

Figure 6.14 shows simulated and measured AR antenna performance at $\phi = 0^\circ$. Antenna 3 dB AR beamwidth is very close to the simulated. An exception is that the measured results show ripples and significantly less symmetry comparing to the simulations. This can be expected considering the gain performances observed earlier.

The rippling effect is more pronounced in the upper band than in the lower band, as it was observed for the antenna realised gain. Similarly, the largest AR performance difference between the measured and simulated data is also in the upper band. Table 6.2 provides a summary of measured and simulated 3 dB AR beamwidth data.

The measured results do not confirm the mutual coupling impact on the AR performance as severe as predicted in section 3.5.2. Similar findings are described also in sections 5.4.2 and C.2.3.

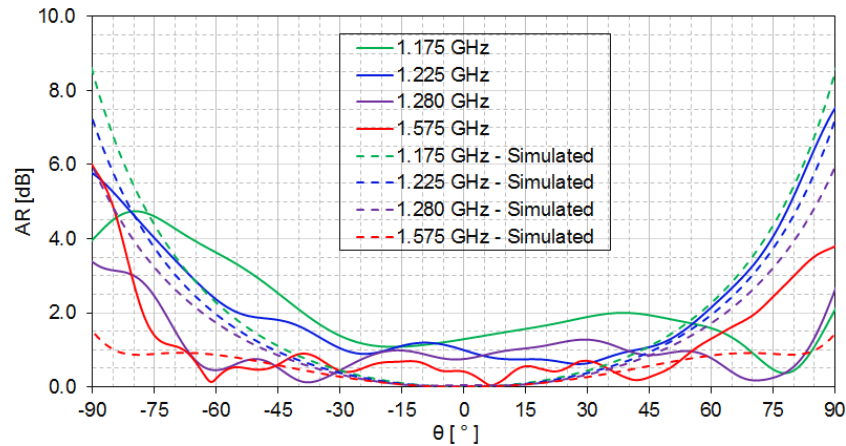


Figure 6.14: Measured AR beamwidth at $\phi = 0^\circ$.

Table 6.2: Measured and simulated AR beamwidth at $\phi = 0^\circ$.

Frequency [MHz]	Measured AR 3 dB beamwidth [°]	Simulated AR 3 dB beamwidth [°]
1175	>140	130
1225	135	140
1280	165	150
1575	160	>180

6.4 Analysis

The basic measured results have been presented. Comparing to the simulations, the measured performances deviate depending on the frequency and a specific parameter. There are potentially multiple sources of the observed deviations but most likely the following have the most significant impact: width of the excitation strips, position and alignment of the excitation strips, di-

mensions of the loading structure, conformality of the loading structure and the DR dielectric constant.

The width (w_{es}) of the excitation strips was found upon a close inspection to vary from 2.1 mm to 2.5 mm. The width varies from one strip to another but it was also found that each strip has an unintended taper as a result of fabrication. In addition, there appears that the strips are not properly aligned with the vertical axis, which resulted in strips being tilted. The tilt creates up to 2.5° position error on the DR top circumference.

The dimensions of the loading structure also appear to have a fabrication error. The widths of the upper and lower row wedges, w_7 and w_8 , respectively, appear to be larger although the gap widths w_2 and w_5 have correct dimensions. This fabrication error was found by measuring the unwrapped width (w_0) of the structure, see Figure 5.7. The fabricated w_0 was about 66.47 mm, which implied that each wedge is on an average 0.05 mm wider ($16 \times 0.05 \text{ mm} = 0.8 \text{ mm}$). To compensate for this error during the assembly process the entire fPCB was trimmed, which left two adjoining wedges about 0.4 mm narrower. It is hard to predict or simulate effects of this modification.

Conformality between the loading structure and the annular DR inner wall is reduced due to rigidity of the loading structure flex substrate. It was observed that the flex substrate bends easier where the metalization is removed such as the gaps between the wedges. This issue likely changed the response of the loading structure due to the air gap. The air gap likely contributed to the resonance shift observed in the upper band.

The 35 MHz resonant frequency error could be significant, however, the observed frequency shift is not consistent between the lower and upper resonances, see Figure 6.9. Thus, it is unlikely the dielectric constant error is not the only contributing factor to the frequency shift. Also, such an error was anticipated, hence, compensated by increasing the antenna design bandwidth. However, the impact is likely cumulative.

These sources were identified based on the parametric analysis. Other sources are possible as well but the parametric analysis did not identify any of the them as a significant contributor. However, any fabrication and assembly error likely contributed to the overall performance discrepancy.

6.4.1 This work and state-of-the-art

In this section the measured results are compared with the state-of-the-art (section 3.9). The following parameters are compared: $RL \geq 10$ dB BW, realised gain $G_r \geq 0$ dBic BW at the antenna zenith ($\theta = 0^\circ$), realised gain $G_r \geq 0$ dBic beamwidth (BmW), $AR \leq 3$ dB BW and BmW and the antenna total size, see Table 6.3.

This antenna improves or matches performances of the state-of-the-art antenna in all but two parameters: $G_r \geq 0$ dBic BmW and $AR \leq 3$ dB BmW. Both parameters are related to the radiation pattern and beamwidth and likely have the same origin. This design also reduces antenna's total profile height by close to 16 mm (38%) and provides a real-estate for the antenna front-end electronics underneath the ground plane. Both are significant.

Table 6.3: Summary of the results and state-of-the-art.

	This work	State of the art
$RL \geq 10$ dB BW [%]	36.3	33
$G_r \geq 0$ dBic BW [%]	>43	42
$G_r \geq 0$ dBic BmW [°]	105-120	140
$AR \leq 3$ dB BW [%]	>43	>43
$AR \leq 3$ dB BmW [°]	135-165	>180
Antenna total size [mm]	90×24.4	$90 \times 90 \times 39$

6.4.2 This work and thesis objectives

In this section the measured results are compared with the thesis objectives (section 4.1), see Table 6.4. This work meets or exceeds all but two of the thesis objectives: $G_r \geq 0$ dBic BmW and $AR \leq 3$ dB BmW. These are the same two parameters covered in the section above.

Table 6.4: Summary of the results and thesis objectives.

Thesis objective	Result
10 dB RL 1164 - 1606 MHz or 1164 - 1300 MHz and 1560 - 1606 MHz	Yes
Dual-sense CP	Yes
$G_r \geq 0$ dBic $BW \geq RL_{BW}$	Yes
$G_r \geq 0$ dBic $BmW \geq 140^\circ$	No
$AR_r \leq 3$ dB $BW \geq RL_{BW}$	Yes
$AR_r \leq 3$ dB $BmW \geq 140^\circ$	No
$D \leq 90$ mm and $H \leq 25$ mm	Yes

7 Conclusions and recommendations

A novel dielectric resonator based dual-sense CP antenna concept for the GNSS applications has been presented and validated. The antenna meets most of the thesis objectives as shown in Table 6.3 and 6.4. The results indicate that this antenna is a step forward in the family of similar DRAs previously published. The antenna resolves two of the main limitations of the current state of the art design in [46]. It reduces antenna's total profile height by close to 16 mm (38%) and provides a real-estate for the antenna front-end electronics underneath the ground plane. The radiation performances do not surpass the state of the art design only in two parameters: $G_r \geq 0$ dBic beamwidth and $AR \leq 3$ dB beamwidth.

The antenna introduces a new concept that further increases design flexibility comparing to the DRA based on simple resonator shapes. However, this is a complex antenna with stringent fabrication and assembly requirements. This is also potentially an expensive antenna comparing to the commonly found printed antennas typically used in the GNSS applications. The highest cost contributing factors are the DR fabrication and antenna assembly process.

The loading structure is the most unique feature of this antenna. It changes the antenna from a wideband to dual-band response while affecting most of the antenna performance parameters. Most importantly, it creates a new resonance at 1580 MHz (the upper-band), which is outside of the bandwidth of both, the cylindrical and unloaded annular DR. It shows the $HE_{11\delta}$ mode resonance enhancing properties in the lower-band, a sharp cut-off of the $HE_{11\delta}$ mode resonance in the stop-band then again the $HE_{11\delta}$ mode resonance in the upper band.

7.1 Recommendations and future work

An alternative fabrication technique needs to be investigated to eliminate the use of the flex PCB circuits due to significant difficulties with the assembly process. As an interim solution it is necessary to use thinner substrates that are more flexible, hence, provide higher conformity of the loading structure to the inner DR wall. Use of a higher dielectric constant DR is also suggested to further reduce the antenna size. However, use of a higher dielectric constant will likely increase fabrication and assembly complexity, which are already identified as the main deficiency of this antenna.

The bandwidth of the stop-band is narrow and it should be further investigated. In addition, it is not clear how the bandwidth of the upper-band is affected by the loading structure. Use of a different loading structure pattern should be investigated as well. The simulation results show that this antenna has significant group delay within in the upper band, which is likely a loading structure product.

The concept also rises an interesting scientific curiosity related to the interaction between the DR inner fields and the loading structure. Based on the simulation results there appear to be a discrepancy with the established model of a radiating cylindrical DR. This should be further investigated to be understood.

The mutual coupling impact on the AR performance needs to be investigated. All simulated and measured results indicate that the mutual coupling impact on the AR performance is not as severe as predicted in [28, pp.174-178] (see section 3.5.2).

Bibliography

- [1] E. Kaplan and C. Hegarty, *Understanding GPS: Principles and Applications*. Artech House, 3rd ed., 2017.
- [2] B. Hofmann-Wellenhof, H. Lichtenegger, and E. Wasle, *GNSS: Global Navigation Satellite Systems: GPS, GLONASS, Galileo, and more*. Springer Vienna, 2007.
- [3] M. Rip and J. Hasik, *The Precision Revolution: GPS and the Future of Aerial Warfare*. Naval Institute Press, 2002.
- [4] C. Balanis, *Antenna Theory: Analysis and Design*. John Wiley and Sons Inc., 3rd ed., 2012.
- [5] B. Rao, K. McDonald, and W. Kunysz, *GPS/GNSS Antennas*. GNSS technology and applications series, Artech House, 2013.
- [6] “High frequency electromagnetic field simulator (HFSS).” <http://www.ansys.com/Products/Electronics/ANSYS-HFSS>. Accessed: 2018-07-10.
- [7] B. Parkinson and J. Spilker, *Global Positioning System: Theory and Applications, Vol. 1*. Global Positioning System, American Institute of Aeronautics and Astronautics (AIAA), 1996.
- [8] “Minimum operational performance standards for global navigation satellite system (GNSS) airborne antenna equipment.” Radio Technical Commission for Aeronautics (RTCA), DO-228, 1995.
- [9] “Annex 6.8 interim GNSS antenna MOPS 6369.” <http://ec.europa.eu/DocsRoom/documents/953/attachments/1/translations/en/renditions/pdf>. Accessed: 2018-07-10.
- [10] E. Kaplan and C. Hegarty, *Understanding GPS: Principles and Applications*. Artech House, 2nd ed., 2005.
- [11] D. M. Pozar and S. M. Duffy, “A dual-band circularly polarized aperture-coupled stacked microstrip antenna for global positioning satellite,” *IEEE Transactions on Antennas and Propagation*, vol. 45, pp. 1618–1625, Nov 1997.

-
- [12] G. Massie, M. Caillet, M. Clénet, and Y. M. M. Antar, "A new wideband circularly polarized hybrid dielectric resonator antenna," *IEEE Antennas and Wireless Propagation Letters*, vol. 9, pp. 347–350, 2010.
- [13] R. Richtinger, "Dielectric resonators," *Journal of Applied Physics*, vol. 10, pp. 391–398, 1939.
- [14] M. McAllister and S. Long, "Rectangular dielectric-resonator antenna," *IEE Electronics Letters*, vol. 19, pp. 218–219, 1983.
- [15] S. Long, M. McAllister, and L. Shen, "The resonant cylindrical dielectric cavity antenna," *IEEE Transactions on Antennas and Propagation*, vol. 31, no. 3, pp. 406–412, 1983.
- [16] D. Kajfez, A. W. Glisson, and J. James, "Computed modal field distributions for isolated dielectric resonators," *IEEE Transactions on Microwave Theory and Techniques*, vol. 32, pp. 1609–1616, Dec 1984.
- [17] R. K. Mongia and P. Bhartia, "Dielectric resonator antennas—a review and general design relations for resonant frequency and bandwidth," *International Journal of Microwave and Millimeter-Wave Computer-Aided Engineering*, vol. 4, no. 3, pp. 230–247, 1994.
- [18] J. T. H. St. Martin, Y. M. M. Antar, A. A. Kishk, A. Ittipiboon, and M. Cuhaci, "Dielectric resonator antenna using aperture coupling," *Electronics Letters*, vol. 26, pp. 2015–2016, Nov 1990.
- [19] J. T. H. St-Martin, Y. M. M. Antar, A. A. Kishk, A. Ittipiboon, and M. Cuhaci, "Aperture-coupled dielectric resonator antenna," in *Antennas and Propagation Society Symposium 1991 Digest*, vol. 2, pp. 1086–1089, June 1991.
- [20] Y. M. M. Antar and Z. Fan, "Characteristics of aperture-coupled rectangular dielectric resonator antenna," *Electronics Letters*, vol. 31, pp. 1209–1210, July 1995.
- [21] Y. M. M. Antar and Z. Fan, "Theoretical investigation of aperture-coupled rectangular dielectric resonator antenna," *IEE Proceedings Microwave Antennas and Propagation*, vol. 143, pp. 113–118, Apr 1996.
- [22] A. A. Kishk, A. Ittipiboon, Y. M. M. Antar, and M. Cuhaci, "Dielectric resonator antennas fed by a slot in the ground plane of a microstrip line," *IEE publication No. 370, Antennas and Propagation*, vol. 1, pp. 540–543, 1993.
- [23] A. A. Kishk, A. Ittipiboon, Y. M. M. Antar, and M. Cuhaci, "Slot excitation of the dielectric disk radiator," *IEEE Transactions on Antennas and Propagation*, vol. 43, pp. 198–201, 1995.

-
- [24] A. Ittipiboon, R. Mongia, Y. Antar, P. Bhartia, and M. Cuhaci, "An integrated rectangular dielectric resonator antenna," in *IEEE Antennas and Propagation Society (AP-S) International Symposium, Ann Arbor, MI, USA*, pp. 604–607, Jul 1993.
- [25] G. D. Loos and Y. M. M. Antar, "A new aperture-coupled rectangular dielectric resonator antenna array," *IEE Microwave and Optics Technical Letters*, vol. 7, pp. 642–644, 1994.
- [26] M. B. Oliver, Y. M. M. Antar, R. K. Mongia, and A. Ittipiboon, "Circularly polarised rectangular dielectric resonator antenna," *IEE Electronics Letters*, vol. 31, pp. 418–419, 1995.
- [27] K. Luk and K. Leung, *Dielectric Resonator Antennas*. Research Study Press Ltd., 2003.
- [28] A. Petosa, *Dielectric Resonator Antenna Handbook*. Artech House, 2007.
- [29] Nasimuddin, X. Qing, and Z. N. Chen, "A compact dualband circularly polarized gnss antenna," in *2017 Progress in Electromagnetics Research Symposium*, pp. 2932–2935, Nov 2017.
- [30] B.-T. Lim, *Dielectric Resonator Antennas: theory and design, M. Eng. Thesis*. Massachusetts Institute of Technology, 1999.
- [31] R. Mongia and A. Ittipiboon, "Theoretical and experimental investigations on rectangular dielectric resonator antennas," *IEEE Transactions on Antennas and Propagation*, vol. 45, pp. 1348–1356, Sep. 1997.
- [32] Y. M. M. Antar, D. Cheng, G. Seguin, B. Henry, and M. G. Keller, "Modified waveguide model (mwgm) for rectangular dielectric resonator antenna (dra)," *Microwave and Optical Technology Letters*, vol. 19, no. 2, pp. 158–160, 1998.
- [33] L. Zou, *Dielectric Resonator Antennas: From Multifunction Microwave Devices to Optical-nano Antennas, PhD thesis*. Univesrsity of Adelaide, 2013.
- [34] X. S. Fang and K. W. Leung, "Designs of single-, dual-, wide-band rectangular dielectric resonator antennas," *IEEE Transactions on Antennas and Propagation*, vol. 59, pp. 2409–2414, June 2011.
- [35] D. M. Pozar, *Microwave Engineering*. John Wiley and Sons Inc., 4th ed., 2012.
- [36] G. Massie, *Investigation into a wideband circularly polarized hybrid dielectric resonator antenna*. Master of Applied Science thesis, Royal Military College of Canada, 2009.

-
- [37] J. Van Bladel, "On the resonances of a dielectric resonator of very high permittivity," *IEEE Transactions on Microwave Theory and Techniques*, vol. 23, pp. 199–208, Feb 1975.
- [38] K. M. Luk, M. T. Lee, K. W. Leung, and E. K. N. Yung, "Technique for improving coupling between microstripline and dielectric resonator antenna," *Electronics Letters*, vol. 35, pp. 357–358, March 1999.
- [39] X. Liang, T. A. Denidni, and L. Zhang, "Wideband l-shaped dielectric resonator antenna with a conformal inverted-trapezoidal patch feed," *IEEE Transactions on Antennas and Propagation*, vol. 57, pp. 271–274, Jan 2009.
- [40] L. Zhang, S. Zhong, and S. Xu, "Broadband u-shaped dielectric resonator antenna with elliptical patch feed," *Electronics Letters*, vol. 44, pp. 947–949, July 2008.
- [41] K. W. Leung, W. C. Wong, K. M. Luk, and E. K. N. Yung, "Circular-polarised dielectric resonator antenna excited by dual conformal strips," *Electronics Letters*, vol. 36, pp. 484–486, March 2000.
- [42] K. Khoo, Y. Guo, and L. C. Ong, "Wideband circularly polarized dielectric resonator antenna," *IEEE Transactions on Antennas and Propagation*, vol. 55, pp. 1929–1932, July 2007.
- [43] G. Massie, M. Caillet, M. Clénet, and Y. M. M. Antar, "A wideband circularly polarized rectangular dielectric resonator antenna," in *Proceedings of the Fourth European Conference on Antennas and Propagation*, pp. 1–5, April 2010.
- [44] M. Caillet, M. Clénet, and Y. M. M. Antar, *Miniaturized wideband circularly polarized hybrid dielectric resonator antenna*. DRDC Ottawa, Technical Memorandum TM 2012-125, Oct 2012.
- [45] M. Caillet, M. Clénet, and Y. M. M. Antar, *A Compact Circularly Polarized Hybrid Dielectric Resonator Antenna Array for CRPA Applications in the GPS/GNSS Frequency Bands*. DRDC Ottawa, Technical Memorandum TM 2013-091, Sep 2013.
- [46] S. K. Podilchak, J. C. Johnstone, M. Caillet, M. Clénet, and Y. M. M. Antar, "A compact wideband dielectric resonator antenna with a meandered slot ring and cavity backing," *IEEE Antennas and Wireless Propagation Letters*, vol. 15, pp. 909–913, 2016.
- [47] M. Lapierre, Y. M. M. Antar, A. Ittipiboon, and A. Petosa, "Ultra wideband monopole/dielectric resonator antenna," *IEEE Microwave and Wireless Components Letters*, vol. 15, pp. 7–9, Jan 2005.

-
- [48] Z. Wu, G. Drossos, M. A. Jusoh, J. Sha, and L. E. Davis, "Dielectric resonator antennas supported by infinite and finite ground plane," in *Tenth International Conference on Antennas and Propagation*, pp. 486–489, Apr 1997.
- [49] A. Petosa and A. Ittipiboon, "Dielectric resonator antennas: A historical review and the current state of the art," *IEEE Antennas and Propagation Magazine*, vol. 52, pp. 91–116, Oct 2010.
- [50] K. W. Leung, E. H. Lim, and X. S. Fang, "Dielectric resonator antennas: From the basic to the aesthetic," *Proceedings of the IEEE*, vol. 100, pp. 2181–2193, July 2012.
- [51] R. K. Gangwar, A. Sharma, M. Gupta, and S. Chaudhary, "Hybrid cylindrical dielectric resonator antenna with $HE_{11\delta}$ and $HE_{12\delta}$ mode excitation for wireless applications," *International Journal of RF and Microwave Computer-Aided Engineering*, vol. 26, pp. 812–818, 2016.
- [52] D. Guha, A. Banerjee, C. Kumar, and Y. M. M. Antar, "Higher order mode excitation for high-gain broadside radiation from cylindrical dielectric resonator antennas," *IEEE Transactions on Antennas and Propagation*, vol. 60, pp. 71–77, Jan 2012.
- [53] M. Caillet, M. Clenet, A. Sharaiha, and Y. M. M. Antar, "A compact wide-band rat-race hybrid using microstrip lines," *IEEE Microwave and Wireless Components Letters*, vol. 19, pp. 191–193, April 2009.
- [54] C. Caloz and T. Itoh, *Electromagnetic Metamaterials: Transmission Line Theory and Microwave Applications*. Wiley, 2005.
- [55] N. Engheta and R. Ziolkowski, *Metamaterials: Physics and Engineering Explorations*. Wiley, 2006.
- [56] F. Yang and Y. Rahmat-Samii, *Electromagnetic Band Gap Structures in Antenna Engineering*. The Cambridge RF and Microwave Engineering Series, Cambridge University Press, 2009.
- [57] S. Jović, M. Clénet, and Y. M. M. Antar, "Aperture coupled hybrid dielectric resonator antenna with an EBG back plane," in *17th International Symposium on Antenna Technology and Applied Electromagnetics (ANTEM)*, pp. 1–2, Jul 2016.
- [58] S. Jović, M. Clénet, and Y. M. M. Antar, "Multi-frequency gss dielectric resonator antenna with in-band filtering," in *12th European Conference on Antennas and Propagation (EuCAP 2018)*, pp. 1–4, April 2018.

-
- [59] “C-STOCK AK and AK-500 low loss plastic stock with adjusted dielectric constant, N-10-000-00061-F.” www.cumingmicrowave.com. Accessed: 2018-08-03.
- [60] “C-STOCK RH low dielectric constant, low loss structural foam, N-01-000-0127-E.” www.cumingmicrowave.com. Accessed: 2018-08-03.
- [61] “AD1000™.” <https://www.rogerscorp.com/>. Accessed: 2018-09-23.
- [62] “Dupont™ Pyralux® AP flexible circuit materials, technical data sheet.” www.pyralux.dupont.com. Accessed: 2018-08-03.
- [63] “Spherical near-field scanner systems.” <https://www.nsi-mi.com/>. Accessed: 2019-06-27.
- [64] “Spherical near-field antenna measurements: Keysight technologies and NSI.” <https://www.keysight.com/>. Accessed: 2019-06-27.
- [65] “Waveguide probes.” <https://www.nsi-mi.com/products/antenna-products/waveguide-probes>. Accessed: 2019-06-26.
- [66] “Galileo constellation information.” <https://www.gsc-europa.eu/system-status/Constellation-Information>. Accessed: 2018-07-06.
- [67] “Compass/BeiBou Navigation Satellite System.” <https://directory.eoportal.org/web/eoportal/satellite-missions/content/-/article/cnss>. Accessed: 2018-07-06.
- [68] “IEEE standard letter designations for radar-frequency bands.” IEEE Std 521-2002, Revision of IEEE Std 521-1984, 2003.
- [69] “GNSS signals.” https://gssc.esa.int/navipedia/index.php/GLONASS_Future_and_Evolutions. Accessed: 2018-07-19.
- [70] C. J. Hegarty, “GNSS signals — an overview,” in *IEEE International Frequency Control Symposium Proceedings, Baltimore, MD*, pp. 1–7, Jul 2012.
- [71] “ESA Navipedia.” https://gssc.esa.int/navipedia/index.php/GNSS_signal. Accessed: 2018-05-17.
- [72] C. Barth, U. Inan, T. Lee, and I. Linscott, “Subsampling GPS receiver front-end,” *Stanford University, Department of Electrical Engineering*, pp. 19–20, 2011.
- [73] J. R. G. Oya, A. Kwan, F. M. Chavero, F. M. Ghannouchi, M. Helaloui, F. M. Lasso, E. López-Morillo, and A. T. Silgado, “Subsampling receivers with applications to software defined radio systems,” *IntechOpen*, 2012.

- [74] “PLGR 96.” <https://www.ion.org/museum/files/PLGR-9~1.PDF>. Accessed: 2018-07-07.
- [75] “DAGR.” <https://www.rockwellcollins.com/-/media/Files/Unsecure/Products/Product-Brochures/Navigation-and-Guidance/GPS-Devices/DAGR-brochure.pdf>. Accessed: 2018-07-07.
- [76] L. Chu, D. Guha, and Y. Antar, “Comb-shaped circularly polarized dielectric resonator antenna,” *IEE Electronic Letters*, vol. 42(14), pp. 785–787, 2006.
- [77] Y. M. Pan, K. W. Leung, and K. Lu, “Omnidirectional linearly and circularly polarized rectangular dielectric resonator antennas,” *IEEE Transactions on Antennas and Propagation*, vol. 60, pp. 751–759, Feb 2012.
- [78] W. W. Li and K. W. Leung, “Omnidirectional circularly polarized dielectric resonator antenna with top-loaded alford loop for pattern diversity design,” *IEEE Transactions on Antennas and Propagation*, vol. 61, pp. 4246–4256, Aug 2013.
- [79] C. Y. Huang, J. Y. Wu, and K. L. Wong, “Cross-slot-coupled microstrip antenna and dielectric resonator antenna for circular polarization,” *IEEE Transactions on Antennas and Propagation*, vol. 47, pp. 605–609, April 1999.
- [80] “Dupont™ Pyralux® AC flexible circuit materials, technical data sheet.” www.pyralux.dupont.com. Accessed: 2018-07-27.

Appendices

A GNSS background

This appendix provides the minimum background information about the GNSS required to properly define and understand the thesis problem as outlined in Chapter 2. References [7], [10] and [2] cover in-depth the subject of GNSS and well beyond what is required here.

A.1 Fundamentals of GNSS

A GNSS consists of three segments: space, ground and user. The space segment consists of a satellite constellation typically in the Mid-Earth Orbit (MEO). The number of satellites varies from one GNSS to another and ranges from 24 to over 30 satellites. The satellites are distributed typically into 3 to 4 orbital planes each inclined between 50° and 65° . The GNSS satellites in MEO have orbital periods ranging from about 12 h to 14 h. Each satellite transmits a minimum of 4 signals in two or more frequency bands. All signals are time and phase synchronized within one satellite and within an entire constellation.

The ground segment consists of the command and control (C2) and constellation monitoring networks. The monitoring networks are focused primarily on the satellite orbital parameters and signal timing accuracy. Both are detrimental to performances of the user segment. This segment is not relevant for the subject of this thesis and it will not be covered any further.

The user segment consists of the GNSS receivers, which are designed to receive and demodulate the satellite signals and provide the navigation measurements. The fundamental navigation measurements consist of position, velocity and time. Other navigation parameters are calculated, estimated or extrapolated from these three fundamental parameters. A GNSS receiver is a receive-only device, hence, a GNSS antenna is a receive-only antenna.

A GNSS antenna has specific beamwidth requirements in the elevation plane. Unlike point-to point communications, the GNSS concept is based on one-way communication from multiple mobile space-based transmitters to one receiver on or relatively close to the Earth surface (Figure 2.2). The transmitters, i.e. satellites, are in a constant motion relative to a receiver and during one-half of an orbital period (approximately 6 h) a GNSS satellite traverses the entire hemisphere. Hence, an antenna needs to receive a signal from any direction in the upper hemisphere.

A.2 Status of GNSS

As of early 2018 there are two fully operational GNSSs and two under development. The Global Positioning System (GPS) was the first fully operational GNSS and it was developed and operated by the United States Air Force (USAF). Initially, GPS was primarily used by the military, however, today in the civilian domain it is the most commonly used system worldwide. An initial operational capability (IOC) was declared in 1993 whereas the full operational capability (FOC) was declared in 1995 [2, pp.10]. The second GNSS that reached the full operational capability is Globalnaya Navigatsionnaya Sputnikovaya Sistema (GLONASS). Soviet Union (SU) started development of this system in the mid 1970s whereas IOC and FOC were declared in 1993 and 1996, respectively, under the Russian Federation as a successor state [2, pp.341-342].

Both GPS and GLONASS were developed primarily for the military applications but both also provide at least one open signal for the civilian users. The US Military and its Allies, including Canadian Armed Forces (CAF) use GPS exclusively.

The two GNSS under development are Galileo, developed and operated by the European Space Agency (ESA) and BeiDou, also known as Compass, developed and operated by the Government of China. Both systems are in advanced stages of completion and each have multiple fully functional satellites in orbits. The Galileo satellite constellation as of July 2018 consists of 14 usable satellites and additional six ready for commissioning [66]. Once fully deployed, the Galileo space segment will include a constellation of 30 satellites in MEO. Galileo was initially envisioned as a commercial only system, however, a military application is possible.

BeiDou or Compass is different to a degree from the three previously mentioned systems. In addition to its global coverage it also includes elements of a regional satellite navigation system (RSNS) covering the area of East Asia and Pacific Ocean. The BeiDou program began in 1993 whereas the first two experimental satellites were launched in 2000. The BeiDou satellite constellation is partially completed consisting of 22 operational satellites, as of Nov 2017, out of total 35 required [67]. The constellation includes satellites in both MEO and in the Geostationary Earth Orbit (GEO).

In addition to the GNSS mentioned above there are two RSNS and three satellite based augmentation systems (SBAS). However, none of these systems has any significant impact on the GNSS antenna requirements relevant for this thesis work. This observation is based on the facts that they use the same frequency bands and signal polarisation, see [10, pp.397-430] for additional information about RSNS. References [5, pp.3-5] and [10, pp.2-11] provide extended summaries of the current and proposed GNSS systems as of 2013 and 2005 respectively.

A.3 GNSS signals, modulation and spectral deconfliction

From an antenna design perspective, a signal spectral occupancy is one of the key design parameters since it determines the bandwidth requirements. The GNSS signals are assigned to two frequency ranges in the L-band as per IEEE standard 521 for letter designations for radar-frequency bands [68]. The first frequency range occupies frequencies from about 1164 to 1300 MHz while the second occupies frequencies from about 1559 to 1616 MHz. These two bands are also referred to as "the lower L-band" and "the upper L-band", respectively.

To increase the spectral efficiency most of the GNSS signals share the same frequency bands [69]. The spectral deconfliction is accomplished using different forms of digital signal modulation techniques in a combination with one of the spread-spectrum multiple access encodings. Reference [69] lists all GNSS allocated and proposed signals along with accepted designations as of 2017. For more information about the GNSS signals see [2, pp.309-430], [70] and [71].

A.3.1 GPS Signals

The GPS user equipment operates in three frequency bands: L1 centered at 1575.42 MHz, L2 centered at 1227.60 MHz and L5 centered at 1175.45 MHz. Each of the occupied bands is about 24 MHz wide and accommodates between 1 and 4 different signals as shown in Table A.1 . In addition, GPS employs L3 and L4 bands at 1381.05 MHz and 1379.913 MHz, respectively. These two frequencies are used as a part of the nuclear event detection system (NDS) [2, pp.328]. Open literature provides very little additional information about the signals in L3 and L4 bands.

The legacy GPS signals such as the Coarse Acquisition (C/A) and Precision (P) code signals use the binary phase shift keying (BPSK) for data modulation whereas the code division multiple access (CDMA) is used for signal deconfliction. The new military signal, also called the M-code, uses the binary offset carrier modulation (BOC) and CDMA for signal deconfliction.

Table A.1: GPS signals.

Band designation	Signal designation	Carrier frequency [MHz]	Occupied BW [MHz]	Modulation	Multiple access technique
L1	C/A	1575.42	2.046	BPSK	CDMA
L1	P	1575.42	20.46	BPSK	CDMA
L1	L1C	1575.42	2.046	BOC	CDMA
L1	M	1575.42	24	BOC	CDMA
L2	L2C	1246.0	2.046	BPSK	CDMA
L2	P	1246.0	20.46	BPSK	CDMA
L2	M	1227.6	24	BOC	CDMA
L5	L5C	1176.45	20.46	BPSK	CDMA

A.3.2 GLONASS Signals

As of 2018 GLONASS operates in two bands: L1 centered around 1602 MHz and L2 centered around 1246 MHz. Both bands occupy about 8 MHz. In addition to these two bands there is a proposal for additional signals to be allocated in four bands each occupying from 2 to 24 MHz [69]. GLONASS is the only system that uses frequency division multiple access (FDMA) for its legacy signals. The new proposed signals will use BOC and CDMA, see Table A.2.

A.3. GNSS signals, modulation and spectral deconvolution

Table A.2: GLONASS signals.

Band designation	Signal designation	Carrier frequency [MHz]	Occupied BW [MHz]	Modulation	Multiple access technique
G1	C/A	1602.00	8.0	BPSK	FDMA
G1	P	1602.00	8.0	BPSK	FDMA
G1	L1OC	1600.995	2.0	BOC	CDMA
G1	L1OCM	1600.995	12	BOC	CDMA
G1	L1OMI	1575.42	2.0	BOC	CDMA
G2	C/A	1246.0	8.0	BPSK	FDMA
G2	P	1246.0	8.0	BPSK	FDMA
G3	L3OC	1202.025	UNK	UNK	UNK
G5	L5OC	1176.45	UNK	UNK	UNK

A.3.3 Galileo Signals

Galileo signals occupy four frequency bands, three in the lower and one in the upper L-band, each occupying 12 to 41 MHz, see Table A.3.

Table A.3: Galileo signals.

Band designation	Signal designation	Carrier frequency [MHz]	Occupied BW [MHz]	Modulation	Multiple access technique
E1	E1A	1575.42	32	BOC	CDMA
E1	E1B	1575.42	12	BOC	CDMA
E1	E1C	1575.42	12	BOC	CDMA
E6	E6A	1278.25	41	BOC	CDMA
E6	E6B	1278.25	12	BPSK	CDMA
E6	E6C	1278.25	12	BPSK	CDMA
E5	E6A	1176.45	24	BOC	CDMA
E5	E6B	1207.14	24	BOC	CDMA

A.3.4 BeiDou Signals

BeiDou COMPASS 2 and 3 have 12 signals distributed in four frequency bands, two in the lower and two in the upper L-Band, each occupying from 2 to 24 MHz, see Table A.4.

Table A.4: BeiDou signals.

Band designation	Signal designation	Carrier frequency [MHz]	Occupied BW [MHz]	Modulation	Multiple access technique
B1	B1-OS	1561.098	2	BPSK	CDMA
B1	B1-AS	1561.098	2	BPSK	CDMA
B1	B1-C	1575.42	2	BOC	CDMA
B1	B1	1575.42	24	BOC	CDMA
B2	B2a-D	1176.45	24	BOC	CDMA
B2	B2a-P	1176.45	24	BOC	CDMA
B2	B2b-D	1207.14	24	BOC	CDMA
B2	B2b-P	1207.14	24	BOC	CDMA
B2	B2-OS	1207.14	2	BPSK	CDMA
B2	B2-AS	1207.14	20	BPSK	CDMA
B3	B3	1268.52	10	BPSK	CDMA
B3	B3-A	1268.52	24	BOC	CDMA

A.4 GNSS Receiver

A generic GNSS receiver functionally consists of five major blocks; antenna, signal down-conversion, analog to digital converter (ADC), digital signal processor (DSP), user interface (UI) and usually external interface (Figure A.1). The antenna is the first element in the signal acquisition and processing chain. An antenna usually includes an active front-end, which is located very close to the receiving element to minimize the insertion losses. The front-end consists of one or more band-pass filters (BPF) and a low noise amplifier (LNA).

Once the analog signal is band-filtered and amplified, it is then down-converted to the intermediate frequency (IF) or the base-band (BB). The down-conversion is usually based on the super-heterodyne concept that relies on nonlinear mixing of the input signal with the local oscillator (LO) signal. A new concept based on a sub-sampling receiver architecture has been proposed in [72] and [73]. Under the sub-sampling concept the RF signal is converted to IF or BB by aliasing. Hence, a sub-sampling receiver sample the incoming RF signal at a frequency close to the frequency of the information content rather than the carrier frequency. Such concept significantly simplifies and reduces size of a receiver but it increases the system added signal NF by at least 3 dB and typically closer to 10 dB. Newer high speed ADC allow direct signal

sampling, which eliminates the added NF and significantly reduces receiver complexity.

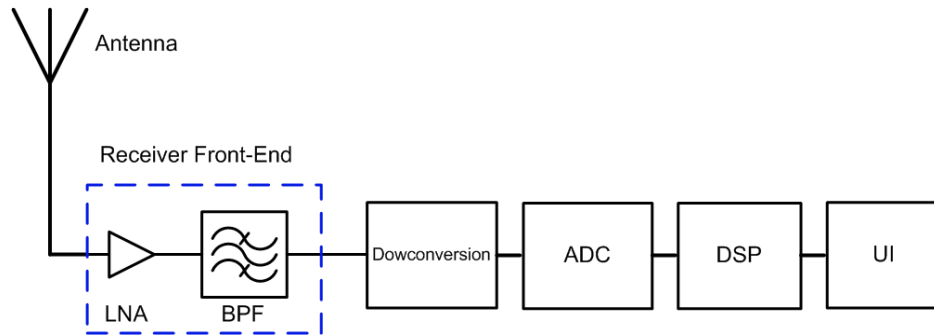


Figure A.1: GNSS receiver functional block diagram.

After the signal down conversion, it is then converted to a digital signal at the ADC stage. The digitized signal is then processed at DSP to extract the navigation messages. Using the extracted navigation messages the processor estimates the position, velocity and time (PVT), which are then provided to a user through the UI or an external digital interface.

Figure A.2 shows three military handheld GPS receivers: PLGR 96+, PLGR 3 and DAGR, all made by Rockwell Collins Inc. [74][75]. The three receivers represent a rapid evolution of the military receiver technologies in the time period between mid-1990s and mid 2000s. In addition to the receiver internal electronics evolution, the receiver antennas have developed as well. Note that PLGR 96+ uses externally mounted large helical antenna whereas both PLGR 3 and DAGR use internally mounted antennas.

A.5 Single vs. dual frequency and single vs. multiple GNSS

Access to two coherent signals using significantly spaced carrier frequencies allows a receiver to compute the signal ionospheric propagation delay [2, pp.384]. Examples of such GNSS frequencies are GPS L1 (1575.42 MHz) and GPS L2 (1226.70 MHz) and Galileo E1 (1575.42 MHz) and E5 (1207.14 MHz). A proper estimation of the ionospheric delay increases accuracy of a PVT solution. Such a capability is otherwise available only through use of an additional augmentation services. Another advantage of a dual frequency re-



Figure A.2: Military handheld GPS receivers: PLGR+96, PLGR 3 and DAGR (© J. Lang, DRDC Ottawa, 2003).

ceiver is reduced vulnerability to the EM interference. These two capabilities were initially available only to the military users. However, addition of the GPS L2C signal gave the same advantages to the civilian users.

Use of multiple GNSS signals gives similar advantages as the dual frequency but with an additional layer or redundancy. In particular, availability of a large number of satellites allows a receiver to select the signals from satellites that provide the best satellite geometry for the most optimum position solution, which is in the literature referred to as the Geometry Dilution of Precision (GDOP). A dual or multi-GNSS receiver will have a higher accuracy, integrity, reliability and availability relative to a single-GNSS receiver. In the military domain use of the GNSS that are under a foreign nation control is usually limited due to the security implications.

From the antenna requirements perspective there are multiple parameters affected by the number of frequencies and GNSS used, the bandwidth is an obvious one. The antenna phase center and group delay variations are other two parameters which are addressed in the main mater.

B Review of single-port CP excitation for DRA

The far-field CP radiation from a DR can be excited using one or multiple excitation ports. Antennas using single-port excitation typically provide a narrow *AR* BW and beamwidth and can provide only uni-sense CP. However, single-port CP excitation usually provides a more compact and simpler design comparing to a multi-port excitation.

To generate CP using a single feed there are two techniques: exciting a single mode where the field distribution is perturbed due to a change in the DR geometry or boundary conditions and to excite two identical modes but geometrically orthogonal and quasi-degenerate. The quasi-degeneracy will provide the phase quadrature between the excited modes, thus, CP radiation.

B.1 Single mode

This method relies on the perturbation of an excited mode in a DR by adding interfaces in the dielectric such as two dielectrics of different permittivities, or by adding a metallic strip or patch to the resonator. Such modifications change resonator's boundary conditions and as a consequence impact the field distribution of the excited mode.

An example of this a method is presented in [76] where the $HE_{11\delta}$ mode is excited in a cylindrical DR using a single coaxial probe. The dielectric cylinder was modified by cutting slots into resonator's upper surface to produce CP, see Figure B.1. This concept operates on the $HE_{11\delta}$ mode revolution symmetry, which allows any number of $HE_{11\delta}$ modes to be excited around the cylinder circumference. The slots add a dielectric permittivity gradient that creates a second set of fields as a result of the primary mode field propagation within

the DR. CP occurs when the phase difference between the parallel and perpendicular fields is 90° , and the amplitude of the parallel and perpendicular fields is equal.

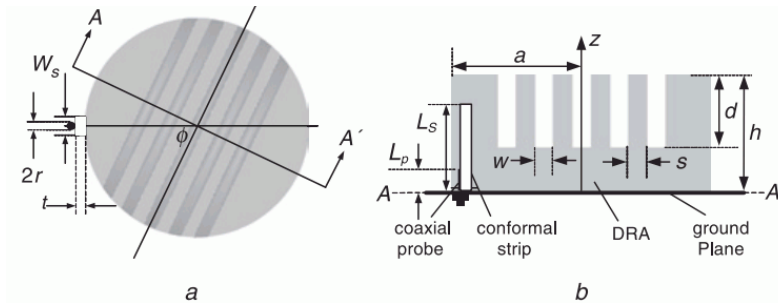


Figure B.1: Circularly polarised comb-shaped cylindrical DRA (from [76]).

Another example includes a rectangular DR centrally fed by a probe that radiates like an electric monopole but generating omni-directional CP fields [77]. Slots are introduced to the DR sidewalls, exciting a degenerate mode for the generation of CP radiation, see Figure B.2. Its operating mode is analogous to the $TM_{01\delta}$ mode of a cylindrical DRA.

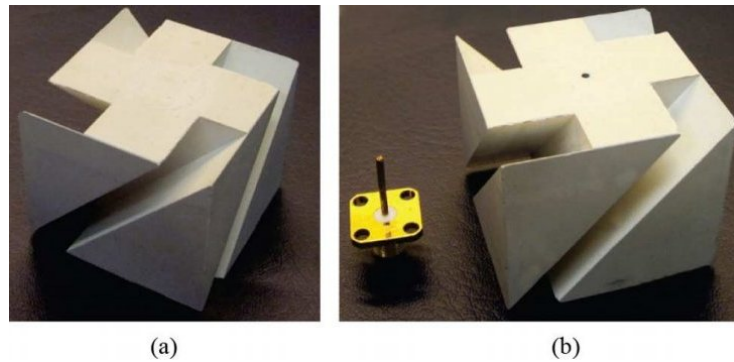


Figure B.2: Omnidirectional CP rectangular DRA (from [77]).

In [78] an omnidirectional CP DRA using a modified Alford loop is reported. The antenna is based on a top-loaded cylindrical DR center fed by an axial probe and excited in $TM_{01\delta}$ mode. By tuning the Alford loop dimensions, the DR external fields are made equal in amplitude but 90° different in

phase, hence, generating an omnidirectional CP radiation pattern.

The $AR < 3$ dB BW of such antennas is small since the field perturbation changes as a function of the frequency. The antennas in [76] and [78] yield about 4% and 7%, respectively, of $S_{11} < 10$ dB impedance and $AR < 3$ dB BW.

B.2 Dual mode

This method relies on the resonator geometry that supports two geometrically orthogonal and quasi-degenerate modes each having a similar resonant frequency and overlapping band coverages. The resonant frequencies of the two perturbed modes need to satisfy eq. B.1 and B.2 to create a condition for existence of two orthogonal modes.

$$f_x = \frac{f_0}{1 + \frac{1}{2Q_x}} \quad (\text{B.1})$$

$$f_y = \frac{f_0}{1 - \frac{1}{2Q_y}} \quad (\text{B.2})$$

The f_x and f_y are the resonant frequencies of the quasi-degenerate modes, and Q_x and Q_y are their respective Q-factors. The impedance and AR BW strongly depend on the asymmetry between the modes, hence $f_x \neq f_y$ and $Q_x \neq Q_y$, see [28, pp.178-181]. Using eq. B.1 and B.2 antenna normalized input impedance can be estimated from eq. B.3 as a function of Q-factor [28, pp.178-181].

$$Z = 1 + \frac{jQ}{ff_0}(f^2 - f_0^2) \quad (\text{B.3})$$

A good example of a single-feed dual mode DRA is given in [26]. In that case, a quasi-squared DR is excited through a single aperture. The aperture excites $TM_{\delta 11}^x$ and $TM_{1\delta 1}^y$ modes, which are geometrically orthogonal, see Figure B.3. The impedance and AR BW of the antenna are both 6.6% but with an overlapping BW of only 4%.

Another example of this concept is the use of two crossed slots of different arm lengths in [79]. A CP BW of 4.7% is achieved by optimizing the slot lengths and the open-end feeding microstrip line stub length. A number of single-point feed CP DRA concepts is also covered in [28, pp.178-190]. The

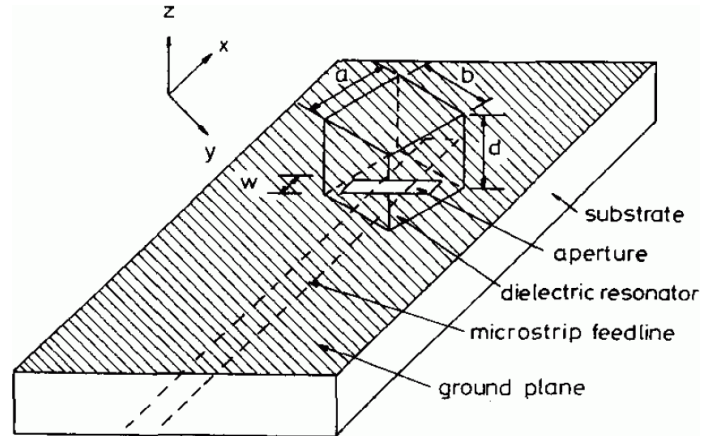


Figure B.3: Aperture fed CP rectangular DR (from [26]).

theoretical impedance and AR BW of the presented concepts range between 2% to 24% and 1% to 12%, respectively [28, pp.181].

Petosa in [28] summarizes impedance and AR BW performances of the single feed excited CP DRA as a function of the Q-factor and f_x and f_y frequencies. The impact of the difference between f_x and f_y confirms that a DR under such excitation conditions resonates in two orthogonal but distinctive modes. However, such resonant conditions produce practical AR BW only half of the impedance BW due to the phase difference ψ impact on the AR in eq. 3.42.

C Cylindrical DRA design optimization

This Appendix is an extension of Chapter 4. In sections 4.7.3 and 4.8 it was hypothesized that a DR design needs to consider all antenna parameters such as feeding mechanism, number of excitation ports and ground plane. That hypothesis was based on the fact that free space suspended Q_u , which is based on the design equations in section 4.3, cannot be replicated in practice, hence, a more practical conditions need to be considered.

C.1 Cylindrical DR optimization

The DR design based on the analytical process from [28], which is followed in section 4.3 does not take in account impact of the external parameters such as the finite size ground plane and DR excitation technique. The impact of these two parameters is significant as shown earlier. In addition, the resonant frequency, Q-factor and radiation efficiency appear to be affected by the number of excitation ports. As shown in Figure 4.8, use of four excitation strips instead of one, almost doubles the impedance BW.

These findings indicate that a DR design needs to consider all of the parameters, including the ground plane size, excitation technique and a number of excitation ports, in addition to h , r/h ratio and ϵ_r , which are the only parameters considered in the analytical design process. Hence, it is likely that all the parameters need to be optimised to maximise antenna performance.

To test the hypothesis, dimensions of a cylindrical DR of $\epsilon_r = 10$ on a ground plane of radius $r_{GP} = 45 \text{ mm}$ were optimised for a maximum impedance BW. The starting values of $h = 26.0 \text{ mm}$ and $r/h = 1.194$ ratio were used but h and r/h ratio were allowed to range in between $18 < h <$

32 mm and $0.4 < r/h < 5$, respectively. The DR was excited using four tin-wire probes as described in section 4.5.1. The probes were fed in a quadrature to excite the CP radiation pattern.

The DR radius r and height h converged at 25.77 mm and 30.94 mm, respectively, for $r/h = 1.2006$. These DR dimensions do not match the dimensions based on the analytical design procedure presented in section 4.3. The simulation results are shown in Figure C.1. The input impedance BW exceeds 200 MHz, or 13.8%, which is higher than predicted by the design. The input impedance BW is also higher than the simulated for unoptimized DR presented in Figure 4.8 and Table 4.4. These results confirm the hypothesis but do not explain the discrepancy.

Figure C.1 also shows S_{21} and S_{31} parameters, which indicate the mutual coupling between ports 1 and 2 (adjacent) and 1 and 3 (opposing), respectively. The coupling level between the opposing ports is high and approaching -3 dB around 1.6 GHz.

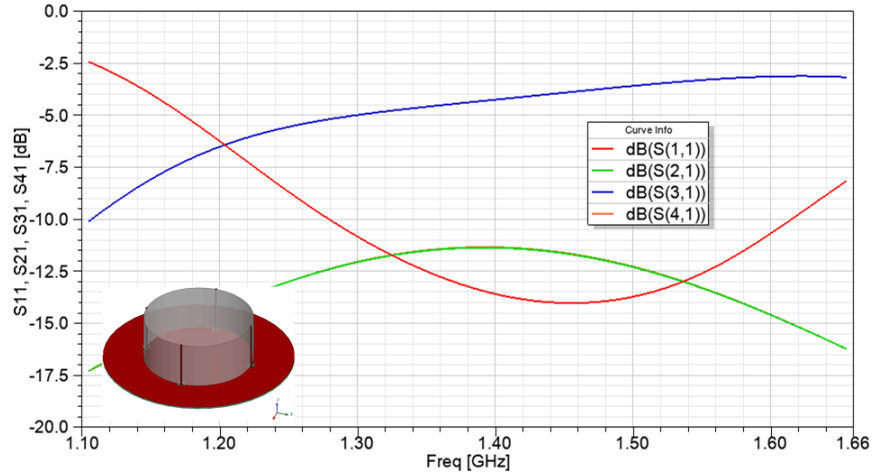


Figure C.1: S -parameter response of a cylindrical DRA optimised for the excitation mechanism and ground plane size.

C.2 Cylindrical DRA optimization

In this section the above hypothesis is applied on the entire antenna, which includes antenna impedance matching, and considers antenna fabrication.

C.2.1 Antenna design

Considering all the findings this far, an antenna concept based on a cylindrical DR and a circular ground plane of 90 mm diameter can be proposed. To achieve CP, the DR is fed in quadrature. The DR is excited using four vertical conformal metallic strips, which were found to provide the highest impedance BW, as shown in section 4.5. To further improve antenna impedance BW, $\varepsilon_r = 10$ is used for the DR.

To ensure a gap-less conformal coupling between the strips and DR, the strips could be printed on a flexible substrate similar to [80], which is $\varepsilon_r = 3.6$ and 0.072 mm (3 mil) thick. The strips are connected to 1 mm diameter vias through the ground plane. To ensure a gap-less interface between DR and the ground plane, which was noted as a problem in the designs presented in [45, 46], the DR is affixed to the substrate and ground plane using four fasteners M3x0.5x30 made of polyester ($\varepsilon_r = 3.2$). The fasteners are also used to align the DR with excitation strips and vias, which should simplify the assembly process.

In this concept proposal additional emphasis is put into the antenna input impedance matching. To improve the antenna impedance matching, the via-though pad diameter and a single microstrip transformer are used. The problem with the $HE_{11\delta}$ mode impedance matching was observed earlier and also noted in [16].

C.2.2 Design optimization

The proposed concept is then optimised using the HFSS optimization tool where the optimization goal was to maximise input impedance BW within the GNSS band. The starting dimensional values were those found earlier. The final optimised antenna assembled and exploded views are shown in Figure C.2.

The final DR dimensions converged to radius and height of 30.8 mm and 24.4 mm, respectively, for r/h ratio of 1.2629. The excitation strip width converged at 2.1 mm and length extending over the entire DR height. The strips are tapered over 12.9% of length starting at the via pad as shown in Figure C.2 insert.

To improve the antenna input impedance BW one-section microstrip transformer is used. The transformer is 22.8 mm long and 1.32 mm wide. The

via-through pad radius (1.2 mm) and its ground plane coaxial radius were also used to improve the input impedance matching.

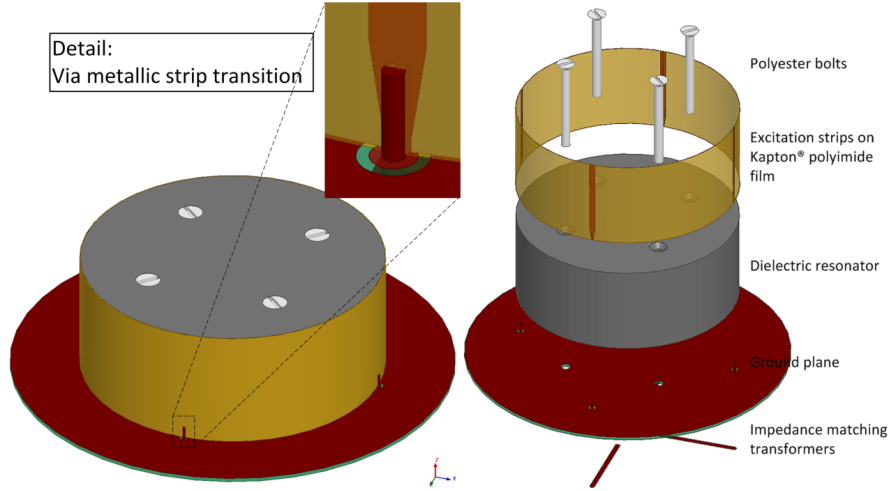


Figure C.2: Cylindrical DRA: a) assembled view and b) exploded view.

C.2.3 Simulation results

The antenna S -parameter responses are shown in Figure C.3. It exhibits $RL > 10$ dB between 1235 and 1630 MHz, which covers the entire upper and about half of the lower GNSS band (Figure C.3). The total impedance BW is about 395 MHz or about 27.7%. The mutual coupling between the adjacent excitation ports 1 and 2 (S_{21}) is under -10 dB below 1.27 GHz and above 1.41 GHz. The same can be assumed for other the adjacent ports considering the antenna symmetry. The coupling between the opposite ports 1 and 3 (S_{31}) is below -5 dB for frequencies below 1.3 GHz whereas it approaches -3.5 dB for frequencies between 1.56 to 1.61 GHz, which is high.

The realized RHCP gain at the antenna zenith is about 5 dBic in the upper band whereas it ranges between 4 and 4.3 dBic in the lower band (Figure C.4). The minimum realised gain BW ($G_R > 0$ dBic) covers frequencies from about 1.11 to 1.73 GHz, which significantly exceeds input impedance BW. Even though the realised gain is not constant across the entire band and RL below 1235 MHz is well below 10 dB, the realised gain never drops below 3 dBic at the antenna zenith.

The radiation patterns in the elevation plane are provided in Figure C.5 for two frequencies; 1225 and 1575 MHz, which correspond to GPS L2 and L1, respectively. The vertical radiation pattern indicates $G_R > 0$ dBic beamwidth of about 130° in both the upper and lower bands. The HPBW is about 110° and 100° for the two frequencies, respectively. At 5° above the horizon ($\theta = 85^\circ$), the realised gain is about -2.5 and -3 dBic for 1225 and 1575 MHz frequencies, respectively. This corresponds to about 7 and 8 dB drop relative maximum realised gain at the antenna zenith.

The 3 dB AR beamwidth exceeds 180° in the upper band and about 140° in and lower band (Figure C.6). This is unexpected considering the AR limitations due to the mutual coupling as described in section 3.5.2. In this case the adjacent port mutual coupling in the highest in the lower band. At 1225 MHz coupling between ports 1 and 2 is about -11.8 dB (S_{21}), then based on Figure 3.24 the AR upper limit should be about 2.6 dB. However, the simulated $AR < 2.6$ dB beamwidth exceeds 130° at 1225 MHz.

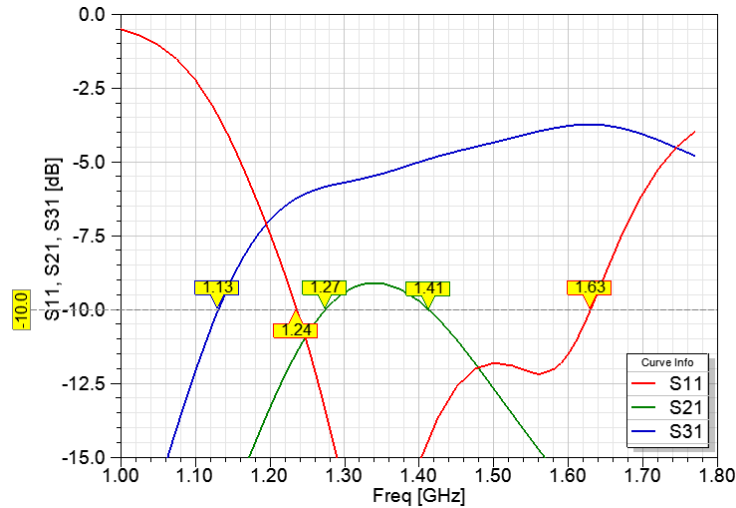


Figure C.3: Reflection coefficients and excitation ports mutual coupling.

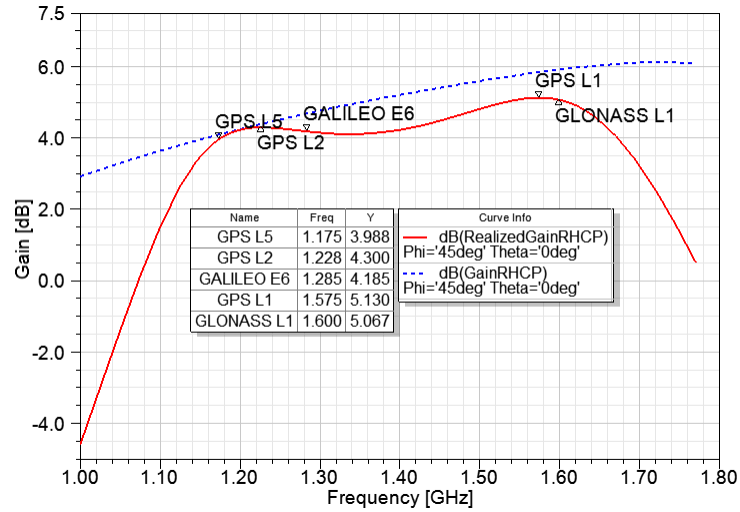


Figure C.4: RHCP total and realized gain.

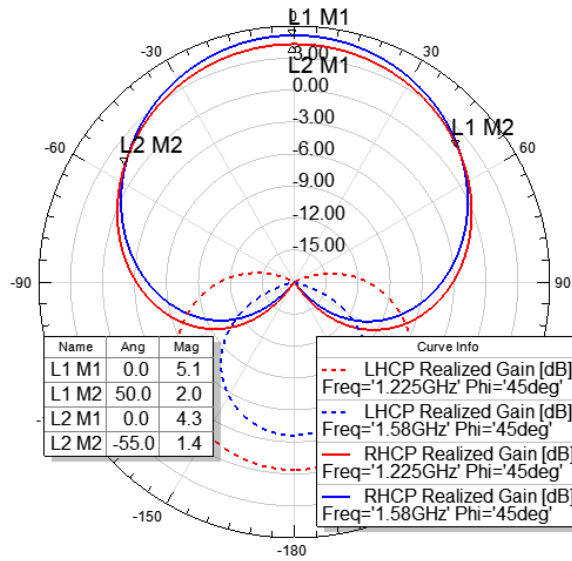


Figure C.5: Vertical plane CP radiation patterns for 1225 (GPS L2) and 1575 MHz (GPS L1) frequencies.

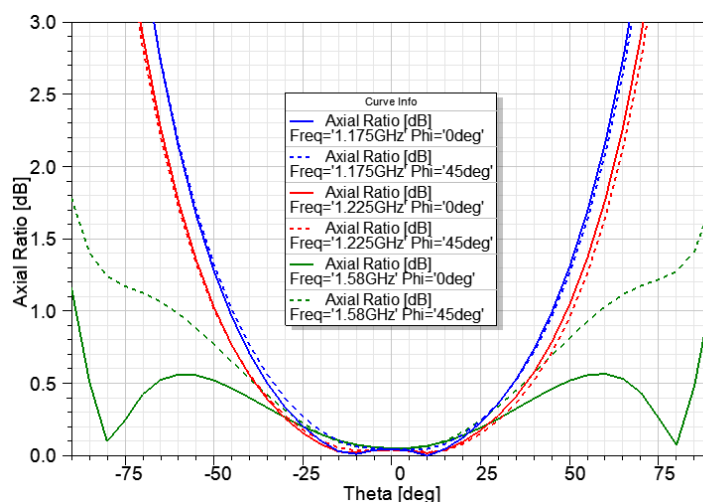


Figure C.6: AR vs. elevation angle for 1225, 1275 and 1575 MHz frequencies.

C.3 Conclusion

Based on the simulation results, it is shown that the DR analytical design process commonly used in the literature does not provide sufficient indication of an antenna performance at least for the $HE_{11\delta}$ radiation mode. The two optimization experiments confirmed that an optimum DRA design needs to consider all the antenna key elements such as excitation technique, number of excitation ports, ground plane size and impedance matching in addition to the DR dimensions, shape and ϵ_r .